# DEVELOPMENT OF RATIONAL NON-INVASIVE BRAIN ELECTROTHERAPY:

## Optimization, Design and Analysis of Transcranial Current Stimulation

By

ABHISHEK DATTA

A dissertation submitted to the Graduate Faculty in Biomedical Engineering in partial fulfillment of the requirements for the degree of Doctor of Philosophy,
The City University of New York
2011

This manuscript has been read and accepted for the
Graduate Faculty in Engineering in satisfaction of the
dissertation requirement for the degree of Doctor of Philosophy

Marom Bikson

Date

Chair of the Examining Committee

Mumtaz Kassir

Date

Executive Officer

Lucas C. Parra

Luis Cardoso

Christopher Chan

Angel V. Peterchev
Supervisory Committee

THE CITY UNIVERSITY OF NEW YORK

**Abstract**

DEVELOPMENT OF NON-INVASIVE BRAIN ELECTROTHERPAY:
Optimization, Design and Analysis of Transcranial Current Stimulation

by

Abhishek Datta

Advisor: Marom Bikson

Transcranial current stimulation involves the application of currents delivered non-invasively. Mild DC currents are used in transcranial DC stimulation (tDCS). Despite safety, cost and ease of use advantages, developments of therapies have been restricted by spatial targeting concerns. This thesis proposes the usage of optimized electrode configurations to improve focality of cortical induced currents. Using Finite element modeling (FEM), optimal stimulation electrode configurations are determined.

The translation of these FEM models to clinical applications requires incorporating highly detailed anatomical features. In this work, we developed a high-resolution MRI-derived model incorporating gyri/sulci specificity. This model is used to compare the conventional stimulation with our optimized configuration.

The proliferation of tDCS therapy has been accompanied by isolated reports regarding skin irritation/burns. The goal of this thesis was to also evaluate safety concerns of the proposed optimized configurations.

Conventional tDCS is being explored to treat patients with traumatic brain injury. The presence of skull defects would alter the intensity/profile of induced current flow and thus modeling these deficits is warranted. The high-resolution model is modified to include skull defects and the resulting changes in current flow are analyzed.

It has been demonstrated that the position of the return electrode and the inter-electrode distance affects modulation under the active electrode. Via FEM, we evaluate the effect of return electrode's position/ size on cortical induced electric fields and compare reported findings.

We also used our high resolution model to compare clinical effects in a fibromyalgia study. Furthermore, we developed an individualized model for a stroke subject who underwent tDCS therapy. We showed that the lesion significantly modulated current flow patterns through the cortex.

Additionally, we validated the accuracy of our FEM model. Transcranial electrical stimulation was applied on a subject and voltage artifacts were compared against an individualized FEM model built for the same subject.

The consideration of tDCS induced current flow is of fundamental importance for the identification of candidates, optimization of electrotherapies and interpretation of clinical results. This thesis highlights the usage of computer models as a tool to develop (optimize/ design) non-invasive brain therapies as well as analyze treatment outcomes.

**Acknowledgements**

I am indebted to my advisor and supervisor, Marom Bikson, for his endless support, encouragement and advice, for providing me with a stimulating environment that allowed me to grow into an independent researcher, for leading me into the world of Neuromodulation, an interdisciplinary and challenging field of research, and for always giving me confidence and guiding me with patience and building the foundation of my future career. His positive attitude with which he approaches any challenge has always been inspirational. It has not always been an easy road, but he has been an anchor of support throughout all these years. I will be forever grateful to him.

I would like to give my special thanks to Lucas C. Parra for his guidance and help, for introducing me to the field of medical imaging and signal processing, and for his invaluable advice and support on numerous topics related to this thesis.

I am grateful to our collaborators Dr. Fortunato Battaglia at Columbia University and Felipe Fregni at Harvard Medical School for providing invaluable clinical information and their constructive suggestions; Dr. Julius Fridriksson at University of South Carolina for his help and guidance in the stroke study. This thesis work could not have been completed without any of them.

My immense gratitude to all the members of my thesis committee: Lucas C. Parra (CCNY), Luis Cardoso (CCNY), Christopher Chan (CCNY) and Angel V. Peterchev (Columbia University). They have been a source of encouragement and advice that have contributed a great deal in the course of my Ph.D. work.

My fellow members of the Neural Engineering Lab have been invaluable to me not only in helping me with the research work, but also in making the lab a fun and exciting place to work at. My thanks to Thomas Radman, Yuzhou Su, Xiang Zhou, Davide Reato, Maged Elwassif, Varun Bansal, Jinal Patel, Asif Rahman, Je Hi An, Julian Diaz, Joao Da Custodia Dias and Jacek Dmochowski. Thanks to them for being a great source of support and friendship.

Heartfelt thanks to my family. I thank my parents Arun Kumar Datta and Sujata Datta and my sister Jayita Datta for their unfaltering understanding, endless support and unconditional love. They have always provided me with every opportunity to succeed at their best. I am indebted to their sacrifice for a lifetime.

# CONTENTS

**Improved spatial focality using a ring electrode versus conventional rectangular pad**



**Chapter 5 Bio-heat Transfer Model of Transcranial DC Stimulation: Comparison of Conventional Pad versus Ring Electrode**



**CHAPTER 6 Transcranial direct current stimulation in patients with skull defects and skull plates**



**Chapter 7 Role of "return" electrode's position and size in design of electrode montage for tDCS**

# List of Tables

# List of Figures

# Chapter 1: Thesis Overview

*In the second chapter*, the background and significance related to the thesis is provided.

*In the third chapter*, we calculate the electric fields induced in the brain during Transcranial Current Stimulation (TCS) using a finite-element concentric spheres human head model. A range of disk electrode configurations were simulated: 1) distant-bipolar, 2) adjacent-bipolar, 3) tripolar; and three ring designs, 4) belt, 5) concentric-ring, and 6) double concentric-ring. We compared the focality of each configuration targeting cortical structures. The distant-bipolar configuration, which is comparable with commonly used TCS protocols, resulted in diffuse (un-focal) modulation with bi-directional radial modulation under each electrode and tangential modulation between electrodes. Increasing the proximity of the two electrodes (adjacent-bipolar electrode configuration) increased focality, at the cost of more surface current. At similar electrode distances, the tripolar-electrodes configuration produced comparable peak focality, but reduced radial bi-directionality. The concentric-ring configuration resulted in the highest spatial focality and uni-directional radial modulation, at the expense of increased total surface current. Changing ring dimensions, or use of two concentric rings, allow titration of this balance. The concentric-ring design may thus provide an optimized configuration for targeted modulation of superficial cortical neurons.

*In the fourth chapter*, we calculate the cortical electric fields induced during tDCS using a high spatial resolution (1 $mm^3$) MRI-derived finite element human head model; cortical gyri/sulci were resolved. We show that electric fields may be clustered at distinct gyri/sulci sites due to details in tissue architecture/conductivity notably cerebrospinal fluid (CSF). The spatial focality of conventional rectangular-pad (7 X 5 $cm^2$) and the ring (4 X 1) electrode configurations were compared. The rectangular-pad configuration resulted in diffuse (un-focal) modulation, with discrete clusters of electric field magnitude maxima. Peak induced electric field magnitude was not observed directly underneath the pads, but at an intermediate lobe. The 4 X 1 ring resulted in enhanced spatial focality, with peak induced electric field magnitude at the sulcus and adjacent gyri directly underneath the active electrode. Anatomically accurate high resolution MRI-based forward-models may guide the 'rational' clinical design and optimization of tDCS.

*In the fifth chapter*, we provide information on the thermal effects of tDCS using a MRI-derived finite element human head model. The proliferation of tDCS therapy has been accompanied by isolated reports regarding concern about their safety namely skin irritation. The potential cause of skin irritation has sometimes been attributed to increased scalp temperature during stimulation. We have developed novel technology for tDCS that improves spatial focality at the cost of increased stimulation electrode current density; high definition tDCS (HD-tDCS). The tissue temperature increases of tDCS using conventional rectangular-pad (7 X 5 $cm^2$) and HD-tDCS using the ring (4 X 1) electrode configurations were compared using a bioheat model. Our results indicate that clinical tDCS do not increase tissue temperature and 4 X 1 ring configurations leads to a negligible increase in scalp temperature.

*In the sixth chapter,* we evaluated the effects of skull defects in conventional tDCS. Preliminary positive results of transcranial direct current stimulation (tDCS) in enhancing the effects of cognitive and motor training indicate this technique might also be beneficial in traumatic brain injury. One perceived hurdle is the presence of skull defects or skull plates in these patients that would hypothetically alter the intensity and location of current flow through the brain. We modeled tDCS using a (MRI)-derived finite element head model with several conceptualized skull injuries. The factors of electrode position (C3-supraorbital or O1-supraorbital), skull defect size, skull defect state (acute and chronic) or skull plate (titanium and acrylic) were analyzed. If and how electric current through the brain was modulated by defects was found to depend on a specific combination of factors. For example, the condition that led to largest increase in peak cortical electric field was when one electrode was placed directly over a moderate sized skull defect. In contrast, small defects midway between electrodes did not significantly change cortical currents. As the conductivity of large skull defects/plates was increased (chronic to acute to titanium), current was shunted away from directly underlying cortex and concentrated in cortex underlying the defect perimeter. The results of this study are the first step to assess safety of transcranial electrical therapy in subjects with skull injuries.

*In the seventh chapter*, we evaluate the effect of "return" electrode's position and size on cortical induced fields. Moliadze et al., 2010 demonstrate in an experimental study that position of the return electrode affects neuromodulation under the active

electrode. The distance between the electrodes was found to negatively correlate with the duration and magnitude of after effects. We report that re-positioning of a cephalic electrode to an extracephalic location shifts the current flow patterns which may explain the "surprising"
findings by Moliadze and colleagues.

*In the eigth chapter,* we aimed to determine analgesic effects of tDCS in fibromyalgia using either a M1 or Supraorbital (SO) active electrode position as a cathode or anode, with a fixed common extracephalic return electrode. For each electrode montage, clinical effects were correlated with predictions of inducted cortical current flow using a magnetic resonance imaging (MRI)-derived finite element method head model. Thirty patients were randomized into five different groups (Cathodal-M1(cat-M1), Cathodal-SO (cat-SO), Anodal-M1 (ano-M1), Anodal-SO (ano-SO), and Sham (M1-primary motor cortex and SO-supraorbital area) to receive a single tDCS application (2mA for 20 minutes). A blinded examiner measured pain changes using a visual numerical scale (VNS), pressure pain threshold (PPT), and a body diagram (BD) evaluating pain area. There was a significant pain reduction in Groups Cat-SO and Ano-SO as indexed by VNS, and PPT (cat-SO was not significant for PPT changes). Computer simulation indicated that the M1-extracephalic montage (contrary to the traditional M1-SO montage) produced dominantly temporo-parietal current flow, consistent with lack of clinical effects with this montage. Conversely, the SO-extracephalic montage produced current flow across anterior prefrontal structures; thus supporting the clinical effects seen with this montage. Our clinical and modeling findings

show that electrode montage is critical for the clinical effects of tDCS as electric current needs to be induced in areas associated with the pain matrix. These results should be taken into consideration for future pain and other tDCS studies in which M1 is the target and extracephalic montage is being considered.

*In the ninth chapter*, we demonstrate how different electrode configurations influence the flow of electrical current through brain tissue in a patient who responded positively to a tDCS treatment targeting aphasia (see Baker et al., 2010). While numerous published reports have demonstrated the beneficial effects of transcranial direct-current stimulation (tDCS) upon task performance, fundamental questions remain regarding the optimal electrode configuration on the scalp. Moreover, it is expected that lesioned brain tissue will influence current flow and should therefore be considered (and perhaps leveraged) in the design of individualized tDCS therapies for stroke. The patient, a 60-year-old male, sustained a left hemisphere ischemic stroke (lesion size = 87.42 cc) 64-months prior to his participation. Here we present results from the first high-resolution (1 $mm^3$) model of tDCS in a brain with considerable stroke-related damage; the model was individualized for the patient who received anodal tDCS to his left frontal cortex with the reference cathode electrode placed on his right shoulder. We modeled the resulting brain current flow and also considered two additional cathode electrode positions: right mastoid and right orbitofrontal cortex. Our results demonstrate the profound effect of lesioned tissue on resulting current flow and the ability to modulate current pattern through the brain, including peri-lesional regions, through electrode montage design.

*In the tenth chapter,* scalp voltage artifact recordings were used to validate an individualized high-resolution FEM model of transcranial electrical stimulation. During transcranial electrical stimulation, current passage across the scalp generates voltage "artifacts" on the scalp surface. Using a recording electrode array, we mapped skin voltage artifacts resulting from transcranial electrical stimulation. Each of the three stimulation electrode configurations tested resulted in a distinct distribution of scalp voltages; these spatial maps were linear with applied current amplitude (0 to 1 mA) over low frequencies (0 to 10 Hz). Our results show that high-resolution individualized FEM models accurately predict scalp voltages resulting from current flow across the scalp. Moreover, our results support the use of high-resolution and individualized models in the understanding and design of transcranial electrotherapies. Finally, the monitoring of scalp voltage artifacts can be used to verify electrode placement to increase transcranial electrical stimulation and reproducibility.

*In the eleventh chapter*, we discuss future work.

# Chapter 2: Background and Significance

## 2.1 Non-invasive Therapy: Promise and Challenge

The use of non-invasive electrical stimulation in the treatment of clinical disorders offers several advantages over pharmacological approaches: 1) in contrast to chemicals, electric fields are rapid; thus electric field paradigms are readily and rapidly adjusted on a patient specific basis, incorporating immediate feedback on behavioral effects; 2) electrical therapy may target specific brain regions and structures; 3) by adjusting stimulation settings, a single device can be (economically) used to treat a wide range of diseases, in a patient customized fashion (Bikson et al., 2009b). However, to take advantage of these features the mechanism underlying electric stimulation therapy must be characterized.

The potential for electrical therapy to treat diseases that are pharmaceutically resistant, or where drugs or resective surgery are associated with unacceptable side effects or unfeasible costs, is motivating the clinical exploration of electro-therapeutic strategies. Electroconvulsive therapy (ECT) and deep brain stimulation (DBS) are two demonstrative examples of electrotherapy success for major depression and movement disorders, respectively. In this thesis, we focus on the development of sub-convulsive non-invasive electrotherapy (tDCS) which has a potentially broad impact of approaches

which do not require surgery or anesthesia. tDCS may also be adaptable for home use. However TCS electrotherapy approaches by virtue of being transcranial are associated with diffuse spatial targeting. This relatively poor spatial focality of non-invasive electrical stimulation amplifies the need to develop functionally focal paradigms; this challenge is intractable without a mechanistic understanding of how electrical stimulation induces change in cortical function.

THE PROMISE: TCS is being explored as therapies for major depression, movement disorders, Parkinson's disease, Alzheimer's disease, epilepsy, obesity, addiction, pain, stroke, schizophrenia, OCD, tinnitus.

THE CHALLENGE: Currently the protocols are determined empirically with a limited set of waveforms used on highly disparate disorders and often requiring time consuming semi-quantitative patient adjustment (George et al., 1999).

RATIONAL ELECTROTHERAPY DESIGN: Characterization of electrical effects on cortical neurons and development of rational approaches for functionally targeted stimulation design will manifestly improve treatment efficacy and safety (Bikson et al., 2006).

**2.2 Functional insights from human and invivo animal studies**

Systematic animal studies in anesthetized rats demonstrated that weak direct currents, delivered by intracerebral or epidural electrodes induce cortical activity and an increase /decrease in excitability (modulation) which persist post stimulation (Bindman et al., 1964). Studies reveal that long-lasting effects are protein-synthesis dependent

(Gartside, 1968) and accompanied by modifications of intracellular cAMP (Islam et al., 1995) and calcium levels (Hattori et al., 1990). Thus these effects share some features with the well characterized phenomena of LTP and LTD. Anodal stimulation was suggested to diminish depressive symptoms (Costain et al., 1964) while cathodal stimulation reduced manic symptoms (Carney, 1969). Unfortunately these results were not replicated in follow up studies possibly because of different patient sub groups, inconsistent stimulation parameters, or other factors that were not controlled for systematically (Bikson et al., 2008).

tDCS has been reevaluated recently and shown to reliably modulate human cerebral cortical function inducing prolonged and reversible shifts of cortical excitability (Nitsche and Paulus, 2000, , 2001). Subsequent tDCS studies have largely adopted the protocols developed by Nitsche and Paulus including the use of relatively large wet sponges with size and current of (1-2 mA) applied for durations up to 20 min. Animal studies implicate that the immediate short-lasting effects of tDCS are probably mediated by polarity specific shifts of the cell's resting membrane potential (Nitsche and Paulus, 2000). On the contrary, the long term effects are attributed to membrane potential changes as well as plastic changes in synaptic connectivity especially mediated by NMDA receptors (Liebetanz et al., 2002; Nitsche et al., 2003a).

**2.3 Cortical Modulation function: Electric field**

Transcranial stimulation generates extracellular voltage gradients (electric fields) inside the head and these fields will lead to polarization of sections of neuronal membrane. This induced membrane polarization will affect a range of functional/cellular properties. Relatively strong supra-threshold electric fields will trigger action potentials. Sub-threshold fields can modulate the firing properties of neurons (e.g. action potential threshold / timing (Jefferys, 1981; Radman et al., 2007), synaptic efficacy(Bikson et al., 2004) , and neuronal information processing (Deans et al., 2007).

It is well established that the 'point' extracellular voltage generated by applied stimulation does not provide a useful indication of neuronal modulation; for this reason proximity to anode or cathode does not either provide meaningful information on cell *modulation*. Rather, the *spatial distribution* of extracellular voltages (electric field) is applied to a modulation function (which may also include information on neuronal geometry, membrane biophysics, synaptic properties) that determines neuronal modulation at each location. The classic "Activating Function" considers the electric field *derivative* along each membrane segment.

In determining 'cortical modulation functions' in this report, we considered the electric field magnitude induced in the brain. The consideration of electric field (as opposed to the electric field derivative / classical activating function (Rattay, 1986) may be a suitable approximation if for transcranial current stimulation, the induced electric field is locally uniform on the scale of any given neuron and neuronal modulation is directly related to uniform electric field amplitude. The latter is supported by

experimental and theoretical studies showing; 1) polarization of short or bent cortical axons is linear with (sub-threshold) electric field amplitude (Nagarajan et al., 1993; Tranchina and Nicholson, 1986); 2) synaptic efficacy is quasi-linear with electric field amplitude (Bikson et al., 2004; Jefferys, 1981); 3) somatic and dendritic process polarization is linear with (sub-threshold) uniform electric field amplitude (Chan et al., 1988; Hause, 1975); and 4) metrics of neuronal excitability vary with electric field amplitude (Amassian et al., 1994; Bikson et al., 2004; Ghai et al., 2000).

**2.4 tDCS Efficacy and Safety metrics**

An assumption is often made in tDCS studies that the ratio of the injected current to the electrode area (I/A = 1 mA / 35 $cm^2$) determines the magnitude of stimulation effect or efficacy (Miranda et al., 2009; Nitsche et al., 2008). This assumption is implicitly made when I/A ratio is typically used to specify and compare stimulation intensities. However it should be noted that when comparing tDCS electrode montages, increased surface electrode current densities do not necessarily equate with brain modulation (cortical electric fields). Standardization to calculated electrode-surface current density (total current/electrode area) assumes that current density at the scalp scales consistently with current density at the brain; this assumption does not necessarily hold across electrode configurations ( in part because of differences in fractional scalp/ skull loss) or for relatively small electrodes. For example, a micro-electrode (0.01 $cm^2$ area) with 'standardized' current density (1 mA / 35 $cm^2$ × 0.01 $cm^2$ = 0.0003 mA current) will not be effective. In addition, current density is not uniform on the electrode

surface (Miranda et al., 2006; Wagner et al., 2007). Nonetheless, approximated uniform electrode-surface current density (total current/electrode area) remains a useful functional/safety metric because it presumably places an upper limit on current density, and hence electric field in the brain; assuming current density diffusion through scalp/ skull interface (Bikson et al., 2009a; Wagner et al., 2007) offsets current density concentration at the electrode edges.

**2.5 Electrical stimulation of tissues and sensitivity of brain to temperature rises.**

The electrical stimulation of tissues can lead to temperature increases as a result of both Joule heat and metabolic responses to stimulation (Elwassif et al., 2006). The electrical stimulation of rat brains with microelectrodes has been shown to increase brain temperature. Brain function is especially very sensitive to changes in temperature. An increase in temperature by ~1 °C can have profound effects on a single neuron and neuronal network function (Fujii et al., 2002; Hoffmann and Dionne, 1983). All biophysical properties are temperature dependent including membrane properties such as passive resistance/capacitance and voltage gated channel kinetics. Changes in membrane properties will thereby affect firing threshold, peak firing rate and depolarization block threshold. Excitatory and/or inhibitory synaptic transmission is also highly sensitive to temperature changes.

**2.6 Use of tDCS in patients with skull defects: Safety concerns**

Because tDCS has been increasingly studied for the treatment of neuropsychiatric diseases, an important question explored as part of this proposal is what would be the effect of skull defects/skull plates on induced current in brain. This is an important issue since a relatively large proportion of patients might have skull defects and skull plates such as patients with stroke, who underwent decompression craniectomy, or patients with refractory epilepsy who undergo epilepsy surgery and finally patients with traumatic brain injury that commonly have skull fractures or need to undergo craniectomy. To date, there are no studies assessing the effects of tDCS in these patients. The only investigation using another technique of noninvasive brain stimulation involved the use of transcranial magnetic stimulation in patients with refractory epilepsy and titanium plates. In these two studies, authors assessed temperature and side effects and showed minimal or no effects on these parameters after repetitive TMS (Rotenberg et al., 2007; Rotenberg and Pascual-Leone, 2009). It would be important to repeat such experimental evaluations for the case of tDCS. The biophysics surrounding how defects and plates modulate current flow for the cases of tDCS and TMS are distinct, and one cannot directly extrapolate stated efficacy or safety guidelines. During tDCS, current applied at the scalp must pass through the resistive skull before reaching the brain, and the specific relationship between electrode position, skull geometry, and the underlying tissue properties are thought to determine the location and magnitude of current flow (Datta et al., 2009a). It remains unknown how skull defects and use of skull plates associated with TBI would affect current flow through the brain and how to *modify* tDCS dose in such cases. For example, a hole through the skull that is filled with relatively highly conductive fluid or tissue, might present an attractive "shunt" pathway for current entering the brain. The

underlying cortex would then be exposed to a higher intensity of focused current flow. This in turn might be either beneficial in targeting the underling brain region or hazardous if the increased current levels resulted in undesired neurophysiologic or pathological changes.

## 2.7 Importance of Numerical Computation: The Finite Element Method

Finite element method (FEM) is a technique that has been increasingly used in studying brain-electromagnetic field interactions because of its ability to solve the dynamics of physical phenomena in complex geometries. Non-invasive electrotherapy is being explored to treat a host of neurological and /or cognitive deficits but the exact spatial profile of brain electric fields and current flow is still not well understood or known.

Experimental measurement of induced electric fields in humans is difficult and researchers have therefore focused their efforts on building finite element models to simulate various electrotherapy modalities. Efforts ranging from spherical head models to more realistic head models which possess improved approximations of the shapes of different parts of the head have been developed (Im et al., 2008; Oostendorp et al., 2008; Wagner et al., 2007; Wongsarnpigoon and Grill, 2008). However limitations in the resolution of the modeled head restrict the accuracy of such simulations. These models do not contain clear anatomical borders and features such as cortical gyri/sulci. Reduced resolution of *boundaries* between tissue parts may result in inaccuracies especially at

these boundary surfaces where increased concentration of the induced current density probably occurs. Studies have shown that local perturbations in tissue geometry and at tissue boundaries in the head can have significant effects on the distribution of induced current densities.

**2.8 MRI derived model:**

Volume conductor models were created with the same resolution ($1mm^3$) as the MRI data used to derive them. The raw scans were first contrast enhanced and noise filtered.

The typical workflow involved the following steps:

1) Segmentation: The head was segmented (using a combination of manual and automated segmentation) into compartments (or 'masks') representing the brain, CSF, skull, muscle, fatty tissue, eyes, blood vessels and the scalp respectively (Simpleware Ltd). The segmentation of the *background data* (grayscale data e.g. CT, MRI) results in *masks* that define how an object fills the space. Thus each region of interest (e.g. eyes, skull, etc.) was represented by a mask. Masks are convenient to operate upon since they can be modified and filtered before converting them into a finite element mesh.

The skull was initially hand segmented using the *paint* tool (see below for explanation). The brain mask was created by dynamically *thresholding* the image data. Then a

recursive *Gaussian filter* was applied at 1 mm (Gaussian kernel width) in all directions to smooth the surface of the mask. Filtering usually leads to the creation of 'islands' or holes (unconnected pixels in the mask). A *floodfill* algorithm was then used to remove any islands from the mask. Furthermore, using a threshold algorithm may lead to regions having similar gray scale values as that of the brain (especially dura) being assigned as part of the brain mask. These regions are manually disconnected from the brain mask. The new skull mask was created by simply smoothing (using recursive Gaussian filter) the original segmentation (manually segmented) at 2 mm in all directions. The CSF is created by using "*Booleans*" to fill the gap between the brain mask and the skull mask. However it should be noted that a simple fill of the gap was only possible from the top of the head until the level of the head where fatty tissue and eye balls begin to appear. From this level to the bottom of the head, appropriate Booleans are implemented to correctly segment the different compartments of the head. The scalp compartment is created by thresholding the background and then inverting the mask. The mask is then subtracted (Boolean) from all the other masks in the model to obtain the scalp mask. The scalp mask is then Gaussian filtered to obtain a smother surface. The muscle, eye balls, blood vessels compartments were hand segmented. At all steps during the segmentation process, results are validated against an anatomical MRI atlas.

The image processing steps of some of the segmentation tools mentioned above are as follows:

*Gaussian kernel width*: The width of the Gaussian kernel defines around each visited pixel how many neighboring pixels should contribute to the smoothing operation. The larger the kernel, the stronger is the smoothing. Values from 1 to 3 times the pixel spacing of the data in each direction usually result in good smoothing.

*Paint*: This tool makes it possible to edit masks by hand to tidy up segmentation or disconnect unwanted regions. The tool allows you to add and/or delete individual pixels.

*Threshold*: The threshold algorithm selects a window of grayscale values and is useful where segmentation can be achieved based on grayscale intensities.

*Floodfill*: This algorithm is a region growing algorithm where the threshold value is considered to be the measure of similarity or connectivity.

*Boolean operations*: These tools include operations to invert, combine, subtract, and intersect different masks to generate new masks.

For the MRI derived model, the electrodes were imported as CAD models and placed appropriately within the image data. Each of these CAD models is also converted to masks.

2) After segmentation, the masks are converted to surface meshes. The surface meshes are then converted to volumetric tetrahedron meshes by ‘smooth’ meshing as opposed to

voxel meshing. The minimum element quality was chosen to be 0.4 and 'off-surface' meshing was allowed. The tetrahedral quality metric is the normalized in-out radius given by the following (Simpleware Reference Guide):

$$Q = 3 \cdot \frac{R_{in}}{R_{out}} \quad (1)$$

where $R_{in}$ = inscribed sphere radius

and $R_{out}$ = circumscribing sphere radius

A minimum quality of 0.1 or over generally indicates a mesh of excellent quality (Simpleware Reference Guide). Off-surface meshing allows the meshing optimizer to migrate surface nodes if optimization on-surface fails to achieve the specified minimum quality target for the mesh. This may compromise surface smoothness and topology to some extent but generally always guarantees a good quality mesh.

For the volume conductor models (see below), the resultant mesh had > 10 million tetrahedral elements with > 15 million degrees of freedom. For the bioheat transfer model generated previously at 2 mm resolution (see C.3), the meshes had > 5 million tetrahedral elements with > 20 million degrees of freedom. The meshes are eventually exported to a COMSOL Multiphysics, a commercial FEM package.

**2.9 Model Physics**

1) Electric field in a volume conductor

A quasi-stationary condition was assumed for the volume conduction in our model. The electric field in a volume conductor is represented as:

$$\nabla.(\sigma \nabla V)=0 \qquad (2)$$

(V: scalar electric potential; $\nabla$ : gradient vector; $\sigma$ : conductivity).

The resulting Laplace equation assuming uniform conductivity was eventually solved to determine the induced cortical electric field distributions.

2) Bioheat Transfer Model:

An approximate temperature distribution throughout a perfused tissue can be found by solving the bio-heat transfer equation suggested by Pennes (Nelson and Nunneley, 1998):

$$\rho C \frac{\partial T}{\partial t} = \nabla(k \nabla T) - \rho_b \omega_b C_b (T - T_b) + Q_{met} \qquad (3)$$

where $\rho$: density; $C$: specific heat; $\kappa$: thermal conductivity; $\omega_b$: blood perfusion rate; $T$: temperature; $T_b$: arterial blood temperature; $Q_{met}$: metabolic heat.

During electrical stimulation, additional joule heating arises when energy is dissipated by an electric current flowing through a conductor. The Laplace equation

$\nabla.(\sigma\nabla V) = 0$ (V: potential; σ: conductivity) was solved to determine the electrical potential. The Pennes equation (1) above is modified to incorporate joule heating during electrical stimulation (Elwassif et al., 2006). In addition, we considered steady state temperature increases consistent with prolonged tDCS protocols (>10 minutes) (Nitsche and Paulus, 2001) ; resulting in the following bio-heat equation:

$$\nabla(-k\nabla T) = -\rho_b\omega_b C_b(T - T_b) + Q_{met} + \sigma|\nabla V|^2 \quad (4)$$

The electrical and thermal properties of the tissues were assigned the representative average values taken from literature. COMSOL Multiphysics 3.5 (Comsol Inc., MA), a commercially available finite element (FE) package is used to implement the models. For models with large degrees of freedom (>100,000), *direct* solvers as opposed to *iterative* solvers typically need much more memory. However iterative solvers are less stable (do not always converge) than direct solvers. To optimize memory usage, we used iterative solvers in these studies. For the volume conductor model, the stationary linear system iterative solver of conjugate gradients was used with a relative tolerance of 1 X $10^{-6}$.

For the bioheat models, the linear system iterative solver of BICGStab was used. The relative tolerance was also set to 1 X $10^{-6}$. BICGStab is typically used for nonsymmetric problems and uses a fixed amount of memory independent of the number of iterations. Therefore it uses less memory than GMRES, which is another alternative

for nonsymmetric problems in COMSOL Multiphysics. The algebraic multigrid preconditioner was used in both the models.

# Chapter 3: Transcranial current stimulation focality using disk and ring electrode configurations

### 3.1 Introduction

Transcranial Current Stimulation (TCS) involves the application of currents through electrodes on the scalp to modulate brain activity. Transcranial Electrical Stimulation (TES) conventionally refers to short duration (50 -500 μs) supra-threshold pulses (100-1200 V) (Calancie et al., 1998; Holdefer et al., 2006; Zentner, 1989). Cranial Electrotherapy Stimulation (CES) utilizes a range of waveforms with peak current levels ranging from 50 μA to 5 mA (Schroeder and Barr, 2001). Supra-threshold current pulse trains (~ 0.9 A) are generally used during Electroconvulsive Therapy (ECT) (Nadeem et al., 2003). DC waveforms normally ranging from 260 μA to 2 mA are used for Transcranial Direct Current Stimulation (tDCS) (Ardolino et al., 2005; Iyer et al., 2005; Marshall et al., 2005; Nitsche et al., 2003c; Nitsche and Paulus, 2000). The objective of this study was to examine optimized electrode configurations and to develop 'modulation maps' that may guide anatomically and functionally targeted TCS applications.

Generally, TCS electrode configurations utilize one anode and one cathode, positioned around the head. tDCS applied to M1 can facilitate implicit learning (Nitsche et al., 2003d) and tDCS over the occiptal cortex can facilitate visuo-motor learning (Antal et al., 2004b). tDCS has also been shown to alter excitability or related behavioral performance in somatosensory (Uy and Ridding, 2003), frontopolar (Kincses et al., 2004) and prefrontal cortices (Fregni et al., 2005a). Clinical TCS is being actively explored as a

non-invasive therapeutic option for the treatment of neurological and psychiatric disorders including depression, stroke, epilepsy, learning disorders, and for relieving pain (Boggio et al., 2007; Boggio et al., 2006; Fregni et al., 2006b; Liebetanz et al., 2006; Lisanby, 2007; Webster et al., 2006).

Experimental and theoretical studies examining the mechanisms of TCS have implicated 'direct' modulation (polarization) of primary cortical neurons (Ardolino et al., 2005; Nitsche et al., 2005; Suihko, 1998) and/or modulation of (NMDA) synaptic efficacy (Liebetanz et al., 2002; Nitsche et al., 2003a). Anode and cathode specific modulation of brain activity has been characterized using broad indicators of "excitability" (Ardolino et al., 2005; Bindman et al., 1964; Lang et al., 2004; Nitsche et al., 2007; Nitsche and Paulus, 2000; Nitsche et al., 2005; Purpura and McMurtry, 1965) . Oscillating transcranial currents can entrain cortical oscillations (Marshall et al., 2006; Schroeder and Barr, 2001). *In vivo* (Gartside, 1968) and *in vitro* (Bikson et al., 2004; Deans et al., 2007; Radman et al., 2007) animal studies have identified complex short- and long-term actions on neuronal excitability. Despite clinical success with existing TCS technology, efficacy and targeting concerns include: 1) divergent cathodal and anodal effects (Nitsche et al., 2007; Saypol et al., 1991); 2) poor spatial focality (Nathan et al., 1993; Rossini et al., 1985); 3) poorly characterized cellular targets (e.g. neuronal type) and biophysics of both short and long-term modulation (Bikson et al., 2004; Nitsche et al., 2003b; Priori, 2003a, 2003b; Radman et al., 2007). Clinical protocols are thus adjusted empirically and restricted within a conservative parameter range.

Strategies using either 'ring' (also termed 'belt' or 'unifocal') electrode configurations (Besio et al., 2007; Rossini et al., 1985; Saypol et al., 1991; van Oosterom and Strackee, 1983), scaling bipolar electrode size (Nitsche et al., 2007), or increasing number of electrodes (Rossini et al., 1985; Suihko, 2002) have previously been investigated to address concerns about TCS spatial focality (and related stimulation current threshold). Here we further consider optimizing the shape (geometry) and number of electrodes. In addition, we develop 'modulation maps' addressing cellular target orientation. We compare the focality and efficacy of TCS stimulation of cortex with remotely spaced bipolar electrodes ("distant-bipolar") (Nitsche and Paulus, 2001; Nitsche et al., 2003d), proximal bipolar electrodes ("adjacent-bipolar")(Nathan et al., 1993; Rossini et al., 1985; Saypol et al., 1991), "tripolar" electrodes, and three ring electrode configurations: "belt" (Rossini et al., 1985; Saypol et al., 1991), "concentric-ring", and "double concentric-ring" using a reduced concentric sphere head model. The analysis of the electric field distributions induced inside the brain for different electrode configurations/geometries will allow for the "rational" (Bikson et al., 2006) design of TCS research and clinical protocols.

### 3.2 Model Methods and Analysis

The head was simulated as a 3-D inhomogeneous medium comprising concentric spheres; each sphere was homogeneous and isotropic. The concentric head model (three and four layer) is accepted for its quantitative agreement with a variety of general observations of the electroencephalogram and magnetoencephalogram (Ferdjallah et al.,

1996; Rush and Driscoll, 1968; Stecker, 2005; Suihko, 1998) and has been experimentally validated for transcranial stimulation (Rush and Driscoll, 1968). Four concentric spheres of 61.53 mm, 64.03 mm, 71.76 mm, and 76.49 mm radii represent the brain tissue, the cerebrospinal fluid (CSF), the skull, and the scalp, respectively; the dimensions of the head are based on a 26 year old male (Ferdjallah et al., 1996). The electrical properties of the four layers of the model were assigned representative average values taken from standard sources (Akhtari et al., 2002; De Mercato and Garcia Sanchez, 1992; Geddes and Baker, 1967; Ranck, 1963): (in units of S/m) scalp 0.465; skull 0.010; CSF 1.650; brain 0.200.

Although a symmetric model is used, 10/20 EEG notation is applied to indicate relative electrode location for different stimulation configurations. For distant-bipolar stimulation and double concentric-ring, the electrodes were placed at equivalent distances from the head apex (analogous to Cz), while for all the other stimulation scenarios; the electrodes were oriented in order to obtain a peak electric field under the head apex.

We simulated a range of electrode configurations (indexed below); for several configurations we tested a sub-set of electrode geometries (e.g. size) as indicated. For existing clinical electrode configurations, studies with comparable placements are referenced.

"Distant-Bipolar": Simulation with two disc electrodes, centre's placed 52.4 mm apart to approximate standard tDCS stimulation of the primary motor cortex with the active electrode over C3 and the reference electrode at the forehead above the

contralateral orbita (analogous electrode placements can be used according to the desired target). “Distant-bipolar” is also referenced in the literature as unipolar stimulation (Nathan et al., 1993).

“Adjacent-Bipolar”: Simulation with two disk electrodes separated by 25 mm. This is similar to the separation distance of electrodes previously referenced as “bifocal stimulation” (Cohen and Hallett, 1988; Saypol et al., 1991).

“Tripolar”: Simulation with three disk electrodes, each one separated by 25 mm from the other. This approximately corresponds to the first anode between CPz and Pz, second anode over C1, and the cathode over C2. The current at each anode was equal; the summed current at the single cathode was thus double this value.

“Belt”: Simulation with a cathode belt (2 mm wide, outer radius: 67 mm, and inner radius: 65 mm) circling the forehead and an anode disk electrode placed on Cz. Belt stimulation is also referred to as “unifocal stimulation” (Rossini et al., 1985; Saypol et al., 1991).

“Concentric-Ring”: Simulation with a cathode ring electrode (outer radius ranging from: 11 - 23 mm, inner radius: 9 - 21 mm) enclosing an anode disk electrode (of either 3 / 4 mm radius) over Cz.

"Double Concentric-Ring": two concentric ring electrodes: outer anode ring electrode (outer radius: 17 / 14 mm, inner radius: 15 / 13 mm); inner cathode ring electrode (outer radius: 11 / 9 mm, inner radius: 9 / 8 mm). Both the ring electrodes enclosed a third anode disk electrode (4 mm radius) over Cz. We considered both 'symmetric current', where the total current at each anode was equal, and 'asymmetric current', where the total current was different at each anode; in both cases, the current at the cathode was the summation of the two anodic currents.

Unless otherwise noted, all the disk electrodes had a default 4 mm radius (Marshall et al., 2004; Marshall et al., 2005). The thickness of the disk electrodes was 0.5 mm, while ring electrode thicknesses varied from 0.25 mm to 2 mm; the thickness of the electrodes increased with increasing radius in order to maintain continuous contact with the curved scalp. Note that electrodes were only energized on the flat distal surface (see below); (Szmurlo et al., 2006). We do not explicitly consider the use of conductive gels or sponges.

The electrodes were modeled as conductors with the conductivity of copper ($5.8 \times 10^7$ S/m). The Laplace equation $\nabla.(\sigma\nabla V) = 0$ (V: potential; $\sigma$: conductivity) was solved and the boundary conditions used were: 1) inward current flow = $J_n$ (normal current density) applied to the distal surface of the "anode" electrode(s), 2) ground applied to the distal surface of the effective "cathode" electrode, 3) all other external surfaces treated as insulated. Note that the total current at the effective cathode electrode thus equals the total anodic current; we confirmed similar current density profiles at the electrode/scalp

interface of bipolar anode and cathode electrodes. Any current density inhomogeneities at the electrode/scalp interface are not reflected at the cortical surface due to the resistance of the skull (Miranda et al., 2006) and did not affect peak cortical electric field (see tolerance below).

For 'distance-bipolar' configuration stimulation, the total injected current was 1 mA (comparable to tDCS protocols); this resulted in a 0.328 V/m peak electric field, 1 mm under the cortical surface. For all other configurations the "equivalent" total injected current ($I_{eq}$) was adjusted to obtain a 0.328 V/m peak electric field, 1 mm under the cortical surface.

The FEM solver was implemented using FEMLAB 3.3 (COMSOL Inc., Burlington, MA). The model was adaptively meshed into more than both 1,200,000 tetrahedral elements and 150,000 boundary triangular elements for each of the simulations. The linear system solver of conjugate gradients was used with a relative tolerance of 1 E-6. Increasing the number of elements by a factor of 4 or reducing the relative tolerance of the solver to 1 E-8 changed the peak electric field values by less than 1 %.

"Surface-magnitude" plots were generated by plotting the magnitude electric field 1 mm below the top half of the innermost sphere in the model (i.e. brain surface). Cortical electric fields produced during surface stimulation have components both parallel and perpendicular to the head surface (Saypol et al., 1991). "Surface-radial" plots

were thus generated by plotting the component of the electric field on the brain surface in the direction normal to the surface (toward the sphere centre). "Surface-radial ±" plots further considered directionality (away or toward the cortical surface). "Surface-tangential" plots were generated by plotting the component of the electric field parallel to the brain surface. "Cross-section magnitude" plots were generated by plotting the magnitude electric field on a coronal slice through the sphere centre's including the head apex. "Cross-section radial" and Cross-section tangential" plots represent electric fields oriented normal and parallel to the cortical surface, respectively. In the case of "bipolar" stimulation, the coronal slice included both electrode centres. In case of "tripolar" simulation, the coronal slice included the centre of the cathode and one of the anodes. In the case of ring configurations, fields were radially symmetric around the head apex. In addition for each of the electrode configurations, electric field magnitude line-plots along the cortical surface and brain depth were generated.

### 3.3 Results

For each configuration/geometry, we calculated the induced electric fields in the head. To allow direct comparison between configurations/geometries we applied "equivalent currents" ($I_{eq}$) such that *peak* cortical electric field in all cases was 0.328 V/m (Table 1). The 'surface-magnitude' and 'cross-section magnitude' plots of each configuration thus allow direct comparison of relative spatial focality (Figure 1). In addition, spatial space-constants, quantifying surface and depth focality, are compared (Table 1). For cortical surface/cross-section plots, radially oriented fields (normal to the

brain surface) and tangential oriented fields (along the brain surface) are considered independently (Figure 1); note that in these plots the maximal radial and tangential fields are not the same, reflecting that different configuration results in different ratios of radial and tangential currents. Finally for radial cortical fields, the direction of current flow is considered explicitly (surface-radial ± plots); these plots are normalized to the maximal positive and/or negative radial field to illustrate the relative bi-directionality of modulation. "Unidirectional" modulation refers to electrode configurations with significant radial electric fields crossing the cortical surface in only one direction (i.e. with the return path sufficiently diffuse).

For all configurations the high resistivity of the skull relative to the scalp, results in current 'shunting' through the scalp, consistent with previous transcranial stimulation studies (Rossini et al., 1985; Saypol et al., 1991). The degree of shunting and the ratio of distal electrode-surface current density (DESCD) with the peak cortical surface current density (CSCD) vary significantly across electrode configurations (Table 1) (Wagner et al., 2007).

*Disk Configurations*

"Distant-bipolar" stimulation results in relatively diffuse cortical and depth modulation (Table 1, Figure 2). Current crosses into the cortex under each electrode and then transverses the brain resulting in *radial* fields under each electrode, and *tangential*

fields in between (Figure 1). The peak inward and outward radial currents are equivalent, resulting in bi-directional modulation.

Increasing the proximity of the two bipolar electrodes, "adjacent-bipolar stimulation", results in more current being 'shunted' across the scalp surface. The equivalent current, to generate comparable peak cortical electric fields, is thus increased from 1 to 1.43 mA (Table 1). In addition, though radial bi-directional currents are still prominent under each electrode, more relative tangential cortical fields are generated (Figure 1). Thus for adjacent-bipolar stimulation the peak electric field is between both electrodes, while the peak radial field is under each electrode. Consistent with previous studies (Nathan et al., 1993; Saypol et al., 1991), we found that "adjacent-bipolar" stimulation is more focal, along both the cortical surface and depth, than

**Figure 1. Finite element model of brain electric fields induced by varied surface stimulation electrode configurations**. For the five electrode configurations illustrated (left to right) the total electrode current ($I_{eq}$) was adjusted to produce a peak 0.328 mV/mm electric field, 1 mm below the cortical surface. The top two rows diagram the *electrode geometries* and *solver mesh*. The remaining rows plot the induced electric fields in varied planes and directions (see Datta et al. 2008). The *surface-magnitude* plot maps the electric field magnitude along the top head hemisphere, 1 mm below the cortical surface. The *surface-radial* and *surface-tangential* plots decompose this plot into the radial (normal to the surface) and tangential (along the brain surface) directions; note that in the cases of bipolar stimulation and tripolar stimulation significant differences exist between the surface-magnitude and surface-directional (radial and tangential) plots, while in the belt and ring configurations the surface-magnitude and surface-radial are similar, consistent with dominantly radial surface cortical current flow. The *surface-radial* ± plots are normalized to respective peak surface-radial field (indicated in inset) and highlight which configurations produce radial bi-directional modulation. The *cross-section magnitude* plot maps the electric field magnitude on a central cortical cross-section. The *cross-section-radial* and *cross-section-tangential* plots decompose this plot into the radial (normal to the surface) and tangential (along the brain surface) directions. All surface/cross-section electric field plots are on the indicated spatial scale, the mesh diagrams are scaled for clarity. (Note: 'o.r.', 'i.r.', 'Mag', and 'Tang' abbreviate 'ring outer radius', 'ring inner radius', 'magnitude', and 'tangential', respectively).

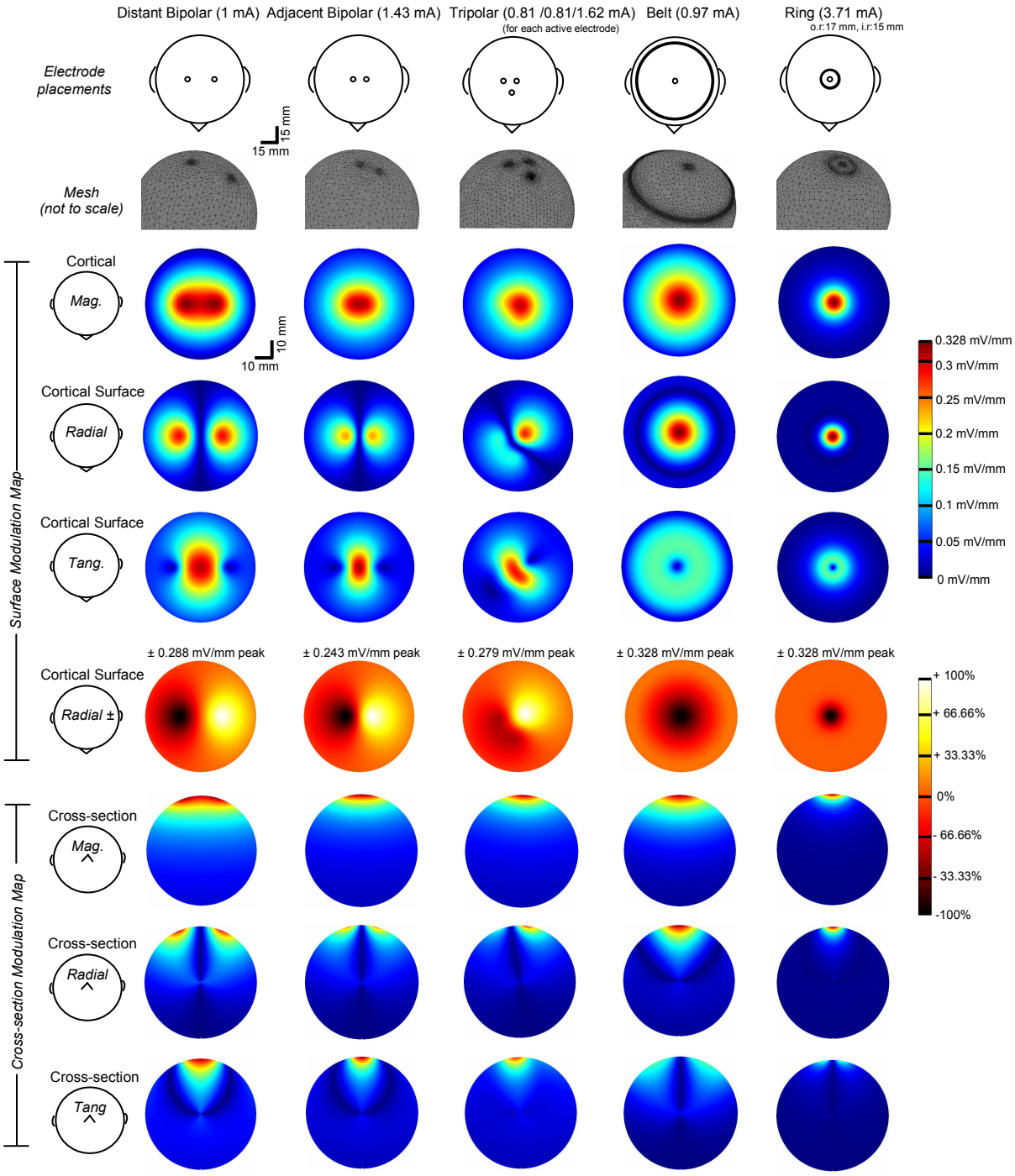
Distant Bipolar (1 mA)
Adjacent Bipolar (1.43 mA)
Tripolar (0.81 /0.81/1.62 mA)
(for each active electrode)
Belt (0.97 mA)
Ring (3.71 mA)
o.r:17 mm, i.r:15 mm
Electrode placements
15 mm
15 mm
Mesh (not to scale)
Surface Modulation Map
Cortical
Mag.
10 mm
10 mm
Cortical Surface
Radial
Cortical Surface
Tang.
± 0.288 mV/mm peak
± 0.243 mV/mm peak
± 0.279 mV/mm peak
± 0.328 mV/mm peak
± 0.328 mV/mm peak
Cortical Surface
Radial ±
0.328 mV/mm
0.3 mV/mm
0.25 mV/mm
0.2 mV/mm
0.15 mV/mm
0.1 mV/mm
0.05 mV/mm
0 mV/mm
+ 100%
+ 66.66%
+ 33.33%
0%
- 66.66%
- 33.33%
-100%
Cross-section Modulation Map
Cross-section
Mag.
Cross-section
Radial
Cross-section
Tang

"distant-bipolar" stimulation (Figure 2) at the cost of shunted scalp current.

The "tripolar"configuration effectively divides the anodic current to two electrodes (0.81 mA equivalent current at two anodes, and -1.62 mA at the effective cathode). Tripolar stimulation was found to have similar total magnitude field focality as "adjacent-bipolar" stimulation (Table 1, Figure 2), but directional surface plots indicate that while radial currents dominate under the single cathode, tangential currents are prominent under the two anodes (Figure 1).

*Ring Configurations*

Although the "belt" configuration is not evidently more focal than "distant-bipolar" stimulation (Figure 1, 2), it requires slightly less equivalent current (0.97 mA). A relatively high density radial current crosses the brain surface under the centre disc electrode; the return current path to the belt electrode is relatively diffuse. The net result is unidirectional and radial modulation under the centre disc.

The "concentric-ring" configuration had the highest relative focality of the configurations evaluated (Table 1, Figure 2) at the cost of moderately increased equivalent current (3.71 mA). Similar to belt stimulation, fields were dominantly radial under the disk electrode and unidirectional (Figure 1). In the case of the concentric-ring, current crosses into the brain at high current density under the disk and rapidly diffuses in the brain (diffuse current densities producing negligible electric fields), the current

remains diffuse as it exits the brain and returns to the ring electrode via the scalp. The increased equivalent current presumably reflects the portion of current that 'shunts' between the disk and ring electrode along the scalp *without* crossing into the brain (without effecting brain function, see Discussion). Increasing the ring diameter decreases the shunt fraction and thus the required equivalent current, at the cost of focality (Table 1).

For moderate ring diameters, electric fields distribution using the "double concentric-ring" configuration roughly approximated those generated under the concentric-ring (Figure 1), with cortical radial stimulation area increasing and $I_{eq}$ decreasing with increasing outer ring diameter. Appropriate selection of ring diameters and/or use of asymmetric currents (where the total anodic current at the inner disk and outer ring are not equal) resulted in generation of ring modulation regions (Figure 3). Similarly, the relative balance of radial versus tangential electric field can be controlled. Rather then suggest specific clinical applications, these examples illustrate how electrode number, size, and current balance can be independently controlled in designing stimulation configurations.

**Table 1.** Summary of evaluated electrode configuration/geometries equivalent currents and focality.

| Electrode configuration/geometry (all dimensions in mm) | | | $I_{equivalent}$ (mA) | Surface space constant (mm) | Depth space constant (mm) | DESCD (mA cm$^{-2}$) | mDESCD/ CSCD |
|---|---|---|---|---|---|---|---|
| Bipolar | | | | | | | |
| *disc electrode separation* | | | | | | | |
| 52.4 (distant bipolar) | | | 1.00 | 22.90 | 13.60 | 1.99 | 302 |
| 25.0 (adjacent bipolar) | | | 1.43 | 22.48 | 7.42 | 2.84 | 430 |
| Tripolar | | | | | | | |
| *disc electrode separation* | | | | | | | |
| 25 | | | 0.81/0.81/1.62 | 18.14 | 7.38 | 1.61/1.61/3.22 | 488 |
| Concentric ring | | | | | | | |
| *ring (o.r., i.r.)* | | *Disc (radius)* | | | | | |
| 11, 9 | | 4 | 8.12 | 8.89 | 3.25 | 6.46/16.15 | 2447 |
| 17, 15 | | 4 | 3.71 | 10.61 | 3.80 | 1.84/7.38 | 1118 |
| 23, 21 | | 4 | 2.45 | 12.58 | 4.58 | 0.89/4.87 | 738 |
| 67, 65 (Belt) | | 4 | 0.97 | 22.51 | 10.93 | 0.12/1.93 | 292 |
| 11, 9 | | 3 | 7.59 | 8.81 | 3.20 | 6.04/26.84 | 4067 |
| 17, 15 | | 3 | 3.49 | 10.52 | 3.76 | 1.73/12.34 | 1870 |
| 23, 21 | | 3 | 2.41 | 12.42 | 4.42 | 0.87/8.52 | 1291 |
| Double concentric ring | | | | | | | |
| *outer ring (o.r., i.r.)* | *inner ring (o.r., i.r.)* | *Disc (radius)* | | | | | |
| 14, 13 | 9, 8 | 4 | 29.92/59.84/29.92 | 8.65 | 8.72 | 35.27/112.05/59.52 | 16977 |
| 17, 15 | 11, 9 | 4 | 28.67/57.34/28.67 | 9.56 | 10.06 | 4.26/45.63/57.04 | 8642 |
| 67, 65 | 17, 15 | 4 | 2.10/4.20/2.10 | 28.80 | 23.26 | 0.25/2.09/4.18 | 633 |
| 17, 15 | 11, 9 | – | 7.30/7.30/0[a] | 12.67 | 4.48 | 3.63/5.81/0 | 880 |
| 14, 13 | 9, 8 | 4 | 8.99/9.59/0.60[a] | 11.72 | 4.12 | 0.60/17.96/1.19 | 2721 |
| 17, 15 | 11, 9 | 4 | 7.83/8.43/0.60[a] | 12.85 | 4.60 | 3.89/6.71/1.19 | 1017 |
| 67, 65 | 17, 15 | 4 | 2.25/5.67/3.42[a] | 28.86 | 23.27 | 0.27/2.82/6.80 | 1030 |

**Table 1. Summary of evaluated electrode configuration/geometries equivalent currents and focality**. For each electrode configuration and geometry evaluated, the equivalent current ($I_{eq}$) corresponding to the total *surface* electrode current required to produce a 0.328 mV/mm field, 1 mm below the cortical surface, was determined. For each configuration the surface-space constants were determined, corresponding to the distance from the location of peak electric field along the brain surface, to where the field decreased to 0.207 mV/mm (63.21% of peak). The depth-space constants were determined, corresponding to the distance from the cortical apex toward the brain centre, where the field decreased to 63.21% of its value at the apex. The distal electrode-surface current density (DESCD: total current/area) for all configurations is also indicated. Note that the current density 1 mm below the cortical surface (CSCD) is 0.0066 mA/cm$^2$ for all cases due to use of $I_{eq}$. For the DESCD/CSCD ratio, maximal values of DESCD where considered. These indicators provide only broad pointers of how efficient each configuration is in guiding current into the brain (as opposed to along the scalp surface) and localizing stimulation to superficial cortical regions. For any given application, these metrics may not necessarily indicate increased efficacy of safety (see discussion). (Note: 'o.r.', 'i.r.', 'DESCD' and 'CSCD' refer to 'ring outer radius', 'ring inner radius', 'distal electrode-surface current density', and 'cortical surface current density' respectively).

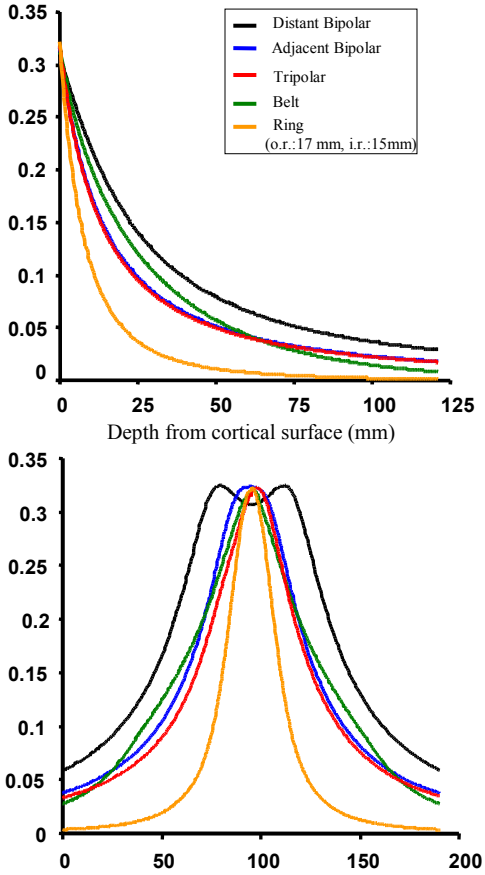


**Figure 2. Electric field profiles along cortical surface and brain depth induced by varied surface stimulation electrode configurations.** For the five electrode configurations illustrated in Figure 1, the line plots of electric field magnitude along the cortical surface midline and down the brain cross-section midline are overlaid. Note that the equivalent current for each configuration has been adjusted ($I_{eq}$) to produce a 0.328 mV/mm peak electric field, 1 mm under the cortical surface. The peak electric field in all configurations is at the head apex except for distant-bipolar where two peaks are observed corresponding to the two stimulation sites. (Note: 'o.r.' and 'i.r.' refer to 'ring outer radius' and 'ring inner radius', respectively).

**Figure 3. Finite element model of brain electric fields induced by double concentric-ring stimulation electrode configurations**. For the double concentric-ring configuration, we considered energizing either only two electrodes (with one electrode insulated/removed) or energizing all electrodes ('tripolar' modulation at two ring electrode geometries). For the five conditions illustrated, the total electrode current ($I_{eq}$) was adjusted to produce a peak 0.328 mV/mm field, 1 mm below the cortical surface. The top row diagrams the electrode configuration; the ring electrode radii and current was varied. The inner ring was energized as the only cathode and the disk electrode had 4 mm radius in all cases. The remaining rows plot the induced electric fields in varied planes and directions. For each case, neuronal modulation was represented using *surface-magnitude*, *surface-radial, surface-tangential, surface-radial ±, cross-section magnitude*, *cross-section-radial,* and *cross-section-tangential* (see Methods). Column 1: Energizing only the central disk electrode and the inner ring (ring 2) duplicates the single concentric-ring configuration. Column 2: Energizing only the two ring electrodes results in dominantly radial modulation under the rings. Column 3, 4: Energizing all electrodes (with total anodic current at the centre disk and outer ring matched) resulted in a modulation 'ring' that scaled with electrode size, surrounding a centered un-stimulated region. Column 5: Asymmetric current at each anode resulted in a more distinct ring modulation region. Note that the relatively high $I_{eq}$ for double concentric-rings results from significant skull/scalp shunting but that peak *brain* electric field (and hence current density) is normalized across all cases. All surface/cross-section electric field plots are on the indicated spatial scale. All dimensions are in mm. (Note: 'o.r.', 'i.r.', 'Mag', and 'Tang' abbreviate 'ring outer radius', 'ring inner radius', 'magnitude', and 'tangential', respectively).

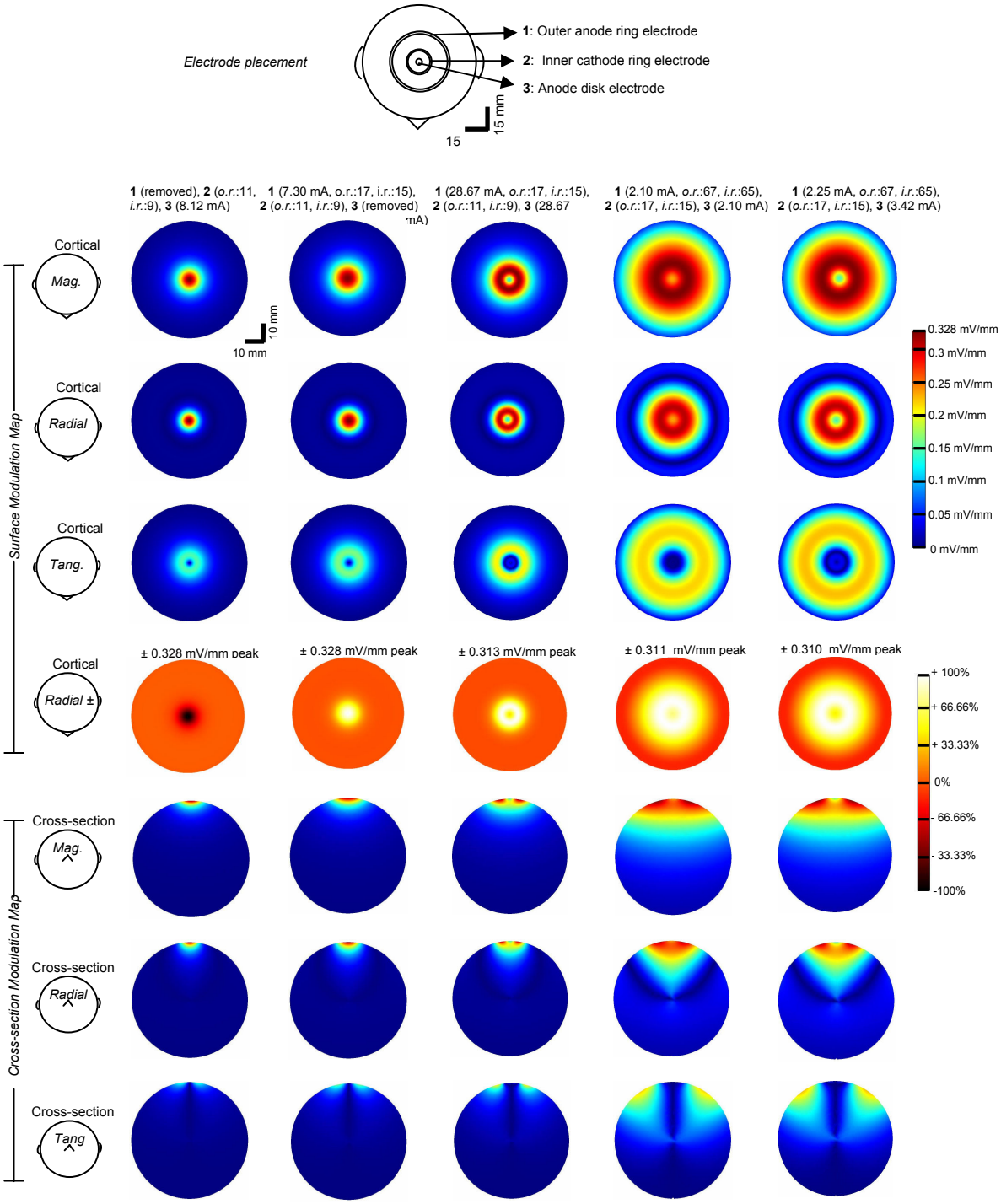
Electrode placement
1: Outer anode ring electrode
2: Inner cathode ring electrode
3: Anode disk electrode
15 mm
15
1 (removed), 2 (o.r.:11, i.r.:9), 3 (8.12 mA)
1 (7.30 mA, o.r.:17, i.r.:15), 2 (o.r.:11, i.r.:9), 3 (removed)
1 (28.67 mA, o.r.:17, i.r.:15), 2 (o.r.:11, i.r.:9), 3 (28.67 mA)
1 (2.10 mA, o.r.:67, i.r.:65), 2 (o.r.:17, i.r.:15), 3 (2.10 mA)
1 (2.25 mA, o.r.:67, i.r.:65), 2 (o.r.:17, i.r.:15), 3 (3.42 mA)
Surface Modulation Map
Cortical Mag.
Cortical Radial
Cortical Tang.
Cortical Radial ±
10 mm
10 mm
0.328 mV/mm
0.3 mV/mm
0.25 mV/mm
0.2 mV/mm
0.15 mV/mm
0.1 mV/mm
0.05 mV/mm
0 mV/mm
± 0.328 mV/mm peak
± 0.328 mV/mm peak
± 0.313 mV/mm peak
± 0.311 mV/mm peak
± 0.310 mV/mm peak
+ 100%
+ 66.66%
+ 33.33%
0%
- 66.66%
- 33.33%
-100%
Cross-section Modulation Map
Cross-section Mag.
Cross-section Radial
Cross-section Tang

## 3.4 Discussion

*Precision of reduced head model*

The accuracy of any given stimulation model is restricted by the calculation of accurate voltage profiles and the subsequent prediction of relevant 'modulation' regions from these voltage profiles. The former is limited by the level of inhomogeneity and anisotropy modeled. The advantages of using a reduced concentric-sphere head model for this initial evaluation include the ability to directly compare different configurations / geometries without concomitant complexity related to head asymmetry. Improving the precision of the head model will enhance the accuracy of the electric field calculations; including incorporation of anatomical information from individual MRI scans (De Lucia et al., 2007; Holdefer et al., 2006; Wagner et al., 2007) and conductivity data derived from diffusion tensor imaging (DT-MRI) (McIntyre et al., 2004). We note that our distant-bipolar calculations are in general agreement with previous tDCS stimulations using concentric spheres (Miranda et al., 2006) and MRI-based anatomy (Wagner et al., 2007). The results reported here using the optimized electrode configurations thus represent an important 'proof-of-principle' supporting further characterization.

*Cortical Modulation Functions (maps): Representation of relevant Modulation regions*

Transcranial stimulation generates extracellular voltage gradients (electric fields) inside the head and these fields will lead to polarization of sections of neuronal

membrane. This induced membrane polarization will affect a range of functional/cellular properties. Relatively strong supra-threshold electric fields will trigger action potentials. Sub-threshold fields can modulate the firing properties of neurons (e.g. action potential threshold / timing (Jefferys, 1981; Radman et al., 2007), synaptic efficacy (Bikson et al., 2004), and neuronal information processing (Deans et al., 2007; Jefferys et al., 2003). It is important to note that in response to any electric field, different compartments of the same neuron will simultaneously either depolarize or hyperpolarize (Jefferys, 1981; Jefferys et al., 2003; Ranck, 1975). Thus the complex "modulation" by electric stimulation cannot necessarily be explained by a simple "increase" or "decrease" in excitability.

It is well established that the 'point' extracellular voltage generated by applied stimulation does not provide a useful indication of neuronal modulation; for this reason proximity to anode or cathode does not either provide meaningful information on cell modulation. Rather, the *spatial distribution* of extracellular voltages (electric field) is applied to a modulation function (which may also include information on neuronal geometry, membrane biophysics, synaptic properties) that determines neuronal modulation at each location. The classic "Activating Function" considers the electric field *derivative* along each membrane segment (Plonsey and Barr, 1995; Rattay, 1986, , 1989; Stecker, 2005).

In determining 'cortical modulation functions' in this study, we considered the electric field magnitude induced in the brain ('surface-magnitude' and 'cross-section

magnitude' plots/space-constants) and the cortical electric field in either the radial ('surface-radial' / 'cross-section radial' plot) or tangential ('surface-tangential' / 'cross-section tangential' plot) directions. The consideration of electric field (as opposed to the electric field derivative / classical activating function (McIntyre and Grill, 1999; Rattay, 1998; Tranchina and Nicholson, 1986) may be a suitable approximation if for transcranial current stimulation, the induced electric field is locally uniform on the scale of any given neuron (Figure 1) and neuronal modulation is directly related to uniform electric field amplitude. The latter is supported by experimental and theoretical studies showing; 1) polarization of short or bent cortical axons is linear with (sub-threshold) electric field amplitude (Amassian et al., 1992; Maccabee et al., 1993; Nagarajan et al., 1993; Plonsey and Altman, 1988; Roth, 1994; Tranchina and Nicholson, 1986); 2) synaptic efficacy is quasi-linear with electric field amplitude (Bikson et al., 2004); 3) somatic and dendritic process polarization is linear with (sub-threshold) uniform electric field amplitude (Bikson et al., 2004; Chan et al., 1988; Chan and Nicholson, 1986; Hause, 1975); and 4) metrics of neuronal excitability vary with electric field amplitude (Amassian et al., 1994; Bikson et al., 2004; Ghai et al., 2000; Gluckman et al., 1996; Jefferys et al., 2003; Komssi et al., 2007; Krings et al., 1997; Miranda et al., 2003; Wassermann et al., 1996).

The above reports reinforce that uniform electric fields preferentially polarize neuronal structures oriented parallel to the direction of the field. Whereas our magnitude plots assume no coherent neuronal geometry, radial and tangential plots represent modulation of cortical structures oriented preferentially normal to the cortical surface (e.g. superficial cortical pyramidal neurons) or parallel to the surface (e.g. axons of

passage, deeper cortical neurons), respectively (Kowalski et al., 2002; Rushton, 1927). For example, based on animal studies (Gartside, 1968; Purpura and McMurtry, 1965) and simulations (Rattay, 1986), inwardly directed radial fields under anodes would be expected to depolarize the soma and simultaneously hyper-polarize the apical dendrites of superficial (hence radially oriented) primary cortical neurons (Surface-radial ± plots, Figure 1 and Figure 3).

Consistent with previous studies, we found that maximal *magnitude* electric fields were observed in the cortical regions under *and* between electrodes. However, we report that consideration of specific electric field direction (structure orientation) changes the modulation profile. For example, the surface-radial electric field (presumably superficial cortical pyramids) modulation region for bipolar stimulation restricts modulation to *only* regions under the electrodes (between electrodes the electric field is tangential); this is consistent with clinical observations that neuronal modulation is restricted to regions under electrodes (Nitsche et al., 2007). Similarly, consideration of surface-radial electric fields further enhances the efficacy of the belt configuration relative to the adjacent-bipolar configuration (Belt: 0.328 mV/mm radial field per 0.97 mA; Adjacent-bipolar 0.243 mV/mm radial field per 1.43 mA), consistent with clinical observations (Rossini et al., 1985). Electric field orientation-specific modulation maps (Figure 1) may thus provide practical clinical guidelines not apparent from magnitude plots.

Interestingly, the tripolar configuration produces distinct radial modulation region and tangentially modulated regions. This configuration may thus be used to probe the functional/therapeutic significance of sub-threshold tangential electric fields.

Ring configurations generally favor surface radial modulation. For belt, concentric-ring, and double concentric-ring configurations, the similarity between surface-magnitude and surface-radial plots (reflecting relatively small tangential currents) reduces ambiguity on appropriate modulation representation. In addition, surface-radial ± plots illustrate that with these circular configurations, bi-directional modulation effects are avoided.

Our cortical modulation maps do not explicitly consider neuronal geometry inhomogeneity, which would require complex reproduction of cortical gyri and sulci, as well as neuronal (cortical layer) sub-types. The assumption that superficial cortical neurons, located at gyri crowns, are preferentially modulated is consistent with the rapid decay in field intensity with cortical depth (Figure 1 *Cross-sections*, Table 1). Our surface cortical modulation maps (1 mm below the cortical surface; Figure 1) may thus, to a first approximation, predict stimulation effects on these relatively homogenous oriented superficial cortical neurons. Indeed, our results with the bipolar configuration are consistent with clinical observations (see above), and the general clinical finding that anodal/cathodal field induce reliable and distinct effects support a relatively homogenous target neuronal population. Nonetheless, the predictions made in this study, regarding optimized electrode configurations and orientated-modulation maps, should be

experimentally verified (Nitsche et al., 2007) and corroborated with anatomically detailed models.

Since the static field approximation in our model implies linearity of the electric field solution, our induced electric field *spatial profile* results can be extrapolated to a wide range of stimulation waveforms (e.g. pulsed or AC fields, (Calancie et al., 1998; Marshall et al., 2006; Nadeem et al., 2003; Schroeder and Barr, 2001) and scale linearly with stimulation magnitude (e.g. 260 μA-2 mA tDCS and >350 mA TES (Rossini et al., 1985). However, the induced electric field magnitude (e.g. sub/supra threshold stimulation) and temporal waveform (e.g. frequency) will affect the appropriate *modulation function* (Bikson et al., 2001; Deans et al., 2007; Durand and Bikson, 2001; Francis et al., 2003; MacDonald, 2002) and the accuracy of our simplified (locally uniform) electric field-based modulation maps.

*Optimization of electrode configuration/geometry: efficacy and safety*

The optimal electrode configuration/geometry will depend on the TCS application. However, spatial focality, cellular type specificity, and avoidance of bi-directional modulation at return electrodes are generally desired. As a rule, increasing the distance between stimulation electrodes (or equivalently increasing ring diameter) decreases the current portion shunted through the skull/scalp, and increases the relative current crossing the brain, while reducing spatial focality. Placing electrodes proximal to each other increases focality at the expense of total equivalent current (to obtain

comparable efficacy with remote electrodes). Thus, when comparing electrode configurations, increased electrode current or electrode current density, does not necessarily equate with increased brain modulation (cortical electric fields).

Concerns about TCS safety generally focus on total electrode current, electrode-surface current density (current / area), total charge (current × stimulation duration), or total charge density (total charge/electrode area) (Merrill et al., 2005; Nitsche et al., 2003b; Poreisz et al., 2007; Priori, 2003a). We note that (charge related) electrochemical product may not be an issue for acute noninvasive stimulation (Durand, 2007) and that the magnitude of scalp sensation does not correlate with threshold of brain stimulation (Nitsche et al., 2003b; Suihko, 2002). Here we propose a supplementary safety consideration of a normalized peak cortical field, reportable as equivalent currents ($I_{eq}$) to a "standard" configuration (1 mA, distant-bipolar). Rational stimulation design may balance scalp current density and equivalent current (cortical electric field) factors (Table 1). Nitsche et al. (2007) demonstrated that during tDCS bipolar stimulation with different size square electrodes, calculated electrode-surface current density (1 mA/35 $cm^2$) roughly standardizes cortical response. Standardization to calculated electrode-surface current density (total current/electrode area) assumes that current density at the scalp scales consistently with current density at the brain; this assumption does not necessarily hold across electrode configurations (Table 1; in part because of differences in fractional scalp/ skull loss) or for relatively small electrodes. For example, a micro-electrode (0.01 $cm^2$ area) with 'standardized' current density (1 mA/35 $cm^2$ × 0.01 $cm^2$ = 0.0003 mA current) will not be effective. In addition, current density is not uniform on the electrode

surface (Miranda et al., 2006). Nonetheless, approximated uniform electrode-surface current density (total current/electrode area) remains a useful functional/safety metric because it presumably places an upper limit on current density, and hence electric field in the brain; assuming current density diffusion through skull (Saypol et al., 1991; Stecker, 2005; Suihko, 1998; Wagner et al., 2007) offsets current density concentration at the electrode edges (Miranda et al., 2006) .

For any given application and temporal waveform (e.g. tDCS for depression, ECT for depression, CES for pain), an appropriate $I_{eq}$ multiplying factor can be determined (desired peak cortical electric field in mV/mm / 0.328 mV/mm). For a *given therapy and temporal waveform*, the $I_{eq}$ multiple factor should be kept constant when changing electrode positions/configuration in order to elicit similar peak cortical fields thus maintaining efficacy and safety; however the $I_{eq}$ will vary with electrode configuration and hence so will the total applied current. For this reason when changing configurations, maintaining total applied current (electrode current density, electrode charge) may not be appropriate. Since the spatial profile of the induced electric field is independent of waveform and application, the *relative* spatial focality of different electrode configurations may be directly compared by normalizing to peak cortical electric field (using $I_{eq}$); and the resultant directional modulation maps generated in this way can be used to predict relative structural targeting (Figure 1, 3).

TES and electroconvulsive therapy both have electrode-surface current densities significantly exceeding 1 $mA/cm^2$ and apply currents > 100 × $I_{eq.}$ However, because of

difference in stimulation waveform (e.g. number of pulses) and desired clinical outcome, efficacy and safety considerations for TES and electroconvulsive therapy are undamentally different. The $I_{eq}$ multiple does not in itself define stimulation effects, without explicit consideration of waveform and therapy factors.

Approaches using multiple electrodes and varying electrode geometries have been well characterized for peripheral nerve stimulation (Durand, 2007). Concentric-ring electrode configurations (consisting of a centre electrode surrounded by a ring electrode) and ring electrodes have been previously used for peripheral nerve / muscle fibre stimulation (Rattay, 1989), producing anesthetic effects (Oda and Fujitani, 1990), and seizure control (Besio et al., 2007). Analytical solutions for concentric-ring stimulation of homogenous tissue have been proposed (van Oosterom and Strackee, 1983). The mathematically complimentary principle of using ring electrodes to improve the spatial focality of bio-potential recording has been applied for EEG (Besio et al., 2006b), EMG (Farina and Cescon, 2001), and ECG signals (Besio et al., 2006a). Our results indicate that the focality of clinical TCS stimulation, targeting radially-oriented superficial structures, can be markedly increased by appropriate application of concentric-ring stimulation electrodes.

In summary, control of surface electrode geometry (shape and number) will modulate both the structural specificity and spatial focality of TCS stimulation. Optimization of focality must be balanced against increased electrode current density and scalp/skull current (which may not necessarily reflect safety concerns). The

configurations explicitly considered in this report can be combined and indeed serve only to illustrate principles of design. Our results thus support the future development of TCS technology incorporating rationally-designed (Bikson et al., 2006) target-specific (pathology, structure) electrode configurations.

# Chapter 4: Gyri-precise head model of transcranial direct current stimulation: Improved spatial focality using a ring electrode versus conventional rectangular pad

## 4.1 Introduction

Conventional transcranial direct current stimulation (tDCS) involves weak direct currents (260 μA – 2 mA) applied to the scalp via sponge-based rectangular pads (nominally 25 - 35 $cm^2$) (Hummel et al., 2005; Iyer et al., 2005; Marshall et al., 2005; Nitsche and Paulus, 2000). tDCS modulates cortical function and has been applied to facilitate learning, alter behavioral performance, and improve impaired brain function (Antal et al., 2004a; Boggio et al., 2007; Boggio et al., 2006; Boggio et al., 2009a; Fregni et al., 2006b; Kincses et al., 2004; Liebetanz et al., 2006; Nitsche et al., 2003d; Uy and Ridding, 2003).

A pivotal factor for tDCS efficacy and safety is the spatial extent of induced cortical electric fields/current density. tDCS is considered to be poorly focused using rectangular-pad electrode configurations (Datta et al., 2008; Nathan et al., 1993; Nitsche et al., 2007; Rossini et al., 1985). The spatial focality of induced cortical electric field (EF)/current densities has been proposed to increase using reduced electrode sizes (Datta et al., 2008; Kwon et al., 2008; Nitsche et al., 2007), appropriate placement of electrodes (Borckardt et al., 2009a; Datta et al., 2008; Nathan et al., 1993), and ring electrode configurations (Datta et al., 2008). However, the precise role of complex tissue-

compartment morphology in influencing the flow of currents during tDCS has not been systematically addressed, including potential discrete cortical "hotspots" (clustering) of induced electric fields (Kanai et al., 2008; Miranda et al., 2006; Wagner et al., 2007).

During any transcranial current stimulation modality, the current which reaches the cortex is significantly altered from the applied scalp current due to intermediate tissue properties. A portion of the injected current is shunted across the scalp. The portion which crosses into the skull is then conducted by cerebrospinal fluid (CSF). Through the highly conductive CSF network, current can eventually cross into the brain. In the case of DC stimulation, induced cortical currents / electric fields have been shown to modulate the firing properties of neurons and 'condition' neuronal excitability (Bikson et al., 2004; Bindman et al., 1964; Gartside, 1968; Purpura and McMurtry, 1965; Radman et al., 2007). There is a general perception that the low conductivity of skull places a severe limit on the spatial focality of brain modulation.

One objective of this study was to compare the focality of 'conventional' 7 X 5 $cm^2$ rectangular-pad stimulation with the 4 X 1 ring electrode configuration using a high resolution MRI-based finite element model of the human head. Spherical-based (Datta et al., 2008; Miranda et al., 2006) and MRI-derived (Oostendorp et al., 2008; Wagner et al., 2007) head models have previously been used to calculate tDCS electric fields. In this study, we incorporated gyri/sulci specificity by developing a model with 1 $mm^3$ resolution. Induced cortical electric fields were used to predict relative spatial focality and the influence of tissue geometry/conductivity. We report that tDCS modulation maps

are fundamentally influenced by detailed cortical architecture and consider limitations on transcranial stimulation focality

## 4.2 Methods

Volume conductor models were created with the same resolution (1 $mm^3$) as the MRI data used to derive them. Raw 3T MRI scans were contrast enhanced and noise filtered. The head was segmented into compartments representing the brain tissue, cerebrospinal fluid (CSF), skull, muscle, fatty tissue, eyes, blood vessels and the scalp respectively (Figure 4,A; SIMPLEWARE Ltd., Exeter, UK). The stimulation rectangular pads and discs were imported as CAD models (see below). The volumetric mesh was generated (minimum quality factor > 0.5) from the segmented data and eventually exported to COMSOL Multiphysics 3.4 (COMSOL Inc., MA, USA). The resulting mesh comprised >10,000,000 tetrahedral elements (>15,000,000 degrees of freedom).

The electrical properties of the tissues were assigned representative isotropic average values (in S/m): brain: 0.2; CSF: 1.65; skull: 0.01; scalp: 0.465 (Akhtari et al., 2002; Baumann et al., 1997; Gabriel et al., 1996; Geddes and Baker, 1967; Hauesien et al., 1997; Holdefer et al., 2006; Nadeem et al., 2003). The muscle, fatty tissue, eyes and blood vessel compartments were assigned the conductivity of scalp tissue.

We modeled two electrode configurations:

(1)‘Rectangular-pad’ (Figure 4,B): Two pads (7 X 5 $cm^2$) were placed at sites commonly used for tDCS of the primary motor cortex, with the “active” (anode) electrode over the left motor cortex and the “return” (cathode) electrode at the forehead above the contralateral orbita. Typically, the rectangular sponges are soaked in saline for conventional tDCS application and the abutting electrode is energized. The sponge was therefore assigned the conductivity of saline: 1.4 S/m.

(2)‘4 X 1 ring’ (Figure 4,C): In order to practically implement the concentric-ring configuration (Datta et al., 2008), we approximated a ring using four “return” (cathode) disc electrodes arranged in a circular fashion around an “active” (anode) center electrode. The active electrode is placed over the motor cortex (coinciding with the center of the active pad used for rectangular-pad stimulation) and surrounded by four return electrodes (each at a disc center to disc center distance of 3 cm from the active electrode). The disc electrodes had a 4 mm radius. The 4 X 1 ring electrode system was implemented by passing current through disc electrodes into the scalp using a customized tDCS gel (CCNY-4) with conductivity: 0.3 S/m.

All electrodes had a thickness of ~ 1 mm and were modeled as conductors with the conductivity of copper: 5.8 x $10^7$ S/m. The thickness of the CCNY-4 gel was ~ 2 mm while the thickness of the sponge varied from 1 to 2.5 mm (thickness changed with scalp curvature in order to maintain continuous contact).

The Laplace equation $\nabla.(\sigma\nabla V)=0$ (V: potential; $\sigma$: conductivity) was solved and the boundary conditions used were (1) inward current flow = $J_n$ (normal current density) applied to the exposed surface of the anode electrode, (2) ground applied to the exposed surface of the cathode electrode(s) and (3) all other external surfaces treated as insulated.

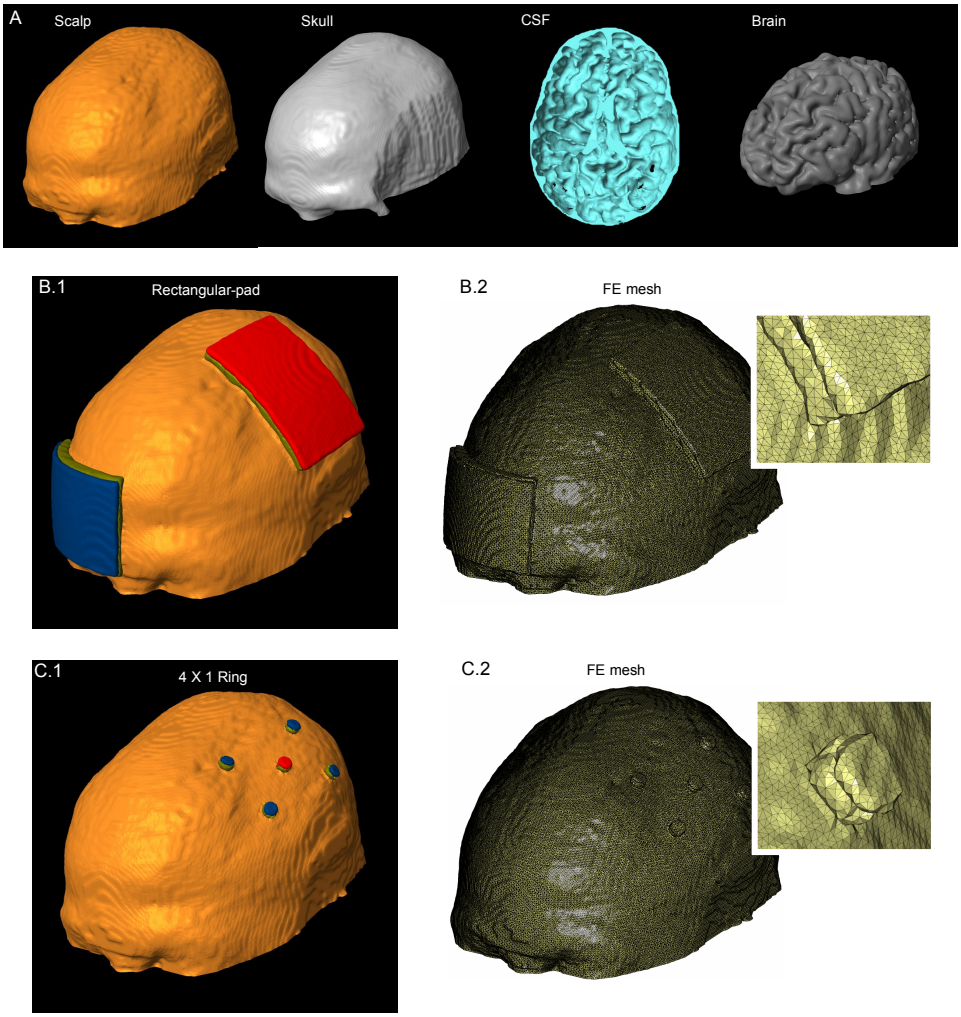


**Figure 4. Finite element (FE) model of the conventional 7 X 5 cm$^2$ rectangular-pad and 4 X 1 ring configurations.** (A) Segmented compartments in the following order: Scalp, Skull, CSF and Brain. (B.1) FE model of the conventional rectangular-pad configuration and corresponding FE mesh (B.2). (C.1) FE model of the 4 X 1 ring electrode configuration and corresponding FE mesh (C.2). The two insets show the zoomed mesh images, highlighting finer detail. 'Red': Anode electrode; 'Blue': Cathode electrode(s); 'Olive green': sponge/gel.

Current densities corresponding to 1 mA total current for the rectangular-pad configuration and 2 mA total current for the 4 X 1 ring configuration were respectively applied.

These currents resulted in similar peak cortical induced EF magnitude for each of the configurations. The finite element method (FEM) model was implemented using COMSOL. The linear system solver of conjugate gradients was used with a relative tolerance of $1 \times 10^{-6}$.

'Surface-magnitude' plots were generated by plotting the magnitude of EF on the surface of brain tissue. In addition, 'Cross-section magnitude' plots were generated by plotting the EF magnitude on coronal slices (Datta et al., 2008). Because the conductivity of brain is uniform, these same plots also represent induced current density profiles (where the actual current density values can be scaled using: $J = \sigma.E$).

In this study, the induced brain electric field magnitude was assumed to correlate with the degree of brain "modulation". The consideration of the electric field (as opposed to the classical activating function) may be appropriate if: 1) tDCS induced electric fields are uniform at the scale of a neuron; and 2) neuronal modulation may be directly correlated with uniform electric field magnitude (Amassian et al., 1992; Bikson et al., 2004; Chan and Nicholson, 1986; Datta et al., 2008; Nagarajan et al., 1993; Tranchina and Nicholson, 1986). Our electric field magnitude modulation maps do not consider any

specific neuronal orientation (and target non-oriented structures) (Bikson et al., 2008; Datta et al., 2008).

### 4.3 Results

For the 7 X 5 $cm^2$ rectangular-pad and the 4 X 1 ring configuration models (Figure 4,B and Figure 4,C), we calculated the induced electric field/current density magnitude in the brain. The surface-magnitude/cross-section magnitude EF plots for each of the configurations allow a direct comparison of relative cortical surface and depth focality (Figure 5).

Rectangular-pad stimulation with 7 X 5 $cm^2$ pads results in widespread diffuse (un-focal) modulation over the entire cortical surface owing to the large size and separation of pads (Figure 5,A.2). 1 mA injected through the pads results in 0.67 V/m peak cortical EF magnitude (encompassed in dashed region of Figure 5,A.2; expanded in Figure 5,A.4) in the walls of a frontal lobe gyrus. The peak cortical EF magnitude of 0.67 V/m corresponds to 0.13 $A/m^2$ peak cortical current density magnitude. The local EF magnitude peak directly underneath the pads was 0.45 V/m. The minimum cortical induced EF magnitude in the entire frontal area of the brain was ~ 0.16 V/m (see coronal slice, Figure 5,A.6) and ~ 0.06 V/m in the occipital area.

The presence of distinct clusters of EF magnitude maxima (Figure 5,A.2) was influenced by regions of reduced skull thickness, which may provide preferential current

pathways of current crossing into the CSF (see also Figure 6), as well as channels of high-conductivity CSF bounded by brain and skull. For example, a particular gyrus may have high induced EF magnitude due to wide pockets of CSF on either side acting as a current "sink" (Holdefer et al., 2006) as well as reduced CSF thickness over that gyri crown acting as a "funnel".

The 4 X 1 ring configuration leads to a significant increase in spatial focality (Figure 5,B.2). Peak electric field magnitude is observed in the gyri and the intermediate sulcus directly underneath the active stimulation electrode (see coronal slice, Figure 5,B.6). The region of modulation is generally constrained between the active electrode and the four return electrodes with a 0.44 V/m EF magnitude peak (encompassed in dashed region of Figure 5,B.2; expanded in Figure 5,B.4). Thus, using the 4 X 1 ring configuration, 2 mA resulted in a comparable peak EF magnitude in the motor cortex as 1

**Figure 5. Brain modulation during tDCS using conventional rectangular-pad (A.1) and the 4 X 1 ring electrode configuration** (B.1). 'Red': Anode electrode; 'Blue': Cathode electrode(s); 'Olive green': sponge/gel. For each configuration, we calculated the induced cortical electric field (EF) magnitude. (A.2, B.2) S*urface-magnitude* plots of EF along the brain surface, same view as (A.1, B.1). The dashed region is expanded in inset. (A.3, B.3) *Top view* of the brain showing the induced s*urface-magnitude* EF. The insets (A.4) and (B.4) show the zoomed *surface-magnitude* EF plots. These images are obtained with "lighting" on [COMSOL Multiphysics] to highlight gyri/sulci modulation. (A.5, B.5) *Cross-section magnitude* EF plotted on a series of successive cortical slices, same view as (A.1, B.1). The *cross-section magnitude* EF plots for two slices and their corresponding MRI scans are shown in (A.6), (B.6). One slice is chosen directly from underneath the rectangular-pad/active electrode of 4 X 1 ring configuration and another from the prefrontal area of the brain. The same slices are shown for each of the configurations. All plots are normalized between zero and the peak positive cortical EF magnitude: conventional rectangular-pad peak = 0.67 V/m (or 0.13 A/m$^2$ current density peak); 4 X 1 ring peak = 0.44 V/m. (Note that for the rectangular-pad, the EF magnitude peak is observed between the pads and not underneath).

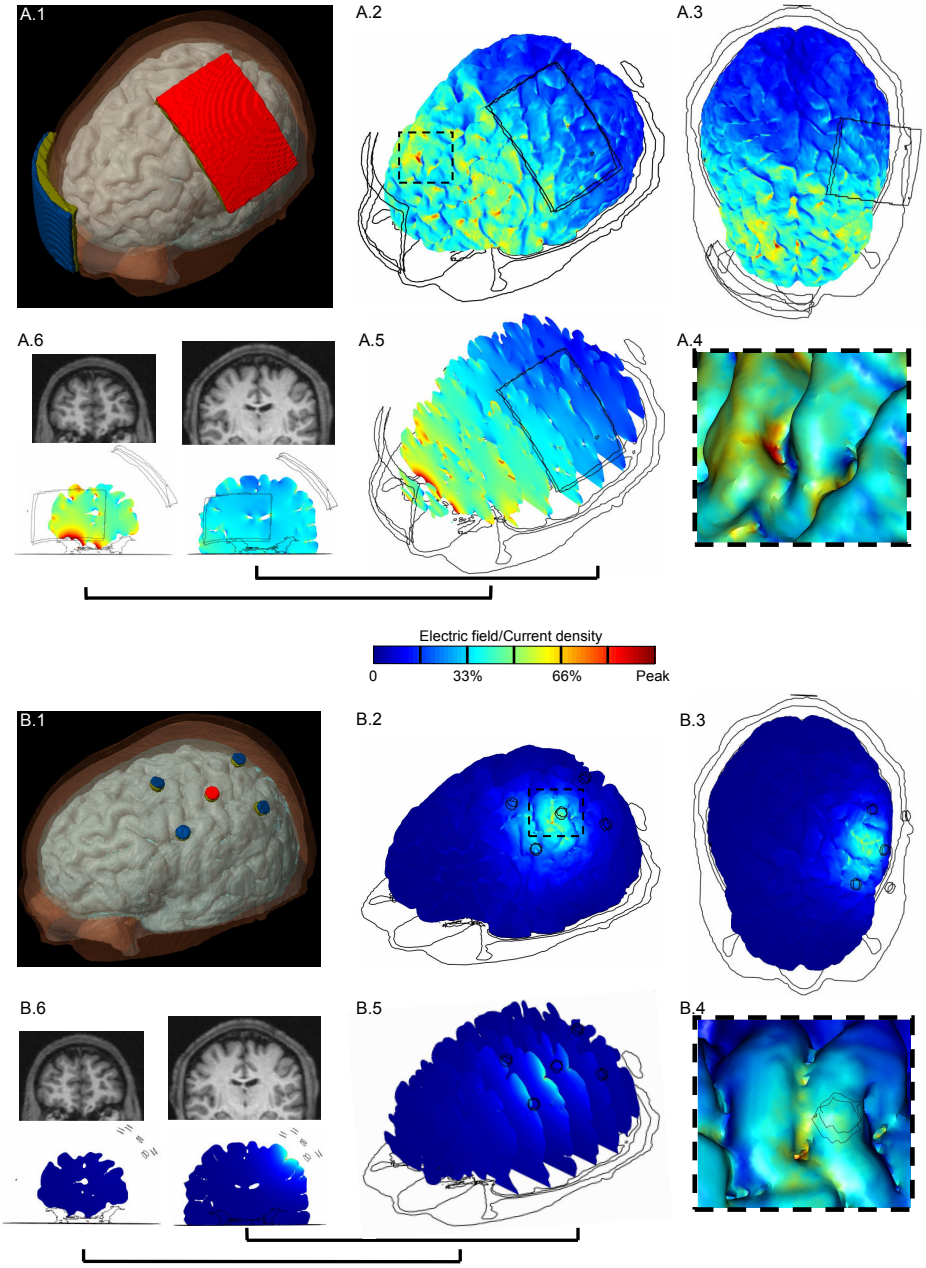
A.1
A.2
A.3
A.6
A.5
A.4
Electric field/Current density
0
33%
66%
Peak
B.1
B.2
B.3
B.6
B.5
B.4

mA rectangular-pad (7 X 5 $cm^2$) stimulation. However, for the 4 X 1 ring configuration, there was no cortical modulation (< 0.01 V/m) in the frontal regions, on the contralateral (right) motor regions of the brain, or on the occipital lobe of the brain. The overall spatial profile of brain modulation was strongly influenced by tissue inhomogeneity, notably due to CSF (Figure 6).

### 4.4 Discussion

The translation of stimulation models to clinical applications requires reproducing application-appropriate anatomical features (Butson et al., 2007; De Lucia et al., 2007; Deng et al., 2008; Holsheimer, 1998; Im et al., 2008; Johnson and McIntyre, 2008; Wongsarnpigoon and Grill, 2008). The incorporation of gyri/ sulci specificity in our 3D human head model can guide rational tDCS design and optimization (Bikson et al., 2008; Bikson et al., 2006).

The overall current flow due to any transcranial electric stimulation is complex and is influenced by a convergence of factors including: 1) electrode size/geometry and separation-distance, with related scalp shunting (Datta et al., 2008); 2) skull thickness, presence of sutures and eye cavities; 3) channels of high conductivity CSF enclosing/and perfusing the underlying cortex; 4) convoluted brain surface morphology; and 5) differences in tissue conductivities at boundaries between tissue compartments.

tDCS using conventional 'large' rectangular pads resulted in diffuse (un-focal) cortical modulation. Moreover, the complex geometry of the brain and regional differences in conductance cause local non-uniformities of current density through the CSF (e.g. "sinks" and "funnels") that are reflected in clustering of brain electric field magnitude at distinct sites. Indeed, some imaging and physiological studies suggest diffuse brain modulation and clustering of regional cerebral blood flow/EF, independent of anatomical connections (Kanai et al., 2008; Lang et al., 2005). Separate imaging, TMS mapping studies and, clinical studies indicate some level of functional spatial selectivity (Antal et al., 2004b; Boggio et al., 2007; Kincses et al., 2004; Nitsche and Paulus, 2000; Nitsche et al., 2003d); which may be explained by FE models with more specific modulation maps (Datta et al., 2008) including non-linearities and thresholding.

Whereas our electric-field magnitude modulation maps assume no particular neuronal geometry or waveform dependent biophysical transduction mechanisms, direction-specific modulation maps incorporating cellular orientation (radial versus tangential) (Datta et al., 2008) and electric field derivative (classical activating function) (Plonsey and Barr, 1995; Rattay, 1986) have been applied elsewhere (Johnson and McIntyre, 2008; Wongsarnpigoon and Grill, 2008). In cases of pulsed or AC stimulation waveforms, the appropriate modulation map (parameter/function that determines degree of brain "modulation") may differ (Kanai et al., 2008; Lisanby, 2007; Terney et al., 2008).

Any FE human head model is limited by the accuracy of tissue dimensions and conductivity values incorporated (inhomogeneity and anisotropy). The present study investigated the distribution of tDCS induced currents in brain using a highly detailed anatomical model. The high MRI scan resolution (1 $mm^3$) allows accurate segmentation of individual tissue compartments. Consequently the precise 3D model rendered, captures anatomical detail such as cortical folding (Figure 5,A.4). Finally the precise FE mesh generated (> 10 million elements), allows accurate computation of induced fields. The importance of incorporating gyri/sulci specificity is highlighted by the observance of clustering of brain modulation during conventional tDCS (see also Figure 6). Our results also suggest that individual variability would affect the magnitude and spatial extent of cortical electric fields. For example, young children have vascularized fontanels, there are differences in the degree/timing of suture closing amongst adults (Holdefer et al., 2006), and elderly subjects have larger fractional CSF volumes (Murphy et al., 1992).

Our results indicate that the focality of clinical tDCS application can be significantly enhanced by the 4 X 1 ring configuration. Additionally, since the peak induced cortical electric field magnitude is similar to the rectangular-pad stimulation; the 4 X 1 ring results in more targeted brain modulation (hence potentially, a safer electrode configuration). The cortical current density of 0.09 $A/m^2$ induced underneath the pads by rectangular pad (1 mA) and 4 X 1 ring (2 mA) configurations is more than two orders of magnitude away from the threshold for histopathologically observed tDCS brain damage in a rat model (Liebetanz et al., 2009). We emphasize that using the 4 X 1 ring configuration, the more *surface* current needed does not lead to more peak induced

cortical EF magnitude, but reflects shunting across the scalp (without crossing into the brain)(Bikson et al., 2009a). For skin safety, the increased scalp current associated with 4 X 1 ring can be offset by increasing the separation distance between stimulation electrodes, but at the cost of stimulation focality (Datta et al., 2008). Importantly when using conventional sponge electrodes, the current density at the scalp is in fact concentrated at the sponge edges and thus exceeds the average current density (injected current / electrode surface area) (Miranda et al., 2006). Moreover, electrode materials and design are as pivotal to comfort as is average current density (Dundas et al., 2007; Merrill et al., 2005; Palm et al., 2008); using appropriate hardware (electrode adapters, stimulation gels), 39.8 $A/m^2$ current density may be applied without pain

**Figure 6. Influence of tissue properties on the spatial profiles of electric field/current density magnitudes induced by stimulation with rectangular-pad (A) and 4 X 1 ring (B) electrode configurations.** First column: Simulation results with *inhomogeneous* electrical conductivities. Second column: Simulation results using the same head model but with $\sigma_{CSF} = \sigma_{brain} = 0.2$ S/m. Third column: Simulation results with *homogeneous* tissue conductivity ($\sigma = 0.2$ S/m). Rows A.1 and B.1: Cortical *surface-magnitude* electric fields. Rows A.2 and B.2: Induced *current density* magnitude in both CSF and brain on a single cross sectional slice (same slice as in Figure 2 of manuscript). Rows A.3 and B.3: Cortical *Cross-section magnitude* electric fields. For the rectangular-pad stimulation, sites of high current densities in CSF generally correspond with regions of high induced cortical electric field magnitudes which are reflected as distinct clusters of modulation (see A.2a and A.3a). Note that A.1a and B.1a are same as Figure 3A.2 and 3B.2 in the manuscript. When the brain and CSF compartments have same conductivity, the region of peak induced electric fields roughly encompasses the entire cortical surface between the pads (A.1b). In addition, distinct clustering of electric fields is not observed owing to similar electrical properties and absence of convoluted cortical morphology (A.2b and A.3b). The cortical surface comprising the peak induced EF magnitudes demonstrates regions of reduced skull thickness (A.1b). Two distinct peaks of modulation beneath the two corresponding rectangular pads are observed when homogeneous conductivities are considered (A.1c). For the 4 X 1 ring configuration, the region of peak cortical electric field magnitude corresponds to sites of high induced current densities in CSF (B.3a and B.2a) similar to rectangular-pad simulation. For the homogeneous case and when the brain and CSF compartments have same conductivity, region of peak induced electric fields roughly encompasses the cortical surface between the active and return electrodes (B.1b and B.1c). Note that for the cross-sectional plots (Rows: A.2,A.3,B.2,B.3) the maximum has been scaled for clarity as indicated.

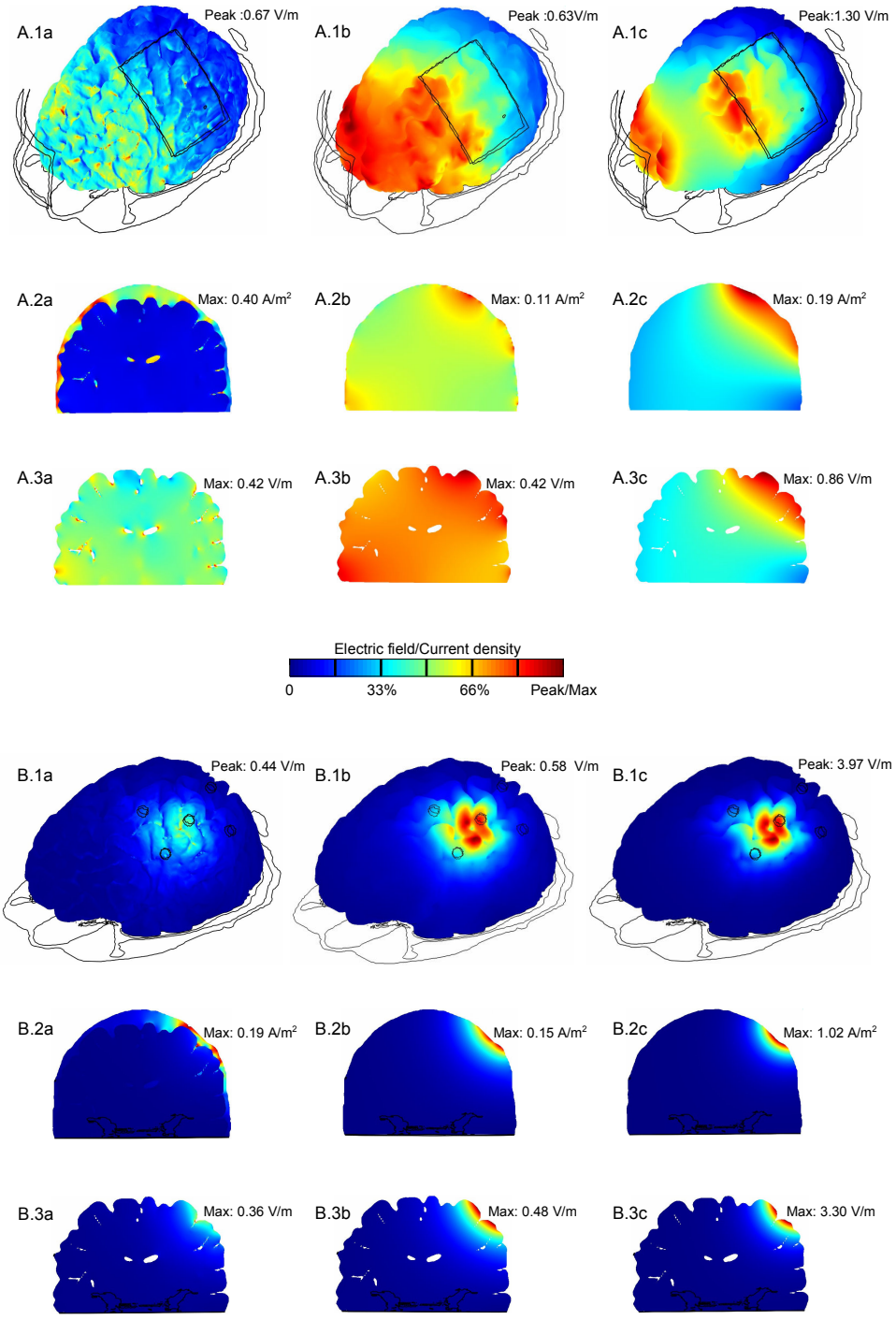
A.1a
Peak :0.67 V/m
A.1b
Peak :0.63V/m
A.1c
Peak:1.30 V/m
A.2a
Max: 0.40 A/m²
A.2b
Max: 0.11 A/m²
A.2c
Max: 0.19 A/m²
A.3a
Max: 0.42 V/m
A.3b
Max: 0.42 V/m
A.3c
Max: 0.86 V/m
Electric field/Current density
0
33%
66%
Peak/Max
B.1a
Peak: 0.44 V/m
B.1b
Peak: 0.58 V/m
B.1c
Peak: 3.97 V/m
B.2a
Max: 0.19 A/m²
B.2b
Max: 0.15 A/m²
B.2c
Max: 1.02 A/m²
B.3a
Max: 0.36 V/m
B.3b
Max: 0.48 V/m
B.3c
Max: 3.30 V/m

(Prausnitz, 1996). Because of the above issues, pain perception for skin should be addressed in a clinical study (Arana et al., 2008). Thus electrode designs that mitigate skin irritation should be developed along with electrode configurations that enhance spatial focality.

The quasi-static field approximation implies conservation and linearity of EF solution. Thus, our EF magnitude 'spatial profile' results can be extrapolated to other transcranial current stimulation modalities (e.g. suprathreshold transcranial electrical stimulation, electroconvulsive therapy, transcranial alternating current stimulation, transcranial random noise stimulation, and cranial electrotherapy stimulation) (Calancie et al., 1998; Kanai et al., 2008; Lisanby, 2007; Schroeder and Barr, 2001; Terney et al., 2008) where the 4 X 1 ring configuration may be used to focally target cortical structures.

The 'transparency' of the skull to magnetic stimulation has led to the development of specialized coils for focused transcranial stimulation (Cohen et al., 1990; Deng et al., 2008; Ren et al., 1995; Roth et al., 2002; Ruohonen and Ilmoniemi, 1998). There is a general perception that the low conductivity of skull places a severe limit on spatial focality of electrical stimulation. The results of this modeling study support the further development of transcranial current stimulation technology for focal stimulation.

# Chapter 5: Bio-heat Transfer Model of Transcranial DC Stimulation: Comparison of Conventional Pad versus Ring Electrode

## 5.1 Introduction

Conventional transcranial direct current stimulation (tDCS) involves weak direct currents (1–2 mA) applied to the scalp via sponge-based rectangular pads (nominally 25-35 $cm^2$) for 10-20 min (Nitsche and Paulus, 2000, , 2001). tDCS is generally considered safe and comfortable (due to the low stimulation current intensities), however isolated reports on skin irritation/damage have suggested local scalp temperature increases as one probable cause (Lagopoulos and Degabriele, 2008; Palm et al., 2008). It is known that electrical stimulation of tissues may lead to temperature increases as a result of both joule heat and metabolic responses to stimulation (Elwassif et al., 2006). The aim of the present paper was to develop a bio-heat transfer model of tDCS and thereby investigate whether tDCS currents would lead to tissue temperature increases.

The spatial focality (targeting) of tDCS have been proposed to increase using a "ring" electrode configuration with electrodes < 11 mm in diameter: 4 X 1 ring (Datta et al., 2009a; Datta et al., 2008). The magnitude and spatial distribution of induced temperature changes for conventional big pad tDCS and the 4 X 1 ring (HD-tDCS) configurations are calculated and compared in this paper.

Brain function is especially sensitive to changes in temperature. An increase in temperature by ~ 1 °C can have profound effects on single neurons and neuronal network function (Elwassif et al., 2006). In addition, the local tissue temperature changes are typically affected by various factors, namely: 1) heat conduction to surrounding tissue; 2) advection (blood flow); 3) scalp heat loss to ambient due to convection, and 4) other thermoregulatory responses (sweating, pilo erection) (Nelson et al., 2000).

Experimental observations have indicated no temperature rise underneath the pads for conventional tDCS (Nitsche and Paulus, 2000). However, tDCS tissue temperature increases has not been previously determined in the scalp and the brain. A realistic MRI derived bio-heat transfer model can guide development of rational therapy and establishing safety standards. By solving the coupled Laplace equation of electrical field and the Pennes bio-heat transfer equation, we simulate how tDCS affects temperature field distribution in the tissue.

## 5.2 Methods

*A. MRI derived human head model:*

The volume conductor 3D model used in this study was developed previously by our group to calculate tDCS induced electric fields (Datta et al., 2009a). High resolution ($1mm^3$) raw 3T MRI scans were contrast enhanced and noise filtered. The head was segmented into compartments representing the brain tissue, cerebrospinal fluid, skull, muscle, fatty tissue, eyes, blood vessels and the scalp respectively. The solutions for the

coupled temperature and electric field for the whole head model at 1 $mm^3$ resolution would demand significant memory resources. The 3D model was thus resampled to 2 $mm^3$ which provided an optimal compromise between computation time and model size (accurate representation of tissues of interest). The stimulation rectangular pads, discs, gels were imported as CAD models (see below). The volumetric mesh was generated (minimum quality factor > 0.5) from the segmented data and eventually exported to COMSOL Multiphysics 3.5 (COMSOL Inc., MA, USA). The resulting mesh comprised >5,000,000 tetrahedral elements (>20,000,000 degrees of freedom).

The muscle, fatty tissue, eyes and blood vessel compartments were assigned the same tissue properties as that of scalp (Datta et al., 2009a). Tissue properties were assigned representative average values obtained from literature and are listed in Table 2. There is no blood flow to the CSF layer and metabolic heat is considered zero (Nelson et al., 2000; Nelson and Nunneley, 1998)

**TABLE 2**

TISSUE ELECTRICAL AND THERMAL PROPERTIES

| Tissue | Electrical Conductivity ($\sigma$) (S/m) | Thermal Conductivity ($\kappa$) (W/m.°C) | Blood flow Rate ($\omega_b$) (1/s) | Metabolic heat ($Q_{met}$) ( $W/m^3$) |
|---|---|---|---|---|
| Scalp | 0.465 | 0.39 | 0.00143 | 363 |
| Skull | 0.01 | 1.15 | 0.000143 | 70 |
| CSF | 1.65 | 0.61 | 0 | 0 |
| Brain | 0.2 | 0.57 | 0.08 | 10437 |

*B. Heat Transfer Model*

An approximate temperature distribution throughout a perfused tissue can be found by solving the bioheat transfer equation suggested by Pennes (Nelson and Nunneley, 1998):

$$\rho C \frac{\partial T}{\partial t} = \nabla(k \nabla T) - \rho_b \omega_b C_b (T - T_b) + Q_{met} \qquad (3)$$

where $\rho$: density; $C$: specific heat, $\kappa$: thermal conductivity; $\omega_b$: blood perfusion rate; $T$: temperature; $T_b$: arterial blood temperature; $Q_{met}$: metabolic heat.

During electrical stimulation, additional joule heating arises when energy is dissipated by an electric current flowing through a conductor. The Laplace equation $\nabla.(\sigma \nabla V) = 0$ (V: potential; σ : conductivity) was solved to determine the electrical potential. The bioheat equation (1) above is modified to incorporate joule heating during electrical stimulation (Elwassif et al., 2006):

$$\rho C \frac{\partial T}{\partial t} = \nabla(k \nabla T) - \rho_b \omega_b C_b (T - T_b) + Q_{met} + \sigma |\nabla V|^2 \qquad (4)$$

In this report, we considered steady state temperature increases consistent with prolonged tDCS protocols (>10 minutes) (Nitsche and Paulus, 2000, , 2001)

*C. Electrode Configurations*

We modeled two electrode configurations:

(1) 'Rectangular-pad' (Figure 7A): Two pads (7 X 5 $cm^2$) were placed at sites typically used for tDCS of the primary motor cortex (Datta et al., 2009a). Rectangular sponges are typically soaked in saline for conventional tDCS application and the abutting electrode is energized. The sponge was therefore assigned the electrical and thermal properties of saline ($\sigma$: 1.4 S/m; $\kappa$ = 0.3 W/m.°C).

(2) '4 X 1 ring' (Figure 7B): Four cathode disc electrodes were arranged in a circular fashion around an anode center electrode (Datta et al., 2009a) .The anode electrode is placed over the motor cortex (coinciding with the center of the anode pad used for rectangular-pad stimulation) and surrounded by four cathode electrodes (each at a disc center to disc center distance of 4 cm from the anode electrode). All disc electrodes had an 11 mm diameter. Current was conducted through disc electrodes into the scalp using a

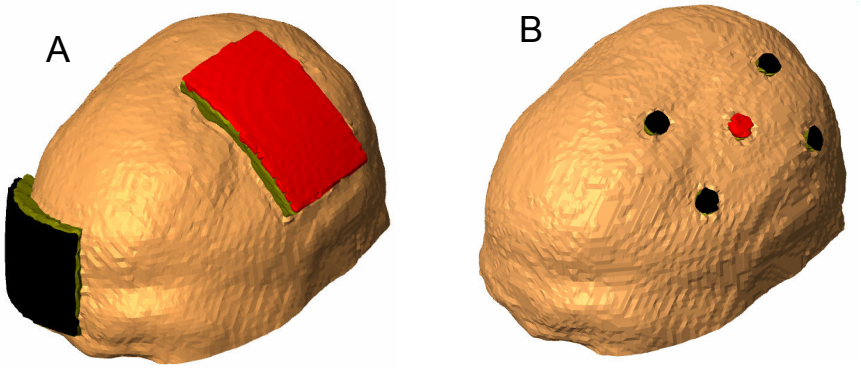


**Figure 7. Finite element model of conventional 7 X 5 $cm^2$ rectangular-pad and 4 X 1 ring configurations** (Red: Anode electrode, Black: cathode electrode; Olive Green: Sponge/Gel)

customized tDCS gel (CCNY-4) with electrical conductivity: 0.3 S/m and thermal conductivity: 0.6 W/m.ºC.

All electrodes were modeled as conductors with $\sigma$ = 5.8 x $10^7$ S/m and $\kappa$ = 31 W/m.°C.

*D. Initial and Boundary Conditions*

The electrical boundary conditions used were (1) inward current flow = $J_n$ (normal current density) applied to the exposed surface of the anode electrode, (2) ground applied to the exposed surface of the cathode electrode(s) and (3) all other external surfaces treated as insulated. Current densities corresponding to 1 mA total current for the rectangular pad configuration and 2 mA for the 4 X 1 ring configuration were respectively applied. 2 mA of current applied through the 4 X 1 ring configuration results in similar electric field magnitude peak directly *underneath* the pads for the conventional rectangular-pad stimulation (Datta et al., 2009a).

The heat loss at the scalp surface is due to both sweat evaporation and convection to ambient (Janssen et al., 2005; Nelson et al., 2000). Heat loss due to sweat evaporation was not considered in this study. For the thermal boundary conditions, all external boundaries of the head model were assigned the following heat flux:

$$q = h(T_{amb} - T) \qquad (3)$$

$T_{amb}$ : External temperature = 24 °C

$T$: Temperature

$h$: Heat transfer coefficient W/($m^2$.ºC) = 4

The following parameters were applied: $\rho_b$ = 1050 Kg/$m^3$; $c_b$ = 3600 J/(Kg.°C); $T_b$ = 309.85 ºC (Elwassif et al., 2006). The electrodes, sponge, gel were assigned the initial temperature of $T_{amb}$. All the tissue compartments were assigned the initial temperature ($T_0$) of 37 °C.

Estimates of steady state tissue temperatures were first obtained by evaluating the model under prescribed conditions with zero applied current density (no stimulation). The solution of the model with injected current density was then compared with the 'no stimulation' condition to evaluate *relative* tissue temperature increases. In addition for the 4 X 1 ring, we calculated tissue temperature increases for injected current density ($J_n$ = 142.9 A/$m^2$); corresponding to 13.58 mA total current. The aforementioned current density value has been reported to be the minimum electrode current density at which brain lesions are observed in a rat model (Liebetanz et al., 2009).

**5.3 Results**

For the 7 X 5 $cm^2$ rectangular-pad (1 mA) and the 4 X1 ring (2 mA and 13.58 mA) configuration models (Fig. 7A and 7B), we calculated the induced tissue temperature distribution due to stimulation (Fig. 8). Rectangular-pad stimulation results in no significant tissue temperature rise in scalp or brain.

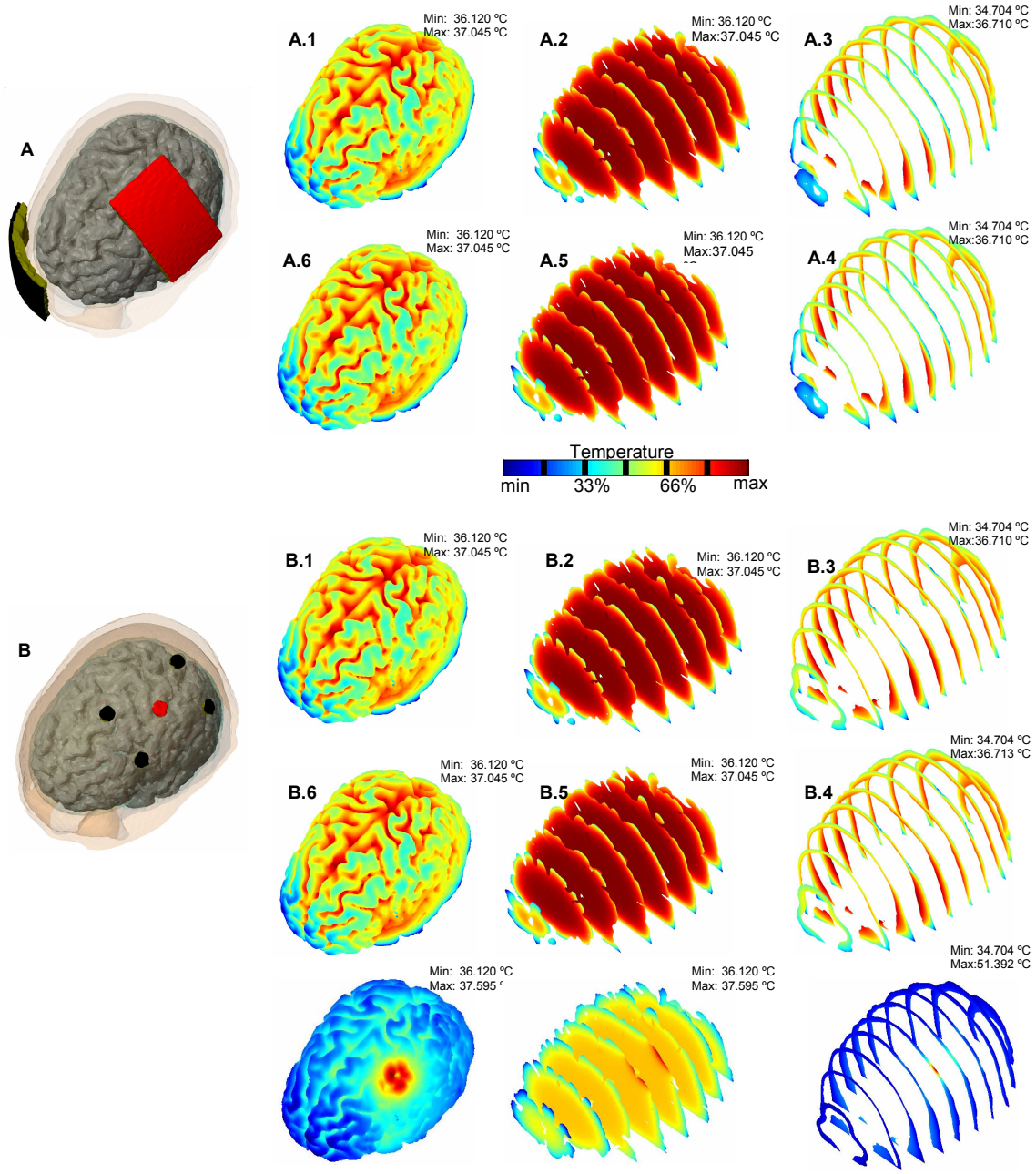


**Figure 8. Bio-heat transfer model of transcranial direct current stimulation using conventional rectangular-pad (A) and 4 X 1 ring electrode configuration (B).** For each configuration, we calculated the induced cortical temperature distribution due to stimulation. The first row of each of the two configurations (A.1 - A.3, B.1 - B.3) models the '*no-stimulation*' condition. The second row (A.4 - A.6) of the rectangular pad configuration models the 1 mA '*stimulation*' condition. The second and third rows (B.4 - B.6, B.7 - B.9) model the 2 mA and 13.58 mA '*stimulation*' conditions respectively. The first two columns plot the calculated induced cortical surface and cross- sectional temperature distributions. The last column plots the induced temperature distribution on a series of cross-sectional slices.

The 4 X 1 ring (1 mA) configuration does not lead to brain tissue temperature rise (Fig. 8B.4). Small tissue temperature rises are observed at the scalp (<0.01 °C). The 4 X 1 ring (13.58 mA) leads to a significant temperature rise of 6.41 °C at the scalp (Fig. 8B.9) and a nominal temperature rise of 0.55 °C at the brain (Fig. 8B.7).

**5.4 Discussion**

Our results indicate conventional tDCS protocols do not cause tissue temperature increases in the scalp. It should however be noted that magnitude of temperature increases critically depend on the electrical/ thermal properties and stimulation settings considered. Our results are consistent with studies where scalp temperature increases underneath the pads (Nitsche and Paulus, 2000) and HD electrodes (Minhas et al., 2010) were measured using a thermocouple.

The observed temperature increases in brain (which is a function of current flowing into the tissue) is electrode montage specific. This is indeed expected, given the particular electrode montage determines the magnitude and the spatial extent of current entering the brain (Bikson et al., 2008; Datta et al., 2008; Miranda et al., 2006; Wagner et al., 2004).

In the Liebetanz et al. sudy, electrode current density of 142.9 $A/m^2$ was found to be the threshold for rat brain lesions (presumably due to burning) using a montage that maximized current fraction entering the brain (Bikson et al., 2009a; Liebetanz et al.,

2009). However, using the same surface current density, we predict minimal brain temperature rises for the 4 X 1 ring; reflecting significant current shunting across the scalp. A potentially hazardous temperature rise was although predicted at the scalp. This highlights the importance of independently considering safety limits for scalp and brain, for each electrode montage (Bikson et al., 2009a; Datta et al., 2009a; Datta et al., 2008).

Our model does not consider micro architecture of the skin which potentially might play in a role in explaining cases of skin irritation observed in conventional tDCS. There have been studies where the skin has been considered to be composed of an outer unperfused layer ($\omega_b$=0), sweat glands, hair follicles, and a fat layer. An extension of this study would be to incorporate detailed architecture of the skin.

Additionally, in the present study we did not consider temperature induced changes due to variation in the electrical and thermal properties. A parametric study for evaluating temperature increases under all possible conditions is important and should be addressed in future.

The results of this present study provide an initial basis for determining tDCS induced temperature rises.

# Chapter 6: Transcranial direct current stimulation in patients with skull defects and skull plates

## 6.1 Introduction

Transcranial electrical stimulation using weak direct currents - transcranial direct current stimulation (tDCS) - is a powerful method of brain modulation that has been increasingly tested as a tool to modulate plasticity in neuropsychiatric diseases (Boggio et al., 2009c). Relatively simple to apply, tDCS involves application of direct current through at least one electrode positioned on the scalp. The mechanisms of tDCS are associated with the intensity and direction of current flow through the cortex, leading to neuromodulation and lasting changes in cortical excitability. Clinical tDCS has shown to induce beneficial effects in preliminary studies in different neuropsychiatric conditions such as pain (Fregni et al., 2006b; Fregni et al., 2007), motor rehabilitation (Fregni et al., 2005b; Hummel et al., 2005), cognitive function (Fregni et al., 2005a; Iyer et al., 2005), major depression (Boggio et al., 2007) and craving disorders (Boggio et al., 2009b).

Because of these initial positive results, tDCS has the potential to be used for the rehabilitation of patients with brain lesions who also have skull defect (with or without skull plates) such as patients with traumatic brain injury (TBI) or patients who undergo neurosurgery. In fact, some of the neurological sequelae are presumably consequences of disrupted cortical activity following the traumatic event, and tDCS in this circumstance can be a useful tool to reactivate and restore activity in essential neural networks associated with cognitive and motor processing. In our pilot study combining tDCS with

robotic motor training aimed at upper extremity motor recovery, in a small group of TBI survivors with no skull defects, we showed that tDCS can enhance the effects of upper extremity motor training. tDCS has similar potential to also improve cognition in these patients. Finally, because of the anti-seizure effects of tDCS (Fregni et al., 2006d; Liebetanz et al., 2006),this technique might be useful for patients with refractory epilepsy who underwent surgery and have skull plates or applied to patients who needed to undergo decompressive craniectomy for trauma and cerebrovascular disease.

Although evidence supports the investigation of tDCS in TBI or patients with other major neurological deficits and skull defects, one perceived limitation for the use of tDCS in these patients is the modified current flow by the skull defects and use of skull plates. During tDCS, current applied at the scalp must pass through the resistive skull before reaching the brain, and the specific relationship between electrode position, skull geometry, and the underlying tissue properties are thought to determine the location and magnitude of current flow (Datta et al., 2009a). It remains unknown how skull defects and use of skull plates associated with TBI would affect current flow through the brain and how to modify tDCS dose and/or electrode locations in such cases. For example, a hole through the skull that is filled with relatively highly conductive fluid or tissue, might present an attractive “shunt” pathway for current entering the brain. The underlying cortex would then be exposed to a higher intensity of focused current flow. This in turn might be either beneficial in targeting the underlining brain region or hazardous if the increased current levels resulted in undesired neurophysiologic or pathological changes.

Computational finite element method (FEM) models of tDCS allow prediction of current flow through the cortex (Miranda et al., 2006; Wagner et al., 2007). We previously developed a high-resolution MRI-derived model of tDCS with increased precision and accuracy (Datta et al., 2009a). Here we modify this model to include conceptualized (cylindrical) skull defects and plates and analyze resulting changes in cortical current flow; therefore our aims were to: (i) determine cortical current density distributions in subjects with skull defects; (ii) determine whether the size of skull defect influences the amount and location of current being delivered to brain cortex and (iii) determine whether skull plates (i.e. acrylic or titanium plates) also change (and in which direction) the amount of current being delivered to the brain. Our results provide a general framework to determine what factors modulate current flow to the brain in cases of specific skull injuries, and thus a rational basis for customizing electrical stimulation dose based on individual parameters and desired outcome.

## 6.2 Methods

*MRI guided finite element head model*

The volume conductor 3D model (having 1 $mm^3$ resolution) used in this study was developed previously by our group to calculate tDCS induced electric fields. The entire process involving segmentation of high resolution 3T MRI scans, mesh creation and the eventual export to a finite element method solver (SIMPLEWARE LTD., UK) was detailed previously (Datta et al., 2009a); importantly the entire work-flow preserves the high resolution of the MRI scans. The model is referred to as the 'healthy head model' in

this paper (Figure 9) and the electrical properties of the tissues are assigned representative isotropic average values (in S/m): brain: 0.2; CSF: 1.65; skull: 0.01; and scalp: 0.465. The muscle, fatty tissue, eyes and blood vessel compartments were assigned the same tissue properties as that of scalp. In this study, the tDCS induced cortical currents of a healthy head was used as a control to evaluate the effects of skull injury. In Part 1, we modeled two electrode *configurations* in combination with a range of skull *defects* and skull *plates*, as specified below. For each model, the combination of electrode configuration and skull injury type and location, together determine the model *montage*. For Part 2, we focused on the role of varying skull defect size under an electrode. Outside of the injury, head properties were unchanged across montages.

*Part 1: Electrode properties and configurations*

We modeled conventional "sponge-based" electrodes having dimension of 7 x 5 $cm^2$, which is a size commonly used in clinical studies and calculated the induced currents in the cortex resulting from application of 1 mA total current (corresponding to an average electrode surface current density of 0.28 $A/m^2$).

We modeled two electrode configurations (Figure 9):

(A) M1 - supraorbital : The anode electrode was placed over the primary motor cortex with its center localized 5 cm below the vertex (corresponding to C3) and the cathode electrode was placed over the contralateral supraorbital area.

(B) Occipital - supraorbital: The anode electrode was placed on O1 (primary occipital cortex) and the cathode electrode was placed over the contralateral supraorbital area.

The latter electrode configuration allowed us to model the presence of large skull defects and skull plates between the stimulation electrodes. During conventional tDCS, rectangular sponges are typically soaked in saline and the abutting electrode is energized. The sponge was thus assigned the electrical conductivity of saline ($\sigma$ = 1.4 S/m) and the stimulation electrodes were modeled as conductors ($\sigma = 5.8 \times 10^7$ S/m). The electrodes had a thickness of 1 mm and the thickness of the sponge varied from 1 - 2.5 mm. An important note here is that electrode location is important only in relation to skull defects and skull plates.

*Part 1: Skull Defects - Acute and Chronic Defects*

Skull defects were modeled as idealized cylindrical "holes" in the skull. We considered the following two defect sizes in this study: (1) a large hole having a diameter of 10 cm that can be associated with decompression craniectomy, surgery to hemorrhage drainage or large skull fracture (Rish et al., 1979) and (2) a small hole with a diameter of 2.5 cm that is usually found as a consequence of a neurosurgical procedure or a small skull fracture (Sekhar and Fessler, 2006). Distinct locations of the holes - either under or between the stimulation electrodes were modeled. In cases where the hole in the skull was underneath the stimulation electrode, the center of the injury was aligned with the center of the electrode (for instance, over the primary motor cortex, corresponding to the

location of C3). In cases where the holes were between the stimulation electrodes, the center of the injury corresponded to approximately midway between the anode and cathode electrodes.

We analyzed two different scenarios for tissue filling up defects: in the *acute* defect state, CSF ($\sigma$ = 1.65 S/m) was used to fill the hole in the skull whereas in the *chronic* defect state, the hole was replaced by a scar tissue having a combined electrical conductivity of subcutaneous tissue, blood, and meninges compartments ($\sigma$ = 0.34 S/m ).

*Part 1: Skull Plates - Titanium and Acrylic*

In most of the cases where there is a large skull defect and where the original skull cannot be used to cover the defect, a skull plate is usually indicated for cosmetic purposes and to also protect against external trauma. Therefore another objective in our study was to determine how the presence of skull plates would interfere with the tDCS induced cortical currents. We modeled two material types of skull plates: one made by titanium (one of the most common plates used) with a conductivity of $7.40 \times 10^{5}$ S/m, and acrylic (less common, but a less expensive solution) having a conductivity of $0.20 \times 10^{-12}$ S/m. We evaluated skull plate only for large skull injuries (10 cm diameter) as usually small skull injuries are not covered with plates. As with acute and chronic skull defects, the skull plates were modeled by replacing a cylindrical hole in the skull by a material; in this case with either titanium or acrylic (Figure 9).

*Part 1: Electrode Montages*

The specific electrode montages implemented for Part 1 are listed in Table 3. For each montage (1-6), the induced cortical currents were analyzed and compared with the analogous healthy head model (Figure 9).

*Part 2: Skull Defect size*

To consider the role of incremental changes in skull defect size, the M1-supraorbital electrode configuration was modeled with different sized skull defects (0.5 cm, 1.5 cm, 3.5 cm, 4.5 cm, 6 cm, and 8 cm diameter). The *acute* state (defect filled with CSF) was considered in all cases – as this state represents the worst scenario in terms of safety - and the skull defects were modeled to be directly underneath the stimulation electrode pads. Note that we did not model skull defects between electrode pads, as induced cortical peak electric field values do not differ significantly from the healthy case. For the M1-supraorbital configuration, we considered both a 7 x 5 $cm^2$ and a 3.5 x 3.5 $cm^2$ *anode* pad – the cathode remained 7 x 5 $cm^2$ in all cases. Note that for Part 2, montage designations were not used.

*Field solver*

A quasi-stationary condition was assumed for the volume conduction in our model. The electric field in a volume conductor is represented as $\nabla.(\sigma\nabla V)=0$ (V: scalar electric potential; $\nabla$ : gradient vector; $\sigma$ : conductivity). The resulting Laplace equation assuming uniform local conductivity was eventually solved to determine the induced cortical electric field distributions. The boundary conditions used were as follows : (1)

inward current flow = $J_n$ (normal current density) applied to the exposed surface of the anode electrode, (2) ground applied to the exposed surface of the cathode electrode, and (3) all other external surfaces treated as insulated. Current densities corresponding to 1 mA total current were applied for each montage. We used COMSOL Multiphysics 3.5 (Comsol Inc., MA), a commercially available finite element (FE) package to implement the model. The linear system iterative solver of conjugate gradients was used with a relative tolerance of $1 \text{ X } 10^{-6}$.

Surface-magnitude plots were generated by plotting the magnitude of electric field (EF) on the surface of brain tissue. Because the conductivity of brain is uniform, these same plots also represent induced current density profiles ($J = \sigma .E$). Additionally, the surface area (in $mm^2$) of the cortex, where electric field magnitude was greater than 90%, 80% and 50% of the *peak* electric field magnitude was calculated for each montage. These percent *area* measures allow a comparison of the relative focality of induced cortical current flow across different montages (irrespective of peak electric field)- however, it is important to qualify the concept of "focality" when using large sponge electrodes in the context of dispersed clustering of current hot spots throughout the brain (Datta et al., 2009a). The presence of eye balls and fatty tissue owing to their high conductivity provide preferential current pathways that may lead to regions of increased EF magnitude at the bottom of the cortex. In this study, these regions were excluded from the analysis and the peak values reported are from the top surface of the cortex.

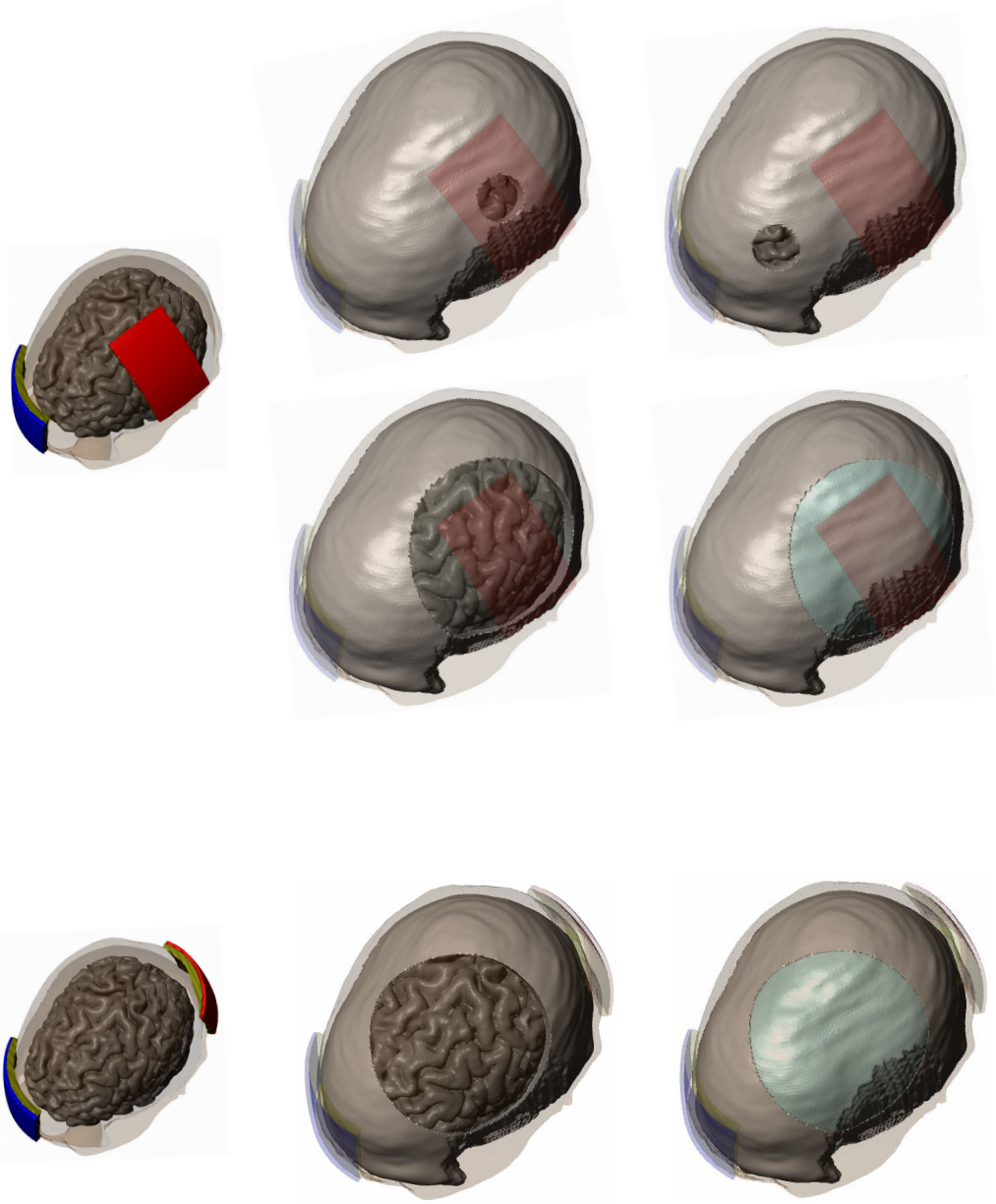

**Figure 9. Healthy and skull injury (defect/plate) simulation montages used to evaluate effects on cortical current flow.** *Part 1*. Two electrode configurations were evaluated (Anode:Red, Cathode:Blue and Sponge: Olive green). We evaluated the impact of acute or chronic defects (empty skull holes) and skull plates (metallic holes). For the motor-cortex anode electrode configuration, the effect of a small defect under or between the electrodes was evaluated (Top Row). For motor-cortex anode electrode configuration, the effect of large defect or plate under the electrodes was also tested (Middle Row). For occipital anode tDCS, the effect of large defect or plate between the electrodes was tested (Bottom Row).

## 6.3 Results

We modeled the current distribution in the head during tDCS using two conventional electrode configurations with a range of idealized skull defects or skull plates. We considered the EF magnitude distribution along the cortical surface under the general assumption that both neuromodulation and risk of pathology increase monotonically with EF magnitude (see Discussion). For Part 1, the effects of skull injuries on the location and magnitude of peak cortical EF, as well as the EF distribution was analyzed (Table 3). For Part 2, the variation of induced cortical electric fields with skull defect size was determined. Evidently it is not possible to explicitly consider all permutations of electrode configuration and defect/plate montages, nor can our results using a specific head anatomy be arbitrarily and quantitatively generalized (see Discussion in this chapter); rather the goal of this analysis is to identify what factors modulate current flow through the brain and develop a general framework for identifying how these factors interact. Ultimately, such knowledge would provide a basis for designing tDCS electrotherapies in patients with TBI or surgical skull defects.

*Healthy Skull Montage*

In order to explore the effects of skull injuries on cortical currents, it is necessary to compare with a healthy head model in which the skull is intact. We therefore adapted a high-resolution (sulci/gyri precise) healthy model developed previously. Consistent with our previous predictions, using either M1 and Occipital anode “large sponge” electrode

configurations resulted in diffuse modulation over the entire cortical surface with numerous discrete clusters of local EF maxima (in contrast with the controlled focality of High-Definition tDCS; Datta et al., 2009a; Datta et al., 2009b). The observance of these localized clusters/hot-spots reinforces the importance of incorporating detailed cortical geometry in any tDCS modeling study.

A total current of 1 mA injected through the electrodes resulted in a 0.67 V/m and 0.77 V/m peak cortical EF magnitudes for the M1 and Occipital anode configurations, respectively. These values are compatible to predictions from previous tDCS FEM models (Miranda et al., 2006; Wagner et al., 2007).

Using large sponge configurations, any consideration of focality and targeting must be qualified. M1 anode electrode configuration resulted in more than 9000 $mm^2$ of cortex being at or above 50% of the peak cortical EF; moreover the peak EF was between and not under the sponges (Figure 10, top row). Using the Occipital anode electrode configuration, more than 8500 $mm^2$ of cortex was at or above 50% of peak cortical EF, with the peak clustered under the lateral edge of one pad (Figure 12, top row).

*Part 1: Small skull defect (fig. 2 – montages 1 and 2)*

The presence of a small defect (diameter = 2.5 cm) in the skull directly underneath the pad (Montage 1) creates a preferential conduit for radial currents into the cortex; thus, altering the spatial profile of current flow as compared to the healthy model (Figure 10). Specifically, this montage results in a 'focal' region of modulation with

increased induced EF/current density magnitude that has roughly the dimensions of the overlying skull hole.

The observed peak EF magnitude in the cortex is strongly influenced by the conductivity value of the material filling the skull defect. The acute phase (defect filled with CSF) and chronic phase (defect filled with scar tissue) resulted in peak EF magnitude of 2.50 and 1.67 V/m respectively. Thus in Montage 1, for the acute phase, the induced EF magnitude increases to ~3.7 times than that for a healthy head model (Part 2 below addresses the specific role of defect size in more detail).

In all cortical field plots, the false-color map is scaled to the respective peak cortical EF. Only for the case of Montage 1B, where we also re-scaled the color map to correspond to the peak value observed for Montage 1A (Figure 10, box); it becomes apparent that Montage 1B results in reduced cortical activation under the defect compared to Montage 1A. This was done to emphasize the importance of *not* directly comparing false-color plots across montages without correcting for the different scales used.

In contrast, when the small skull defect location is *between* the two electrode pads (Montage 2), there was not a marked change in the spatial profile of current flow through the cortex (Figure 10). In fact, similar peak EF magnitude as that of the healthy model is observed in both the acute and chronic states. This finding highlights that the *specific location* of the defect critically influences the flow of cortical currents. In addition, in

| Electrode configuration | Montage | Skull defect/plate | Location of defect | Phase/plate material | Peak (V/m) | $Area_{90}$ | $Area_{80}$ | $Area_{50}$ |
|---|---|---|---|---|---|---|---|---|
| C3-supraorbital | Healthy (*motor cortex tDCS*) | None | – | – | 0.67 | 261.60 | 720.28 | 9390.44 |
| | 1A | Small hole | Under pad | Acute | 2.50 | 2.75 | 8.51 | 220.66 |
| | 1B | Small hole | Under pad | Chronic | 1.67 | 7.80 | 24.74 | 710.32 |
| | 2A | Small hole | Between pads | Acute | 0.67 | 255.62 | 672.69 | 7600.87 |
| | 2B | Small hole | Between pads | Chronic | 0.67 | 263.22 | 693.00 | 7949.73 |
| | 3A | Large hole | Under pad | Acute | 0.79 | 190.90 | 570.56 | 7208.39 |
| | 3B | Large hole | Under pad | Chronic | 0.79 | 239.65 | 712.46 | 9287.59 |
| | 4A | Large plate | Under pad | Titanium | 0.90 | 88.70 | 316.46 | 4324.06 |
| | 4B | Large plate | Under pad | Acrylic | 0.62 | 254.09 | 691.22 | 7654.99 |
| O1-supraorbital | Healthy (*visual cortex tDCS*) | None | – | – | 0.77 | 186.75 | 585.39 | 8519.38 |
| | 5A | Large hole | Between pads | Acute | 0.72 | 197.79 | 583.87 | 8000.84 |
| | 5B | Large hole | Between pads | Chronic | 0.73 | 235.95 | 723.74 | 9907.25 |
| | 6A | Large plate | Between pads | Titanium | 0.91 | 17.26 | 96.03 | 2857.60 |
| | 6B | Large plate | Between pads | Acrylic | 0.77 | 184.33 | 585.08 | 8612.48 |

**Table 3. Summary of evaluated model montages and simulation results** for *Part 1*. The first column reports the electrode configuration and the second column lists the various montages modeled. The third and the fourth column specify the type and the location of the defect respectively. For each of these montages, the skull deficit was modeled by replacing the damaged tissue. The deficit was replaced by CSF in the 'acute' phase and by scar tissue in the 'chronic' phase. Column five lists either the phase of the deficit or the type of material used for the deficit as applicable. The peak induced electric field magnitude (in V/m) for each of the montages is listed in Column 6. Columns 7-9 report the area (in $mm^2$) of the cortex where the induced EF magnitude was greater than 90%, 80% and 50% of the observed peak EF magnitude respectively.

contrast to the observation with large holes (see below), the defects are not large enough to act as a significant preferential shunt for current to cross into the underlying cortical surface.

**Figure 10. Brain modulation of *small skull defects* during tDCS.** Each of the rows show the surface magnitude plots of induced electric field magnitude (with different views). The second column shows the *top view*, while the third column shows the *side view* revealing modulation in the posterior lobes. The first row models the C3-supraorbital montage (Healthy Model) thereby enabling comparison with the head models having skull defects. The second and third rows show the modeling results for Montage 1 with acute and chronic states respectively (see Methods). Likewise, the fourth and the fifth rows plot the simulation results for Montage 2.

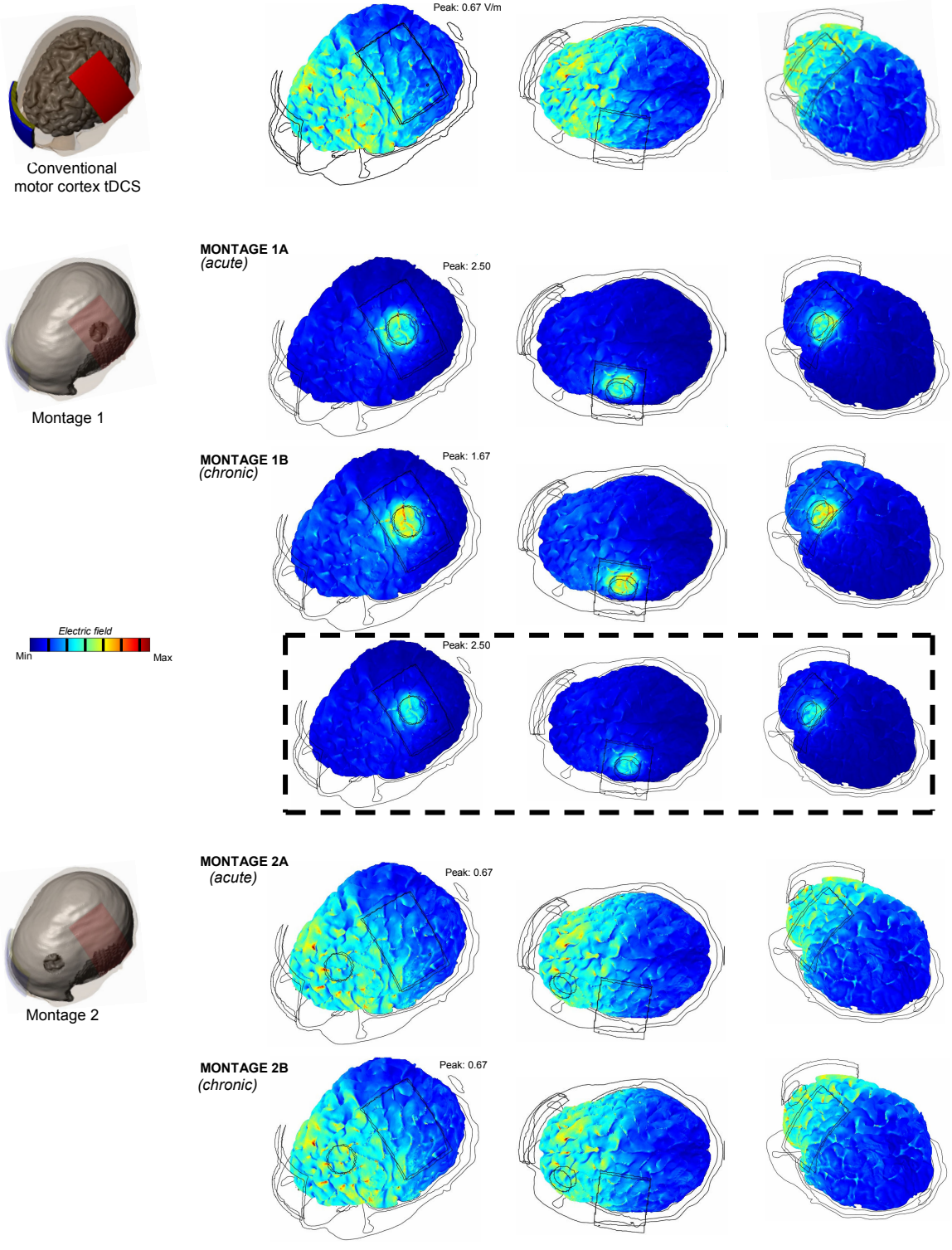
Peak: 0.67 V/m
Conventional
motor cortex tDCS
MONTAGE 1A
(acute)
Peak: 2.50
Montage 1
MONTAGE 1B
(chronic)
Peak: 1.67
Electric field
Min
Max
Peak: 2.50
MONTAGE 2A
(acute)
Peak: 0.67
Montage 2
MONTAGE 2B
(chronic)
Peak: 0.67

*Part 1: Large skull defects (figures 11 and12 – montages 3 and 5)*

The presence of a large defect (diameter = 10 cm) in the skull directly underneath the pad (Montage 3) alters the spatial profile as compared with the healthy head model. The peak induced EF magnitude was 0.79 V/m in both the acute and chronic phases (Figure 11). However, in spite of similar peak EF magnitudes, the region of cortical modulation is influenced by the conductivity value of the defect. Peak EF magnitude was observed in the cortex directly underneath the hole in the chronic case while for the acute phase, the peak EF magnitude was observed in cortex corresponding to the edge of the hole.

For the case where the defect was between the two electrodes (Montage 5), current is initially induced in the posterior lobes and then is shunted across the hole (Figure 12). The amount of shunt depends on the electrical conductivity of the hole. The peak induced EF magnitude in the acute and chronic cases was similar to that of the healthy head model.

The primary effect of large skull defects (with increasing conductivity relative to the skull) can be broadly described as *reducing* current flow crossing into the underlying cortex by shunting (transverse to the cortical surface) while concentrating current in the cortex underlining the skull defect edge. The aforementioned effect is however observed to be more pronounced with proximity of the defect to the stimulation pad.

*Part 1: Skull plates* (*figures11 and 12 – montages 4 and 6)*

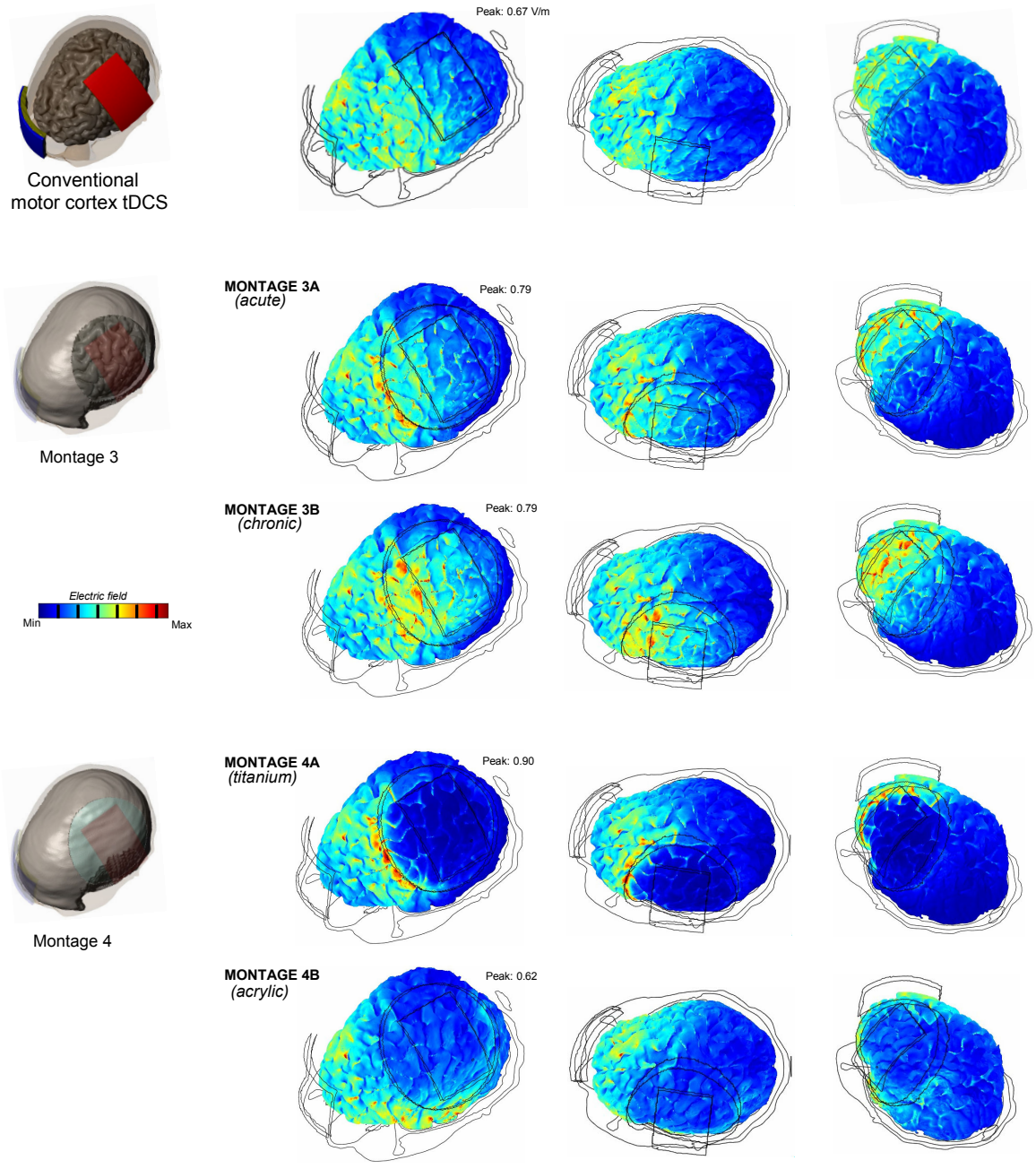


**Figure 11. Brain modulation of *large skull defects and skull plates* during motor cortex tDCS.** Each of the rows show the surface magnitude plots of induced electric field magnitude (with different views). The second column shows the *top view*, while the third column shows the *side view* revealing modulation in the posterior lobes. The first row models the C3-supraorbital montage (Healthy Model). The second and third rows show the modeling results for Montage 3 with *acute* and *chronic* states respectively (see Methods). The fourth and the fifth rows plot the simulation results for Montage 4 with *titanium* and *acrylic* skull plates respectively.

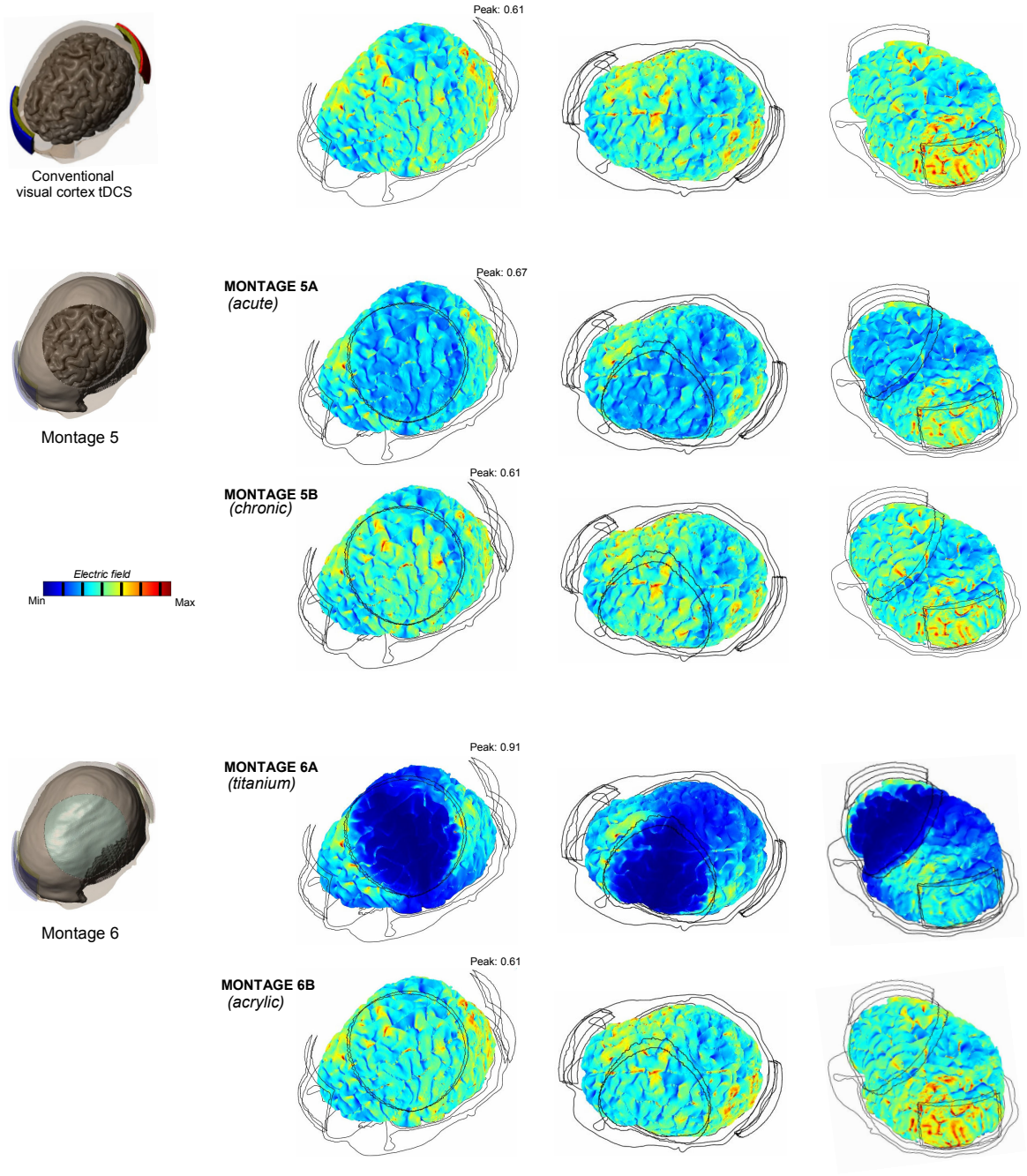


**Figure 12. Brain modulation of *large skull defects and skull plates* during visual cortex tDCS.** Each of the rows show the surface magnitude plots of induced electric field magnitude (with different views). The second column shows the *top view*, while the third column shows the *side view* revealing modulation in the posterior lobes. The first row models the O1-supraorbital montage (Healthy Model). The second and third rows show the modeling results for Montage 5 with *acute* and *chronic* states respectively (see Methods). The fourth and the fifth rows plot the simulation results for Montage 6 with *titanium* and *acrylic* skull plates respectively.

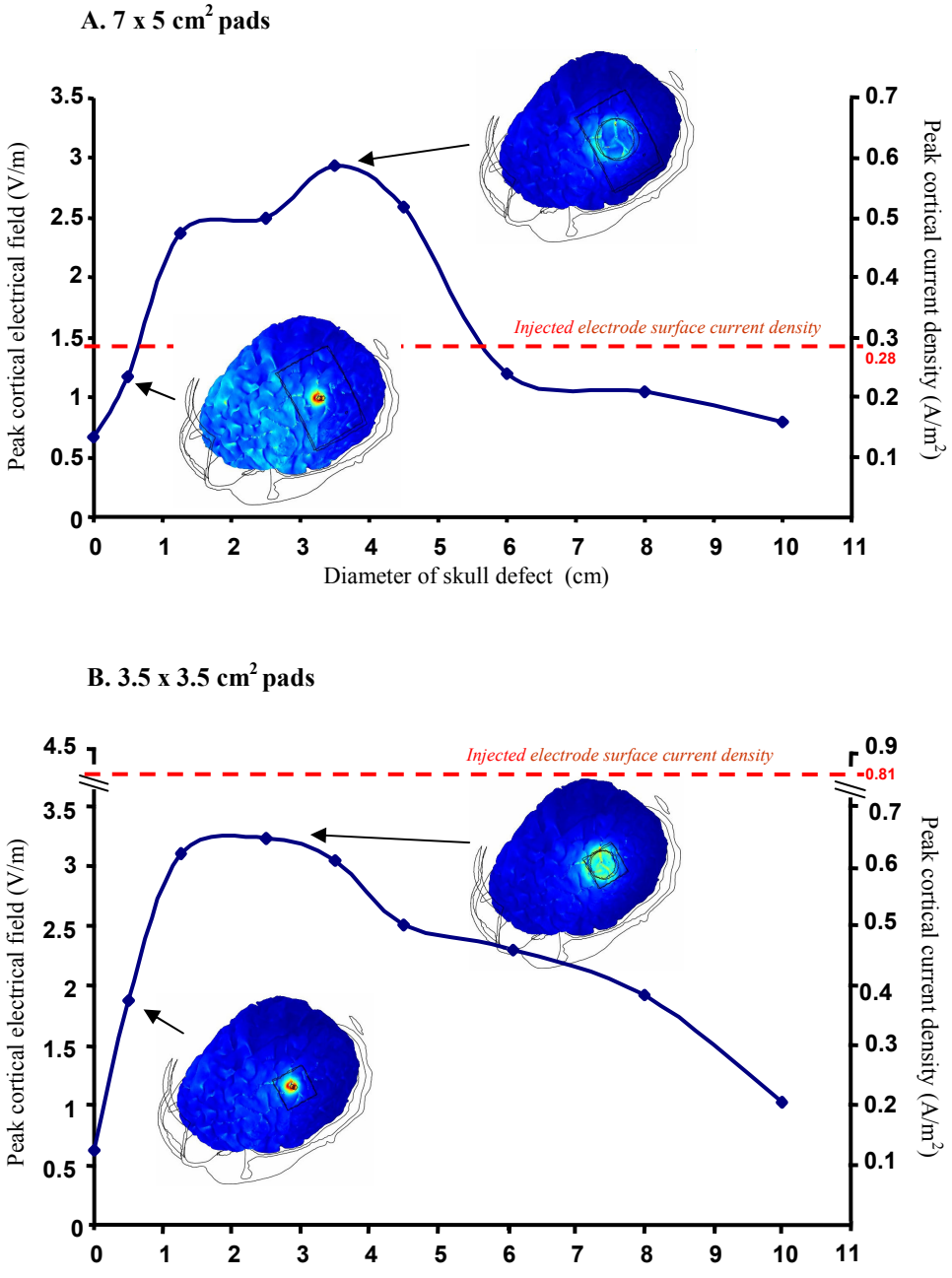


**Figure 13. Role of skull defect size in shaping brain modulation during tDCS.** In *Part 2*, acute defects were fixed under the motor cortex anode. Two anode electrodes sizes were evaluated: A) 7 x 5 cm and B) 3.5 x 3.5 cm with a range of acute skull defect diameters and for the healthy case (e.g. 0 diameters skull defect) case. Peak cortical electric field and peak cortical current density (which are linearly related) are graphed with selected cases expanded as cortical surface plots (scaled to the respective peak cortical electric field). For both electrodes, 1 mA of current was applied resulting in average electrode current densities of (0.28 and 0.81 A/m$^2$ respectively corresponding to the dashed red lines).

Due to its very high conductivity, the presence of a titanium plate accentuates the shunting effect observed with large skull defects. The region of modulation is generally restricted to the portion of the cortex corresponding to the edge of the defect and negligible modulation is observed directly underneath the plate. In addition, the rises in the peak induced EF magnitude (for both under and between the pads) in comparison to the healthy head model are more than that observed with large skull defects.

The effects of acrylic plates on the underlying cortical flow are much less pronounced. There is a negligible difference in both the overall spatial profile and the peak induced EF magnitude in comparison with the healthy model (Montage 6B). For the case of acrylic plate under the pads (Montage 4B), there is a nominal decrease in the peak EF magnitude in comparison to the healthy model.

*Part 2: Skull Defect size*

The values of induced cortical EF magnitudes are maximal when the skull defect size approximates the dimension of the stimulation pad and then decreases when skull defect size is either very small or large (Figure 13). A similar trend was observed with both the 7 x 5 $cm^2$ and 3.5 x 3.5 $cm^2$ stimulation pads. However, for the 7 x 5 $cm^2$ case, the observed peak induced current density in the brain, for a skull defect range of ~3.5 cm, was found to *exceed* the average injected scalp electrode current density (total injected current / electrode area).

Under both the 7 x 5 $cm^2$ and 3.5 x 3.5 $cm^2$ pads, the presence of very small defects (0.5 cm diameter) doesn't increase the peak induced electric field significantly relative to the healthy head model. As the skull defect size becomes smaller, less current shunts through the defect into the underlying cortex eventually approximating the spatial profile observed in the healthy (no defect) case (see Figure 13).

**6.4 Discussion**

Our results confirm the notion that skull defects and skull plates can change the distribution of the current flow induced in cortical areas by tDCS; however, the details of current modulation depend entirely on the combination of electrode configuration and nature of the defect/plate. In majority of cases, with the notable exemption of a moderate defect directly under an electrode, the presence of defects does not result in a marked increase in peak cortical electric field magnitude, though the distribution of electric field and the location of the peaks are shifted toward defect edges.

*Altered current flow around skull defects and plates*

We propose a relatively parsimonious framework to explain the range of observation in this study. Under healthy conditions, we previously showed that current is first "diffused" laterally at the skin and then crosses the skull in a largely radial manner; the current is *not* diffused through the skull (as previously contended). After passing the skull the current travels through the higher-conductivity CSF network, where is can be both diffused and concentrated; and before crossing into the brain, current patterns may be dominated by CSF which offers a pathway with much smaller resistance. For the case

of a small to moderate size defect with increased conductivity relative to skull, the defect acts as preferential pathway for current to cross radially (compared to the surrounding skull) and into the brain leading to a "funnel" type phenomena (Datta et al., 2009a). The maximal concentration of cortical current is a function of several factors including defect size relative to electrode size. Importantly, the conditions at the surface (skin) still determine if there is a driving force for current to enter or exit at the location of the defect, so for the case of a small defect in the middle of two electrodes there is not enough driving force and no significant current flow at that location under normal conditions – as such, the defect does not change the over-all current flow pattern.

For the case of a large defect/plate, with conductivity significantly higher than skull, current may now travel tangentially along the defect/plate, moving between the electrodes. This new defect/plate pathway may be comparable in conductivity to that of the underlying tissue (e.g. chronic defect) or the new pathway may be more conductive than the underlying tissue (e.g. acute defect and especially the titanium plate). The fraction of current "diverted" through the defect increases with both defect conductivity and defect proximity to an electrode. In the extreme conductivity case of titanium, the current preferentially travels tangentially along the plate, avoiding underlying tissue, until reaching the defect/plate edge at which point the current enters the tissue radially rather than continue in the highly-resistive skull.

Similar considerations can explain the range of EF distribution observed under conditions of defects and plates (Figure 10, 11, 12, 13), though we emphasize that the

ultimate pathway of current flow through the brain is rather complex and determined by the combination of all tissue geometries and properties. None-the-less, our results indicate that a gross consideration of the idealized defect/plate properties relative to the electrode configuration can be used to intuitively predict the qualitative alterations of current flow.

*Clinical and safety considerations*

Because tDCS has been increasingly studied for the treatment of neuropsychiatric disorders such as depression, stroke and chronic pain, an important question explored in this study is, the effect of skull defects and skull plates on the induced current by tDCS. This is an important issue since a relatively large proportion of patients might have skull defects and skull plates such as patients with stroke, who underwent decompression craniectomy, or patients with refractory epilepsy who undergo epilepsy surgery and finally patients with traumatic brain injury that commonly have skull fractures or need to undergo craniectomy. To date, there are no studies assessing the effects of tDCS in these patients. The only investigation using another technique of noninvasive brain stimulation involved the use of transcranial magnetic stimulation (TMS) in patients with refractory epilepsy and titanium plates. In these two studies, authors assessed temperature and side effects and showed minimal or no effects on these parameters after repetitive TMS (Rotenberg et al., 2007; Rotenberg and Pascual-Leone, 2009). It would be important to repeat such experimental evaluations for the case of tDCS. The biophysics surrounding how defects and plates modulate current flow for the cases of tDCS and TMS are distinct, and one cannot directly extrapolate (altered) efficacy or safety guidelines.

The central clinical relevance of this study is that skull injuries significantly change the distribution of the current being induced in cortical areas. As highlighted in this work, our models predict that current may become concentrated over the edges of large skull defects/plates. Interestingly, similar edge effect is seen in another study where tDCS fields were computed for stroke lesions filled with CSF (Wagner et al., 2007). Importantly, for the range of *large* skull defect/plate configurations tested in the present study, no significant (1.5 times the peak cortical electric field) resulted, despite changes in distribution. This result suggests that although theoretically safe, stimulation with large skull defects might not induce the aimed clinical effects if different areas are stimulated. In fact, although tDCS induces relatively diffuse effects, position of electrodes and induced current is critical. In this case, the next important question is whether is possible then to vary electrode's position to induce currents in areas that were affected by the skull defect.

Another important finding of this study is that the current peak does not change significantly, except for moderately sized defects when the stimulation electrode is placed directly over the defect (Figure 13). This increase in current peak magnitude in comparison with the control (healthy) case may therefore pose potential safety concerns. However, a recent investigation in animals has shown that the current parameters of stimulation for tDCS are at least two orders of magnitude smaller than currents that would cause brain lesion (Liebetanz et al., 2009). If the degree of concentration due to the skull defect can be predicted, a simple mitigating measure would be to decrease the total injected current. Conversely, if the desired targeted brain region was under the skull

defect, positioning an electrode over a small defect could be used to focus current into the targeted region. Generally as defect size decreases, cortical modulation becomes concentrated under the defect and peak induced cortical electric fields increases. However, further decreases in defect size can decrease peak cortical electric field even as the relative profile of brain modulation continues to become more targeted. Still further decreases in defect size result in a shift toward diffuse brain activation, comparable to the healthy (no defect) case.

There has been debate about the relative merits of "normalizing" tDCS dose to average current density at the electrode surface (Miranda et al., 2009; Nitsche et al., 2007). Our results with skull defects support a tDCS dose system based on a consideration of the entire detailed electrode configuration (Bikson et al., 2008); moreover, individual differences and especially skull defects/plates will modulate how given electrode montages effect brain function. In this context it is important to consider that skull deficits will significantly vary across patients especially if associated with skull loss due to TBI and skull fracture; in each case the factors of defect size and position in relation to the electrodes can be generally considered according to the results of our study.

*Uses and Limitations of the present FEM study*

Our study has some limitations that need to be entertained in the context of progressing with clinical trials: 1) We considered only cortical surface electric field magnitude in this study under the assumptions that the cortical surface is of primary

interest in tDCS efficacy/safety and that both the degree of neuronal modulation and the risk of injury increase monotonically with electric field magnitude. This approach does not address the nature or specific thresholds for any physiological or pathological effects, the importance of neuronal geometry relative to applied fields (Datta et al., 2008) or the complex dynamic response of the brain to stimulation (Bikson et al., 2004); 2) As with any model, the accuracy of our predictions are limited by the accuracy and precision of the model (Datta et al., 2009a; Datta et al., 2009b); 3) Similarly, the role of baseline individual differences (e.g. gross anatomy) was not considered; 4) Moreover, the nature of defects is expected to vary significantly across cases and may be paramount in determining the details of current flow; 4) The defects considered here were highly idealized, since one would expect complex geometries and in-homogeneous tissue properties (including tissue encapsulation) in realistic injuries.; 5) Finally an important issue is that skull defects and skull plates are usually seen in patients with cortical damage and because we modeled only one healthy adult male brain, it is conceivable that cortical lesions would cause additional disturbances in the current being induced by tDCS. Such changes could affect current flow within the damaged region and through adjacent regions in a complex manner. For all the reasons indicated, *individualized* models for patients with brain and skull lesions is the best approach to predict with some accuracy maximal currents and current distributions. Despite these significant limitations in extrapolating *quantitative* generalization from the present study, the qualitative characterization of the general combination of factors which lead to altered current flow in cases of skull defects/plates provide a basis to understand how skull defects would affect current intensity and distribution and therefore can be helpful to set out inclusion

and exclusion criteria of patients with skull defects participating in tDCS trials for instance. This modeling study is therefore a critical step before testing patients with skull defects with tDCS. The next step is to perform functional assessments (such as testing cortical excitability changes) to confirm these results.

# Chapter 7: Role of "return" electrode's position and size in design of electrode montage for tDCS

## 7.1 Introduction

(Moliadze et al., 2010) investigated the role of electrode montage in the induction of acute lasting excitability changes by transcranial Direction Current Stimulation (tDCS) and transcranial Random Noise Stimulation (tRNS); specifically the study demonstrated that during weak transcranial electrical stimulation, the position of the "return" electrode affects neuromodulation under the "active" electrode. Despite wide-spread subsequent dissemination of tDCS, there remain significant unknowns about the mechanisms of tDCS and the design of electrode montages, including electrode size and placement. Moliadze and colleagues address the role of "return" electrode's position (and distance) via induction of Transcranial Magnetic Stimulation (TMS) evoked excitability changes under an "active" electrode over motor cortex (Moliadze et al., 2010).

Understanding and controlling electrotherapy dose is evidently critical in determining behavioral and clinical outcome. The position of stimulating electrodes governs current flow through the body, and hence the distribution of induced electric fields in the brain. These induced cortical currents/electric fields modulate neuronal excitability for DC stimulation and, in turn, determine behavioral and clinical outcomes (Bikson et al., 2008; Bikson et al., 2009b).

The most simplistic dose design schemes for tDCS assume a region of "increased excitability" in the cortex directly under the anode electrode, and a region of "decreased excitability' under the cathode, with intermediary regions largely spared (unaffected). Several studies have suggested limitations in this simplified approach including the need to consider: 1) Current density at the electrode (Nitsche et al., 2007; Miranda et al., 2006; Miranda et al., 2009); 2) Individual differences (Madhavan et al., 2010); 3) Significant current flow in intermediary regions, including the potential for current clustering (Datta et al, 2009); 4) Montages for unidirectional modulation (Rossini et al., 1985; Saypol et al.,1991; Datta et al., 2008); and 5) Relative electrode position, including inter-electrode distance (Stecker et al.,2005; Datta et al., 2008) and the use of extra-cephalic electrodes (Accornero et al., 2007; Ferrucci et al., 2008, Baker et al., 2010). Generally, increasing electrode separation on the head is expected to increase cortical modulation by increased relative amount of current entering the brain rather than "shunted" across the scalp.

The report by Moliadze and colleagues provides some of the strongest clinical evidence to-date that the relative position of stimulation electrode can affect neuromodulation under each electrode – namely that in determining electrotherapy dose the two stimulating electrodes *cannot* be considered separately and independently, even for relatively distant electrode positions. Moreover, increasing electrode distance may *decrease* the magnitude of neuro-modulation, depending on the specific montage and physiological measure.

The current flow through the body is strongly influenced by anatomical details, because of the different electrical conductivities of tissues such as scalp, skull/vertebrae, muscle, CSF, and brain – as a result the induced current profile in the brain may be detailed and complex. Given this, it is thus not surprising that the position of *both* electrodes determines the resulting current flow distribution through the cortex. Simultaneously, the complexity of current flow indicates that determining electrode montages dose by simplified assumptions may not be prudent, as highlighted by the results of Moliadze et al., 2010.

One solution to addressing this complexity in the design of rational stimulation protocols is the prediction of current flow patterns through the brain using computer models. The sophistication of computer models using finite-element-methods (FEM) for this purpose (Butson et al., 2007; De Lucia et al., 2007) has increased to allow high-resolution (e.g. 1 mm; Datta et al., 2009) and individualized modeling (Datta et al., 2010). Figure 14 illustrates the resulting brain current flow for three electrode montages – in all cases, the size and position of the "active" electrode over motor cortex is fixed, while the position or size of the "return" electrode is varied. The position and size of the "return" electrode affects the electric field distribution across the entire cortex. In addition, changing the position of the "return" electrode affects the electric field distribution in cortex directly under the "active" electrode.

## 7.2 Methods

An individualized FEM head model was created from MRI scans of an adult male at 1 mm x 1mm x 1 mm resolution (Soterix LLC, Brooklyn, NY). The head was segmented into compartments representing the brain, CSF, skull, scalp, muscle, eyes, and air. The Laplace equation was solved and current densities corresponding to 1 mA total current was applied. Induced cortical electric field (EF) magnitude maps for the different electrode montages were determined.

## 7.3 Results

Stimulation with a 4 cm x 4 cm return electrode over the contralateral forehead (Montage A) resulted in significant cortical activation in the right frontal lobe, as well as diffuse and clustered activation between the electrodes. Montage B (with 4 cm x 4 cm return electrode over contralateral mastoid) resulted in cortical electric field on the left hemisphere as current preferentially flows down the posterior regions of the brain and through the brain stem. Montage C (with 16 cm x 4 cm return electrode over contralateral forehead) resulted in diffuse and clustered cortical electric fields. For montages with different placements of return electrode (Montage A and B), the pattern of cortical electric fields directly *under* the "active' electrode (inset) was distinct.

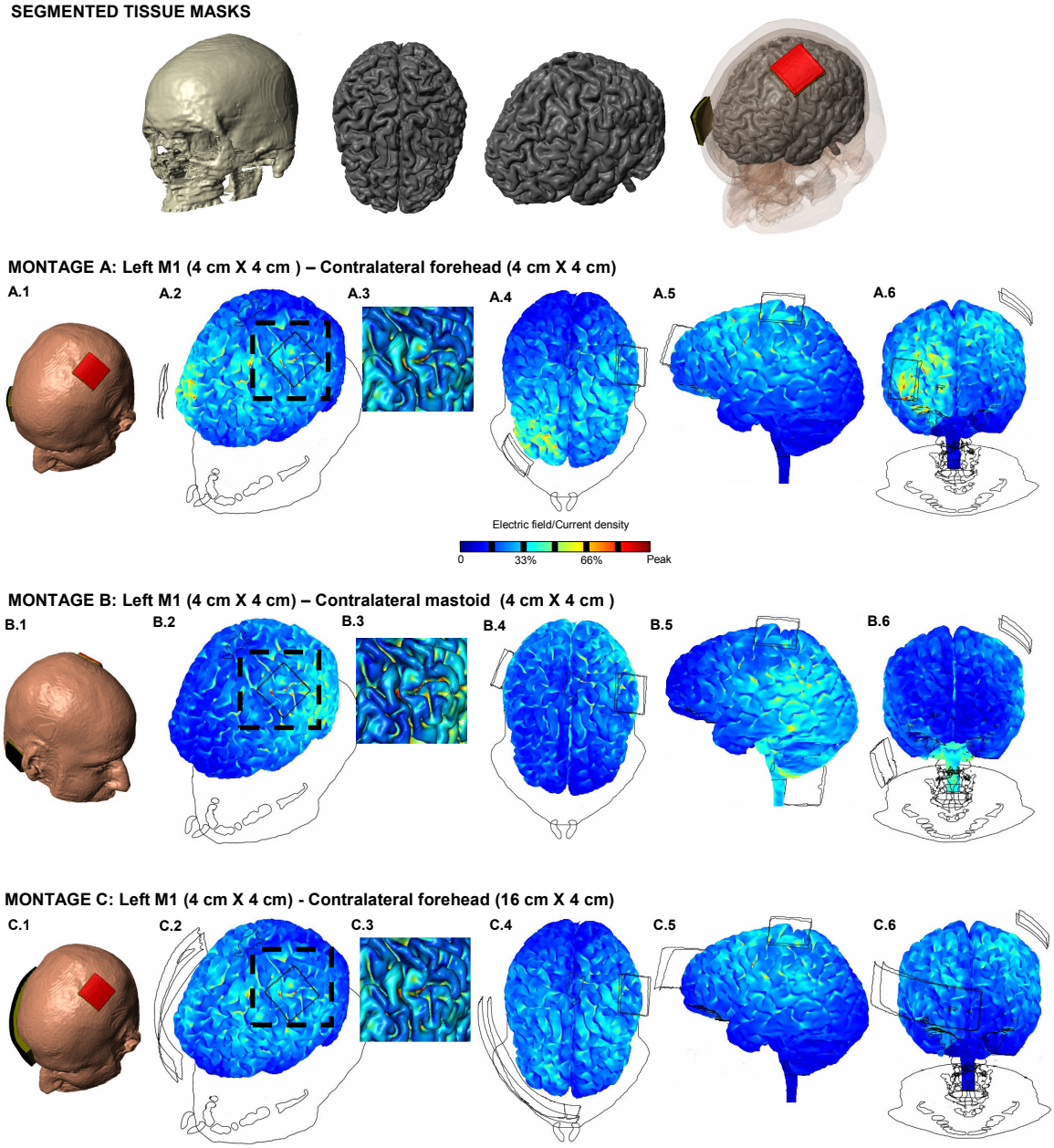


**Figure 14 Effect of "return" electrode's position and size on cortical electric fields induced by a 4 cm x 4 cm "active" electrode over the left primary motor cortex. Top row:** Sample segmentation masks. **A:** Stimulation with a 4 cm x 4 cm return electrode over the contralateral forehead (Montage A) **B:** Stimulation a 4 cm x 4 cm return electrode on the contralateral mastoid (approximating an extra-cephalic electrode; Montage B) **C:** Stimulation with a 16 cm x 4 cm electrode wrapped around the contralateral forehead (Montage C). All false color maps were generated between 0 and 0.44 V/m; the *peak* cortical EF magnitude induced in Montage A. The insets (A.3,B.3,C.3) highlight gyri/sulci modulation directly under the pad (with the "lighting on" feature).

## 7.4 Discussion

Our modeling results support the clinical finding by Moliadze et al. (2010) that even if the direct actions of the "return" electrode are mitigated by its position (e.g. extracephalic) or size (Nitsche et al., 2007); the "return" electrode will still influence the current path through the brain from the "active" electrode. For example, the re-positioning of the return pad from the contralateral forehead to the contralateral upper arm may have shifted the preferential flow of current from across the frontal regions to across the posterior regions of the brain (see Montage A and C versus Montage B in Figure 14). More generally, the regions of brain modulation may *not* be simply under the "active" electrode (Datta et al., 2009a; Lang et al., 2005; Sadleir et al., 2010), such that some "surprising" clinical findings, including by Moliadze and colleagues may be understood by considering the concurrent neuro-modulation of multiple cortical and sub-cortical regions. Additional experimental studies investigating the specific role of electrode placements and intensity, and careful consideration of electrode montage in designing therapeutic protocols, is warranted.

# Chapter 8: Cortical DC Stimulation in Fibromyalgia: Optimized clinical dosage supported by high-resolution computational models

## 8.1 Introduction

Based on recent neuroimaging and neurophysiological studies showing significant brain activity dysfunction in fibromyalgia, noninvasive brain stimulation has been tested as a potential treatment strategy for this condition. Trials using magnetic fields with transcranial magnetic stimulation (TMS) over the motor and prefrontal cortex have shown long lasting effects for pain decrease in patients and in healthy volunteers (Nahmias et al., 2009; Passard et al., 2007; Sampson et al., 2006). Studies with the another technique of noninvasive brain stimulation – transcranial direct current stimulation (tDCS) - have also shown positive results for pain reduction (Fregni et al., 2006a; Fregni et al., 2006c; McIntyre et al., 2004; Roizenblatt et al., 2007), and might be more effective in increasing pain tolerance than other forms of transcranial stimulation (Lefaucheur, 2006). tDCS has further advantages as it can be combined with other behavioral interventions while being a relatively safe, low cost, easy to apply technique that is readily shammed for clinical research (Lefaucheur, 2006; Nitsche et al., 2003b). Finally recent research has shown the benefits in sleep and depression (symptoms usually manifested in fibromyalgia) with the use of tDCS (Boggio et al., 2008; Roizenblatt et al., 2007).

Electrode montage (the position and size of electrodes) determine the resulting brain current flow and hence neuro-physiological effects (Nitsche and Paulus, 2000) and clinical outcomes. Indeed, the ability to customize tDCS treatment through electrode montage provides clinical flexibility and the potential to individualize therapies. At the same time, the need to understand and optimize electrode montages to treat specific diseases, such as fibromyalgia, remain a fundamental channel in tDCS – inconsistent findings in the literature may reflect poor control of montage. In this context we aimed to address several critical questions in the planning of clinical trials for fibromyalgia including: (i) of whether similar clinical effects can be induced with different electrode montages in fibromyalgia and (ii) of whether the use of extracephalic reference electrode is an effective strategy.

In this study we determined whether extracephalic stimulation (placing one return electrode outside the scalp area and using different active electrode positions on the scalp) is an effective strategy in fibromyalgia as indexed by pain reduction and by intracranial current distribution using a magnetic resonance imaging (MRI)-derived finite element head model. tDCS was applied at two of the most commonly used sites for the treatment chronic pain (primary motor cortex (M1) and fronto-polar area (SO). Both the M1 and supra-orbital region were stimulated with two poles (anode and cathode) in separate conditions. We used a computer head model to predict the location of current flow through the brain using the different electrode montages employed in this study. The significance of this approach lies in the combination of clinical evaluation and computer

head modeling data to investigate the effects of different electrode montages in reducing pain in fibromyalgia.

## 8.2 Materials and Methods

*Study Population*

This study consisted of a randomized, double-blind clinical trial conducted at the Advanced Physical Therapy Clinic (CAFIS) of the Bahiana School of Medicine and Public Health (EBMSP) in the period from September 2008 to November 2009 and a computer head modeling study conducted at the Neural Engineering Laboratory at The City College of New York of CUNY also in collaboration with the Laboratory of Neuromodulation (Spaulding Rehabilitation Hospital – Harvard Medical School). The study included 30 participants diagnosed with fibromyalgia by the criteria of the American College of Rheumatology (ACR), literate, and in the age group between 18 and 60 years. We excluded individuals on medication for pain control or undergoing physical treatment for less than two months; individuals with epilepsy and malignant diseases; pregnant women and infants; patients with metal implants in the encephalon or skull, and patients using illicit drugs.

All the participants were submitted to four stages of the study: (1) assessment for compatibility with the inclusion/exclusion criteria. The patients selected by the criteria signed a term of free and informed consent, and were provided with all the information with reference to the research. (2) pain assessment by an examiner blinded to the

treatment. (3) treatment with transcranial direct current stimulation or placebo. (4) re-assessment by the same examiner in stage two.

This study was approved by the Research Ethics Committee of the Bahiana School of Medicine and Public Health (EBMSP), No. 59/2008, and in agreement with Resolution 196/96 of the National Health Council (BRA).

*Assessment Methods*

Patients were assessed with the use of: (a) a Visual Numerical Scale (VNS) of pain, zero being no pain and 10 the worst possible pain; (b) the marking of areas of pain on a body map, and the total area (pixels/cm) of pain was assessed for each patient by an image editing program (Java Image, NIH, USA); (c) the measurement of pressure pain threshold (PPT) with the use of a pressure algometer (Pain Diagnostics & Thermographics Corporation, USA) to establish minimum pressure that triggers pain in the 18 pre-established points for the diagnosis of fibromyalgia (Wolfe et al., 1990). For statistical analysis we used a single value (sum of 18 points). All patients were submitted to the assessment before and immediately after a single session of tDCS.

*Transcranial Direct Current Stimulation (tDCS)*

Treatment was performed by a therapist with no knowledge of the measurements assessed and our hypotheses. As aforementioned, two stimulation sites that have been extensively used in recent research, in accordance with the International 10/20 System of Electrode Placement (Homan et al., 1987), were used: position C3, corresponding to the region of the primary motor cortex (M1) and the right supra-orbital area, corresponding

to the anterior prefrontal cortex region (PFC). The location of electrodes was through individual measurement.

Patients were randomly divided into five groups named according to the transcranial electrode: **Group Cat-M1 -** cathodal stimulation of the left M1 region; **Group Cat-SO**, cathodal of the right supra-orbital region; **Group Ano-M1** - anodal stimulation of the left M1. **Group Ano-SO** - anodal stimulation of the right supra-orbital region; and sham stimulation group. The peripheral electrode was placed over the transition of the cervical and thoracic spine (between the scapulas) in all the groups (any insight as to why as opposed to other extracephalic locations used in literature). We chose the left M1 and right SO as this has been used in several of our previous studies (Fregni et al., 2006a; Fregni et al., 2006c).

tDCS was performed using a universal pulse generator (941 NEMESYS, Quark Medical Products, Brazil) previously calibrated for the study. The treatment method used involved a single application of a direct current at an intensity of 2 mA for 20 minutes through pairs of aluminum-sponge surface electrodes of two sizes: 80x100 mm when used on the extracephalic position, and 40x40 mm when used cranially. For sham stimulation, current was turned ON only for the initial 30 seconds.

*Statistical Analysis*

Statistical Analysis was conducted using STATA 11.0 (College Station, Texas, US). Initially we conducted a group analysis running an ANOVA model in which the

main outcome was change in pain intensity and the independent variables were time (before vs. after) and condition of stimulation (groups of treatment) and the interaction term time*condition. We then performed post-hoc analysis using paired t-test to assess effects of each condition of stimulation. We tested data normality using Shapiro-Wilk test and if not normal we used non-parametric tests (Kruskal-Wallis and Wilcoxon). Finally we conducted exploratory correlation analysis between demographic characteristics and VNS changes.

*FEM model of induced brain current flow*

To consider the role of different electrode montages on induced brain current flow during tDCS, we developed finite element (FE) models. All models were based on a single MRI-derived head model from a healthy adult subject (who was not part of this study). We considered three electrode configurations (M1-extracephalic, SO-extracephalic and also M1-SO; although this last montage was not used in the present clinical study, this montage was used previously by our group in other studies and served as a means to compare the clinical and modeling results). The head model was created at the same resolution (1 mm x 1mm x 1 mm) as the MRI data used to derive it. The entire workflow including segmentation of data, mesh creation and the eventual export to a finite element method solver (SIMPLEWARE LTD., UK) was detailed previously (Datta et al., 2009a). Since the FEM model was directly derived from the subject's anatomical data and in order to approximate the exact clinical montage used, a *dummy* neck and shoulder region was fused onto the existing segmented head. For the model used in this paper (Figure 15) the electrical properties of the tissues are assigned representative

isotropic average values (in S/m): gray matter: 0.276; white matter: 0.126; CSF: 1.65; skull: 0.01; scalp: 0.465; muscle: 0.334; air: 1e-15; eye region: 0.4; and dummy region: 0.17. The blood vessel compartment was assigned the same tissue property as that of scalp.

We modeled the conventional "sponge-based" electrodes using in this study: 80x100 mm when used outside the head, and 40x40 mm when used over the scalp) and calculated the induced currents in the cortex resulting from application of 2 mA total current (corresponding to an average electrode surface current density of 0.28 A/m2 in the cranial electrode). We modeled three electrode montages (Figure 15): (a) M1-extracephalic: One electrode was placed over the primary motor cortex (corresponding to C3 according to the 10/20 EEG system) and the other electrode was placed over the cervical/thoracic transition dorsal midline. (b) Supraorbital-extracephalic: One electrode was placed over the supraorbital area and the other electrode was placed in the same extracephalic position as model A. (c) We performed a third modeling using the position of electrodes most used in studies to modulate chronic pain (M1-SO) as to have a comparison (this is the montage we used in our previous study (Fregni et al., 2006a; Fregni et al., 2006c). During conventional tDCS, rectangular sponges are typically soaked in saline and the abutting electrode is energized. The sponge was thus assigned the electrical conductivity of saline ($\sigma$=1.4 S/m) and the stimulation electrodes were modeled as conductors ($\sigma$=5.8×107 S/m). The electrodes had a thickness of 1 mm and the thickness of the sponge varied from 1 to 2.5 mm (Datta et al., 2009a).

The Laplace equation was solved and current densities corresponding to 2 mA total current were applied (Datta et al., 2009a). Surface-magnitude plots were generated for each of the montages by plotting the magnitude of EF on the cortical surface. All false color map plots were plotted between 0 and the *peak* EF magnitude induced in Montage A.

**8.3 Results**

Thirty individuals were included in this study (28 females, mean age of 43.2 years (± 9.8)). The clinical and demographic characteristics of the patients are shown in Table 1. Patients reported stimulation as no sensation or mild tingling. There were no adverse reactions and no dropouts.

All patients were either on medication and physical therapy to treat pain for more than two months or not taking medications or physical therapy for at least two months. The most used medications were: Codeine phosphate and paracetamol (33%), amitriptyline (26.6%), fluoxetine (16.6%), clonazepam (16.6%), dipyrone (10%) and ketoprofen (10%).

*Pain Intensity (VNS) and pain threshold (PPT)*

We initially conducted a group analysis using an ANOVA in which the dependent outcome was pain intensity (as indexed by VNS) and pain threshold (as indexed by PPT). This analysis revealed a significant interaction (between time and group) for both VNS and PPT ($F(9,28)=5.63$, $p=0.0002$ for VNS and $F(9,28)=2.23$, $p= 0.05$ for PPT). We then

conducted post-hoc testing that revealed significant pain decrease in the Cat-SO (t-test, p=0.0104) and Ano-SO groups (t-test, p=0.015) for VNS, showing that the supra-orbital region is important in analgesia provided by tDCS, irrespective of the pole used (Figure 16). There was a trend for a similar effect using PPT as the outcome but only in the Ano-SO group (t-test p=0.059) (Figure 16).

**TABLE 4**

Clinical and demographic characteristics

| | Group A | Group B | Group C | Group D | Sham | *p*-value* |
|---|---|---|---|---|---|---|
| Number (n) | 6 | 6 | 6 | 6 | 6 | |
| Age (years) | 41.8 (12.9) | 43.5 (8.5) | 44.5 (10.5) | 42.6 (9.2) | 43.5 (10.4) | 0.9 |
| Gender (female (%)) | 83.4% | 100% | 83.4% | 100% | 100% | |
| VNS pain – baseline | 6 (2.8) | 6.5 (1.8) | 5.5 (2.4) | 8.3 (2.7) | 8.6 (1.5) | 0.09 |
| PPT – baseline | 27.6 (10.4) | 19.6 (19.4) | 30.5 (15) | 22.2 (15.8) | 30.2 (12.5) | 0.6 |
| Pain location (pixels/cm) | 4.2 (4.3) | 8.2 (8.8) | 3.3 (1.4) | 6.5 (5) | 6.8 (6.3) | 0.5 |

* ANOVA one way for the comparison of variables

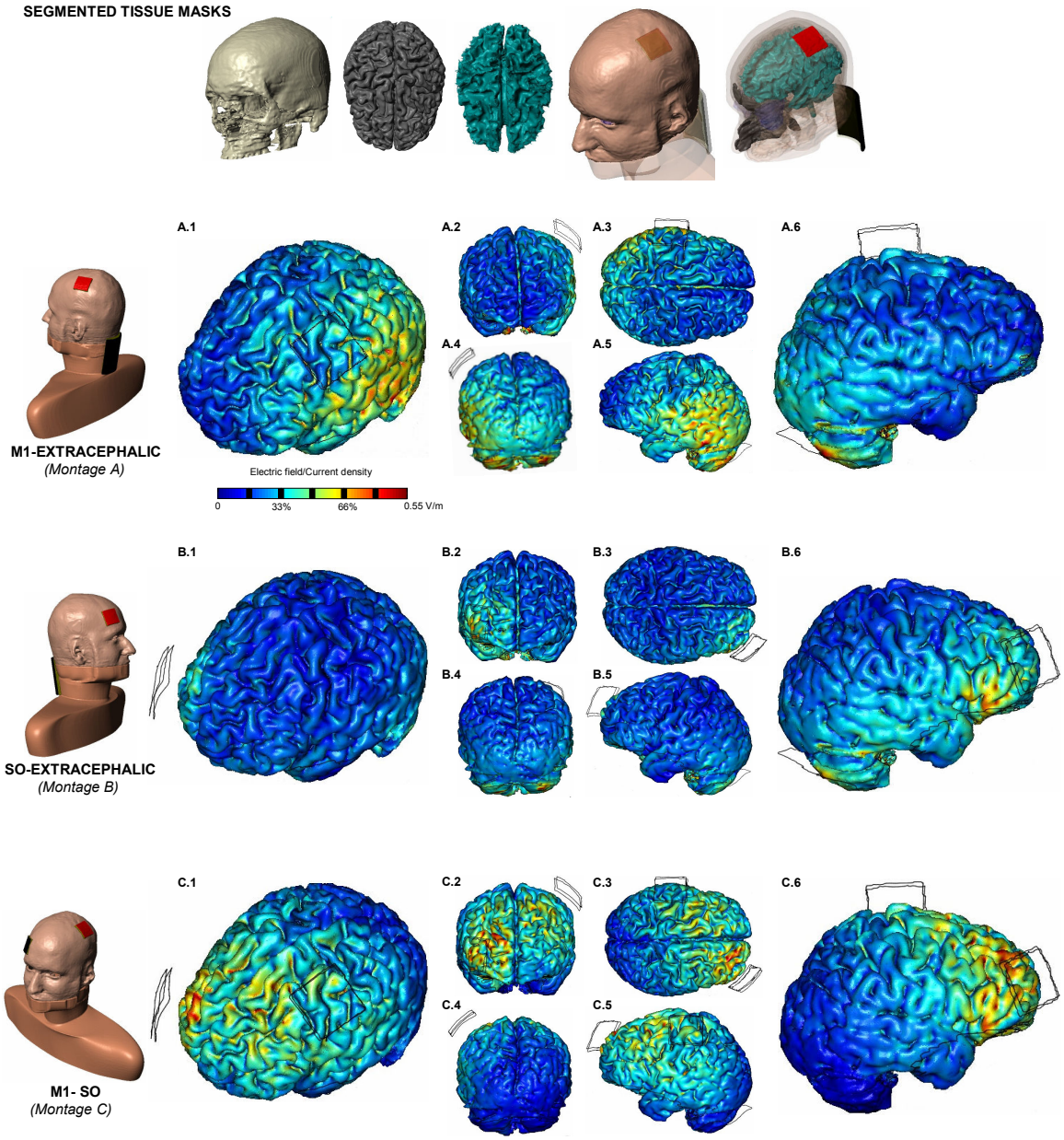


**Figure 15. Computational results of induced cortical currents during tDCS in Fibromyalgia using a 1 mm x 1 mm x 1 mm resolution head model. Montage A**: M1-extracephalic; **Montage B**: SO-extracephalic; **Montage C**: M1-SO (see Methods). For each montage, we calculated the induced cortical electric field (EF) magnitude. All false color maps were generated between 0 and 0.55 V/m; the peak cortical EF magnitude induced for Montage A. Surface magnitude plots of EF were generated with different views. **Top row:** Sample segmentation masks. **A.1** and **A.6**; **B.1** and **B.6**; **C1** and **C6** were generated at a higher zoom level to highlight current flow in the M1 region and the right side regions respectively. **A.2**, **B.2**, **C.2** show the frontal view while **A.4**, **B.4**, **C.4** show the posterior view. **A.3**, **B.3, C.3** show current flow in the top view and **A.5**, **B.5**, **C.5** show current flow in the left side regions.

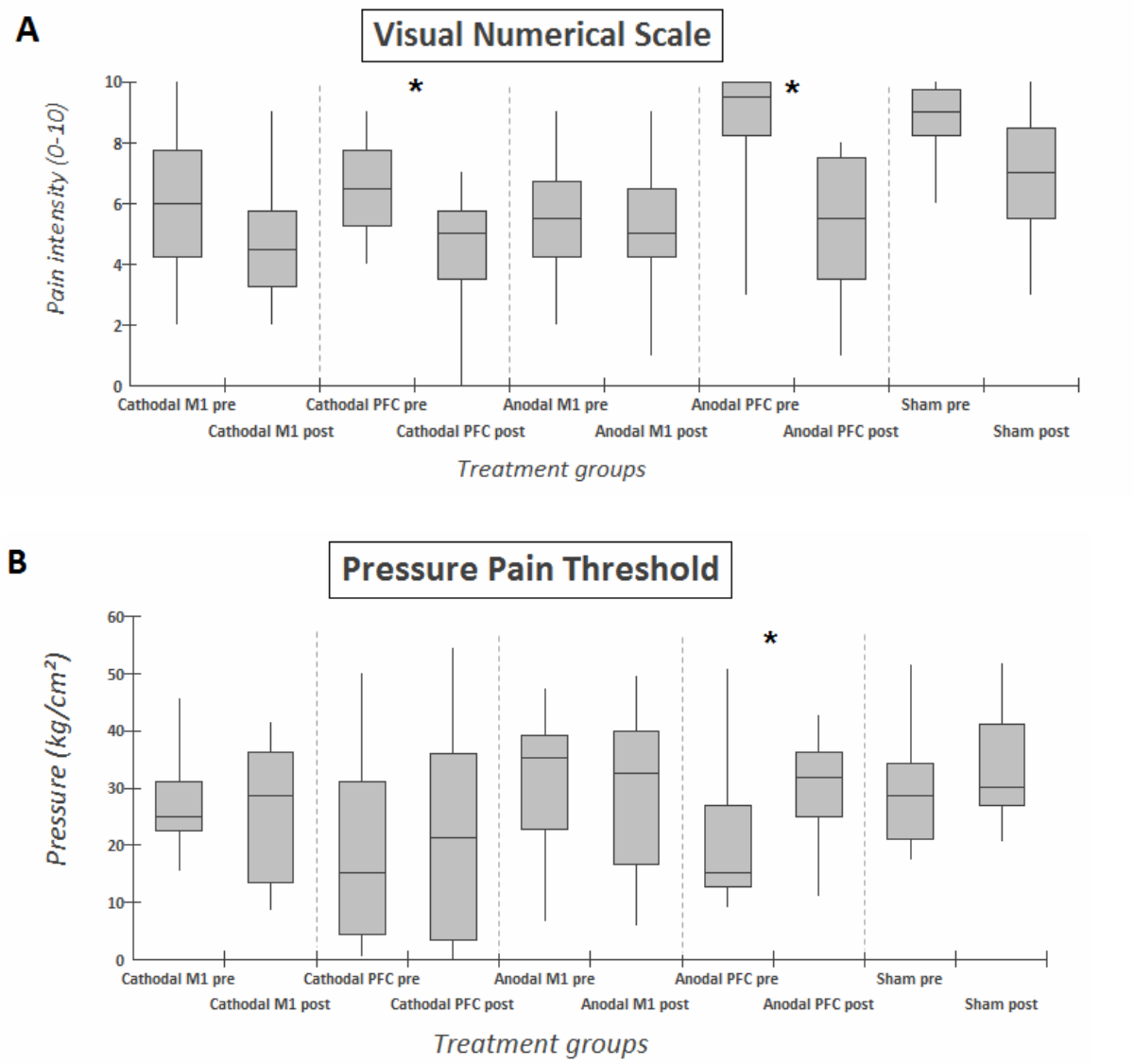


**Figure 16 Pain Intensity and Pain Pressure Threshold ratings** (A) Demonstrates the scores of pain intensity before and after treatment in each group. There was a significant reduction in pain intensity in the CSO and ASO groups. (B) Scores of pain pressure threshold before and after treatment in each group. There was an improvement in the pain threshold in the ASO group. * Indicates significantly different values (Wilcoxon, $p < 0.05$). The measures are represented by median and interquartile values.

*Pain representation*

Here we used a non-parametrical test, because we found a skewed distribution of values. Therefore for the group analysis we used Kruskal-Wallis. This analysis showed no significant differences across groups ($p=0.21$). We therefore did not conduct post-hoc analysis for this outcome.

*Correlations*

We performed an analysis to search for correlation between demographic characteristics and pain reduction, and we did not find any significant correlations for the active conditions.

*Computer head modeling*

We modeled the current distribution in the head during tDCS with 2 mA using the two electrode montages evaluated here, and one additional montage used in a previous treatment study. We considered the electric field magnitude distribution and the peak electric field induced along the cortical surface. The M1-extracephalic montage stimulation resulted in 0.55 V/m peak cortical electric field magnitude. Importantly (differently than the traditional M1-SO montage) (see Figure 15,A and Figure 15,C ), current was localized in the temporo-parietal cortex and not over the motor cortex. The SO-extracephalic electrode configuration resulted in peak EF being more localized under the frontal electrode. The M1-SO configuration also resulted in peak cortical electric field in the frontal regions (Figure 15,C) but with significant electric field/current flow in the cortical regions between electrodes (comparable to Datta et al., 2009).

## 8.4 Discussion

Our results confirm and show for the first time in a clinical setting the important notion that current distribution is critical for the effects of tDCS in reducing pain in fibromyalgia. Here we showed that using the cortical sites associated with positive effects (montage M1-SO) but in a isolated manner with a different current distribution (using extracephalic electrodes) resulted in a lack of effects for primary motor cortex stimulation and in positive effects for supra-orbital electrodes. Importantly there was a strong association between the clinical and modeling results such as only electrode montages producing significant current flow through relevant brain structures produced positive clinical effects.

One interesting aspect is that cathodal or anodal stimulation of the supra-orbital region had an important influence on the pain variables studied, pointing to the fact that the prefrontal cortex (in addition to the primary motor cortex) is a critical region in the modulation of pain in patients with fibromyalgia. This region has many connections with the other brain structures that are highly involved in pain modulation such as the medial dorsal nucleus of the thalamus, the limbic association cortex, hypothalamus, and the periaqueductal gray substance (de Leeuw et al., 2005; Millan, 2002). These connections are associated with an important role in the modulation of emotions, particularly anxiety and fear (Davidson, 2002; Morgan et al., 1993; Simpson et al., 2001), and behavioral characteristics of attention and perception (Barbas, 2000; Cardinal et al., 2002; Rempel-Clower and Barbas, 1998). In fact studies using neuromodulation techniques over the

prefrontal cortex showed positive results to decrease pain threshold in healthy volunteers using tDCS and TMS (Boggio et al., 2008; Borckardt et al., 2007; Nahmias et al., 2009). The stimulation of this region also shows positive results for patients with chronic pain using TMS (Borckardt et al., 2009b; Sampson et al., 2006) showing that the prefrontal cortex is a possible target for treatment of patients with chronic pain with other brain stimulation methods such as tDCS. One important point is that we observed a similar effect for anodal and cathodal stimulation over the SO area and therefore raises the question of whether modulation of different inhibitory and excitatory circuits within the anterior prefrontal cortex leads to modulation of pain-related neural circuits. Although most of the studies targeted DLPFC and not fronto-polar areas as we did in our study, it is possible that this area is as effective as DLPFC for the modulation of pain-related circuits. Finally, the observation that presumed PFC with a SO electrode has clinical significant effects raises interesting questions about numerous studies (including by our groups) where an SO-electrodes was use as a (nominally inactive) "return" – our results indicate this "return" may modulate clinical outcome.

On the other hand, electrode montages with cathodal or anodal stimulation over regions of the primary motor cortex (M1) *with an extracephalic return* did not produce significant analgesic effect. At first glance, without accurate consideration of induced cortical current flow (e.g. with models), this result would be appear to contrast with extensive invasive and noninvasive brain stimulation data showing that primary motor cortex is an excellent target for the treatment of chronic pain (see review Lima and Fregni, 2008). Indeed previous tDCS studies have shown that positioning the anode in

M1 *and the cathode in the supra-orbital region* (M1-SO) had analgesic effects under several conditions (Fregni et al., 2006a; Fregni et al., 2006c; McIntyre et al., 2004; Roizenblatt et al., 2007). Stimulation of primary motor cortex activates superficial layers of the motor cortex (intercortical interneurons – rather than corticospinal axons) that convey stimulation to different areas: (i) thalamocortical projections from ventrolateral-ventral anterior (VL-VA) thalamic nuclei, (ii) collaterals of cortico-cortical projections – especially postcentral and premotor cortex, (iii) local cortical connections in parallel to the cortical layers. This activation propagates both orthodromically and antidromically leading to a cascade of synaptic events resulting in modulation in an extensive neural network that includes thalamic nuclei, limbic system, brainstem nuclei and spinal cord. Indeed both techniques are associated with activation in extensive neural networks (Lima and Fregni, 2008). However, in this study, computer modeling results indicate that the M1-extracephalic montage produces a dominant current flow pattern that largely avoids M1 – consistent with this montage producing insignificant analgesic effects. The role of return electrode position (and size) in modulating neurophysiological effects under the "active" electrode is established (Bikson et al., 2010; Moliadze et al., 2010; Nitsche and Paulus, 2000). Our findings here using extracephalic electrodes, taken together with the aforementioned M1-SO results, provide the clearest evidence to date of the importance of total electrode montage ("active" *and* "return") design in determining clinical outcome; moreover, our clinical findings substantiate the need and utility of accurate computer model of cortical current flow. More generally, our results provide specific insights into the broader and application specific debate about the use of extracephalic electrodes, including how the use of an extracephalic electrode may profoundly effect cortical

actions under and around “active” electrodes and hence account, in part, for variability across studies.

This trial gives some insights on the cortical mechanisms of pain modulation as we showed with a modeling and clinical data cortical areas associated with pain modulation. In addition we showed that extracephalic montage might not induce significant currents in the area under the electrode and therefore current distribution needs to be carefully addressed in studies using this montage. There are some limitations in our trial. First, the small sample of the subgroups might have resulted in false negative results; however, there was not even a trend for significant results when analyzing data from M1 stimulation. Another potential limitation is that we did not measure neurophysiological data in this study; however because we decided to study also prefrontal cortex as an isolated area, TMS-cortical excitability would not be helpful in this case. Also we wanted to show clinical changes associated with location of stimulation (from modeling studies). It is also important to note that our computational results were based on a *single* individualized MRI derived head model. Inter-individual variability (Datta et al., 2009a) may influence the magnitude and the spatial extent of induced cortical fields predicted in this study.

In conclusion, it was observed that the stimulation of the prefrontal cortex with tDCS, irrespective of the polarity of the electrode, resulted in acute improvement of the algic condition in patients with fibromyalgia, and that the stimulation of the M1 area using the extracephalic electrode had no immediate analgesic effect. Our study showed

that the electrodes montage is fundamental to achieve a positive result in pain decrease. The usage of extracephalic electrodes over the motor cortex or prefrontal cortex activates different cortical areas compared with the use of two electrodes over the scalp. These findings should be taken into consideration in future tDCS studies for pain treatment.

# Chapter 9: Individualized model of responsive transcranial direct-current stimulation stroke patient: Retrospective Analysis

## 9.1 Introduction

Transcranial direct-current stimulation (tDCS) is a noninvasive and safe technique designed for modulating cortical activity through the delivery of a weak polarizing electrical current via electrodes placed on the scalp (Nitsche and Paulus, 2000). tDCS has been evaluated to modulate cognitive, linguistic, and motor performance in both healthy and neurologically-impaired individuals- with results supporting the feasibility of leveraging interactions between stimulation-induced neuromodulation and task execution (Iyer et al., 2005; Sparing et al., 2008; Hummel and Cohen, 2005). For instance, we recently demonstrated that the application of anodal tDCS (A-tDCS) to the left frontal cortex significantly enhanced the effect of aphasia treatment in chronic stroke (Baker et al., 2010).

Electrode montage (i.e. the position and size of electrodes) determines the resulting brain current flow and, as a result, neurophysiological effects. The ability to customize tDCS treatment through electrode montage provides clinical flexibility and the potential to individualize therapies (Sunderam et al., 2010). However, while numerous reports have been published in recent years demonstrating the effects of tDCS upon task performance, there remain fundamental questions about the optimal design of electrode configurations. Moreover, it is expected that lesioned tissue will influence current flow

(Wagner et al., 2007) and should therefore be considered in the design of individualized tDCS therapies for stroke.

Computational models using finite-element-methods (FEM) are standard tools for predicting current flow through the brain during tDCS, and thus have the potential to inform therapeutic strategies. Here we present results from the first high-resolution (1 $mm^3$ ) model of tDCS in a brain with lesioned tissue; the model was individualized to the patient who participated in our aforementioned chronic stroke tDCS study (Baker et al., 2010) and was classified as a responder to the tDCS treatment condition as compared to the sham treatment condition. The patient received A-tDCS to his left frontal cortex (Broadmann area [BA] 6) with the reference cathode electrode placed on his the right shoulder. Here we model the resulting brain current flow and consider two additional cathode electrode configurations: right mastoid and right orbitofrontal cortex.

## 9.2 Materials and Methods

*Clinical Summary*

A 60-year-old male sustained a left hemisphere ischemic stroke 64-months prior to his participation in our aforementioned tDCS study (Baker et al., 2010). He suffered damage to BA 44, BA 45, BA 38, as well as the middle and anterior insula (lesion size = 87.42 cc). According to the *Western Aphasia Battery-Revised* (Kertesz, 2007), the patient's language deficits are most consistent with Broca's aphasia (Aphasia Quotient = 72.1/100). He received five days of A-tDCS (1 mA; 20 min) and five days of sham tDCS

(S-tDCS; 20 min) while performing a computerized anomia treatment. Following A-tDCS treatment, the patient named 64.71% more of the treated and untreated nouns immediately following the fifth (and final) treatment session (T1) as compared to baseline and 52.94% more of the treated and untreated nouns one-week following the final treatment session (T2) as compared to baseline. Following S-tDCS, he named 4.08% less of the treated and untreated nouns at T1 as compared to baseline and 2.04% less of the treated and untreated nouns at T2 as compared to baseline.

*MRI derived high-resolution model*

The individualized head model was created from 1 $mm^3$ resolution T1-weighted and T2-weighted magnetic resonance imaging (MRI) scans of the patient collected using a 3 T Siemens Trio scanner (Erlangen, Germany) with a 12 element head-coil. Using a combination of tools from the Functional MRI of the Brain (FMRIB) Software Library (FSL) (United Kingdom) and Simpleware (United Kingdom), the patient's head was segmented into compartments representing gray matter, white matter, cerebrospinal fluid (CSF), skull, scalp, eye region, muscle, air, and blood vessels (Custom Segmentation, Soterix LLC, NY, USA; Figure 17). The lesion site was classified as CSF (Wagner et al., 2007; Datta et al., 2010). The finite element (FE) mesh generated from the segmentation masks was exported to COMSOL Multiphysics 3.5a (Burlington, Massachusetts) for computation of electric fields (Datta et al., 2009).

*Model solution*

We modeled three electrode configurations: (1) Right Shoulder, (2) Right Mastoid and (3) Right Orbitofrontal Cortex (Figure 17). Since the head model was directly derived from previously collected MRI data, it was limited to the anatomical sections collected (Fridriksson et al., 2009). Thus, in order to model the extracephalic clinical montage used in our aforementioned tDCS study (Baker et al., 2010), a synthetic neck and shoulder region was fused onto the existing segmented head. The stimulation electrodes were modeled as 5 x 5 cm sponge-based electrodes and current densities corresponding to 1 mA total current were applied (Baker et al., 2010; Datta et al., 2009; Datta et al., 2010). The following isotropic electrical conductivities (in S/m) were assigned: gray matter: 0.276; white matter: 0.126; CSF: 1.65; skull: 0.01; scalp: 0.465; eye region: 0.4; air: 1e-15; synthetic region: 0.35; sponge: 1.4; electrode: 5.8e7 (Wagner et al., 2007; Datta et al., 2009). The muscle and blood vessel compartments were assigned the conductivity of scalp tissue. The Laplace equation was solved and induced cortical electric field (EF) magnitude maps for the different electrode montages were determined (Figure 17, 18) (Datta et al., 2009).

**9.3 Results**

The current flow pattern through the brain during tDCS was significantly modulated by the presence of the lesion (Figure 17, 18) as compared to a healthy head (Datta et al., 2009). Significant changes in the resulting cortical electric fields were

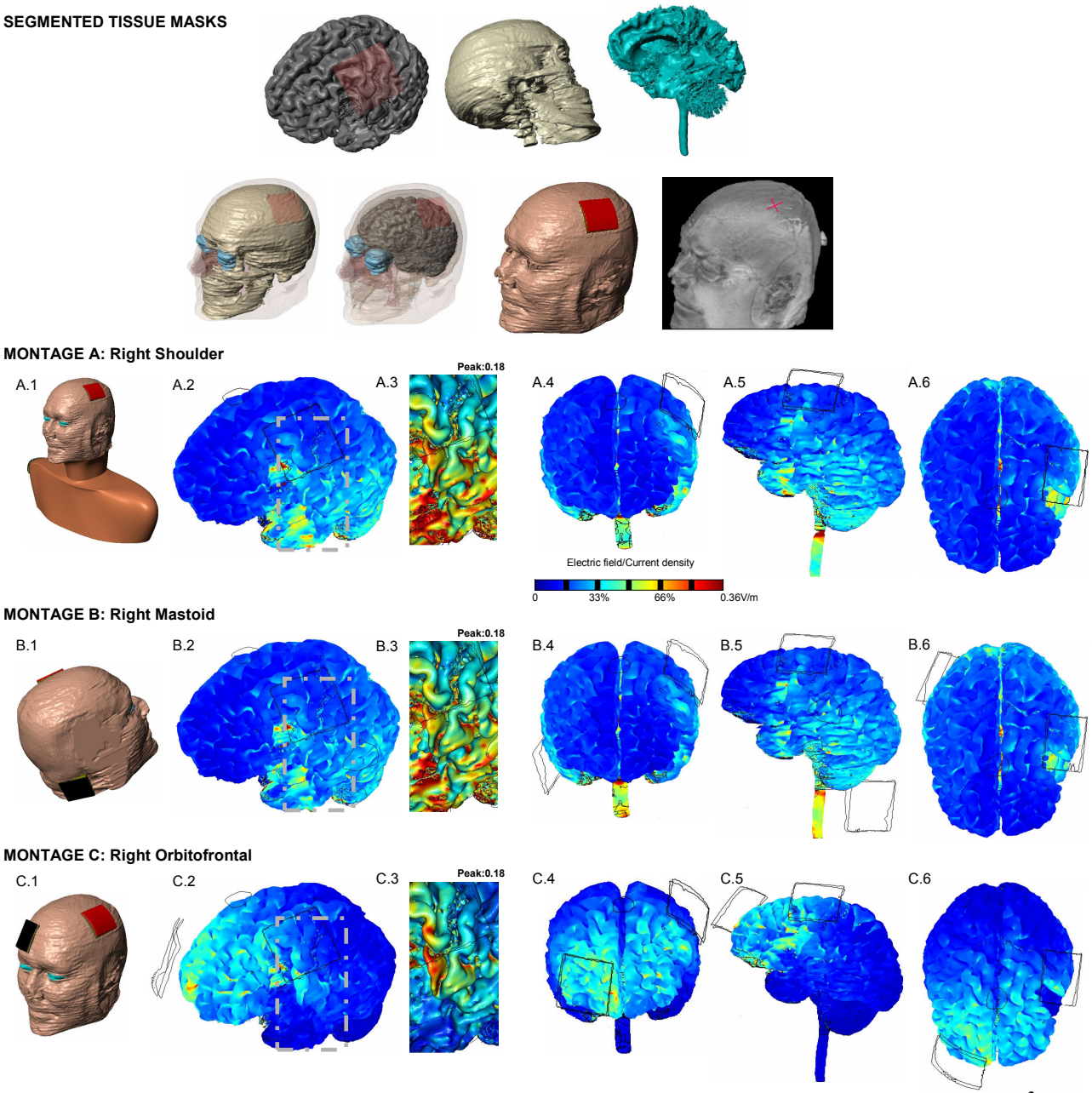


**Figure 17. Computational results of induced cortical currents during tDCS using a 1 mm$^3$ resolution patient-specific head model.** The top two rows show sample segmentation masks. Juxtaposed images of the FE model (derived from the segmentation masks) and 3D model (derived from patient's MRI scans using MRIcro) are also shown. **Montage A**: Right Shoulder; **Montage B**: Right Mastoid; **Montage C**: Right Orbitofrontal. All false color maps were generated between 0 and 0.36 V/m; the *peak* cortical electric field (EF) magnitude induced for Montage A. Surface magnitude plots of EF were generated with different views. **A.2, B.2, C.2** show current flow in the *lesional* and *peri-lesional* areas. The dashed region is expanded in **A.3, B.3, C.3** and scaled between 0 and 0.18 V/m (half of the *peak* induced electric field for Montage A) to highlight current flow in the *posterior peri-lesional* areas. **A.4**, **B.4**, **C.4**: Frontal view **A.5**, **B.5**, **C.5**: Left side view. **A.6**, **B.6, C.6:** Top view.

observed around both the peri-lesional region and wider cortical regions. The relatively conductive lesion concentrated current in the peri-lesional area, especially in deep brain regions between stimulation electrodes (Figure 17.A.3, 17.B.3, 17.C.3). As in the healthy head (Datta et al., 2009), the overall current pattern was complex, reflecting the overall detailed neuroanatomy and convoluted cortical topography. For example, the highly conductive ventricles resulted in a preferential current flow reflected in surrounding brain regions; together with the lesioned region forming a highly attractive current path.

The position of the reference cathode significantly affected brain current flow and resulting electric fields both in the peri-lesional and wider cortical lesions. With an orbitofrontal cathode, current flow was most restricted to the upper hemispheres, with significant electric fields in the cortex under the cathode (Figure 17C). Generally, moving the cathode to the contralateral shoulder (Figure 17A) and to the contralateral mastoid (Figure 17B), increased the current flow in the temporal lobes and brainstem. The current flow was however modulated in a complex and detailed manner. The right shoulder montage resulted in the highest and the most widespread electric fields in the posterior

**Figure 18. Cross section cortical electric field plots of induced currents for the different montages.** All false color maps were generated between 0 and 0.36 V/m; the peak cortical EF magnitude induced for Montage A. First Column: For all the plots, the corresponding coronal MRI scans collected for the subject is shown. The slices were chosen to highlight cross-sectional current flow in the *lesional* and *posterior peri-lesional* areas. Second Column**:** Right Shoulder; Third Column: Right Mastoid; Fourth Column: Right Orbitofrontal

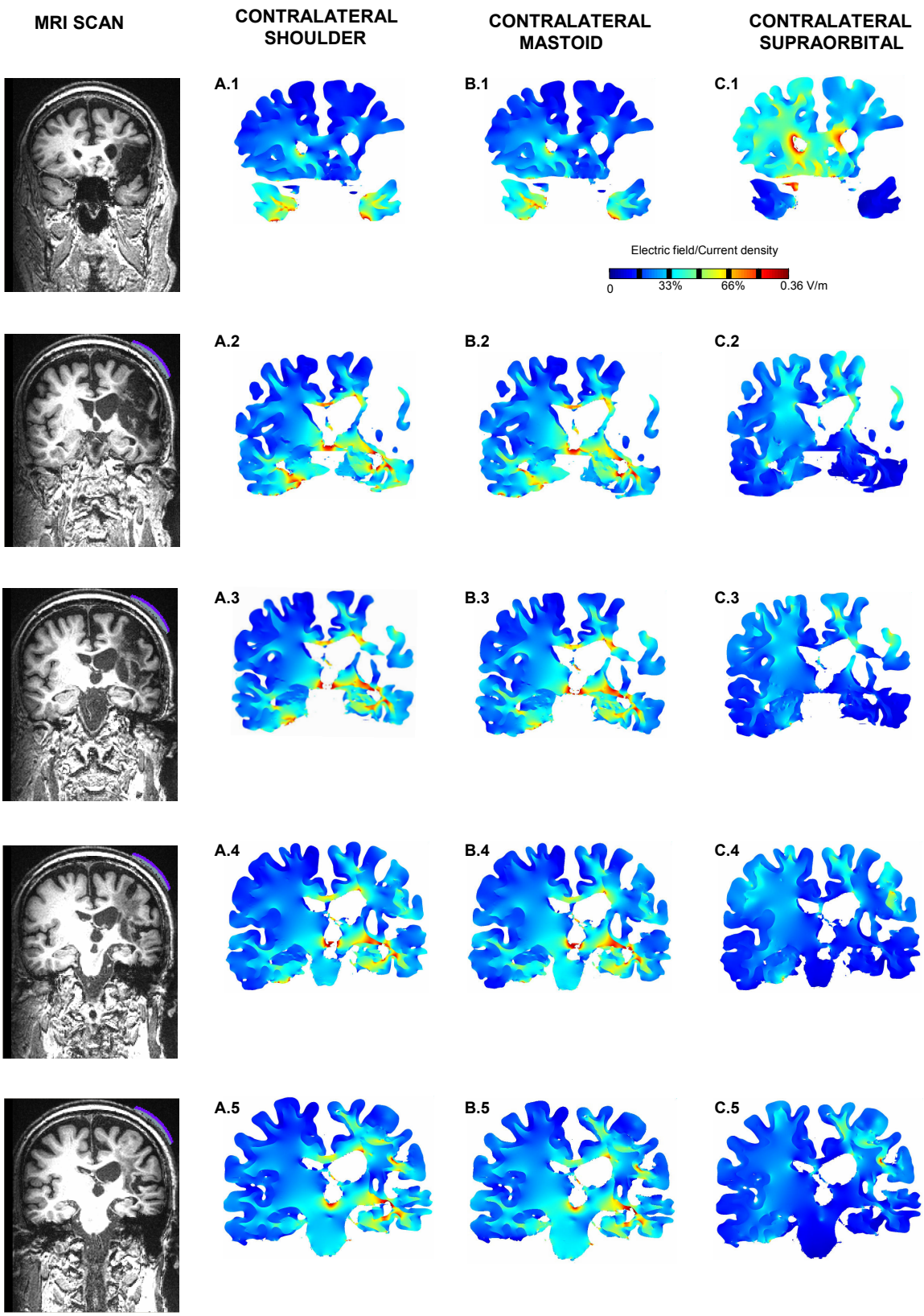
MRI SCAN
CONTRALATERAL SHOULDER
CONTRALATERAL MASTOID
CONTRALATERAL SUPRAORBITAL
A.1
B.1
C.1
Electric field/Current density
0
33%
66%
0.36 V/m
A.2
B.2
C.2
A.3
B.3
C.3
A.4
B.4
C.4
A.5
B.5
C.5

peri-lesional cortex (in the cortex roughly under the anode), while the orbitofrontal cathode montage produced the highest electric field in cortical region anterior to the lesion, including anterior peri-lesional cortex.

### 9.4 Discussion

If tDCS continues to be revealed as a viable option for treatment in chronic stroke, the consideration of tDCS-induced current flow through the brain is of fundamental importance for the identification of candidates, optimization of electrotherapies for specific brain targets, and interpretation of patient-specific results - thus the ability to individualize tDCS therapy must be leveraged. Whereas, tDCS electrode montages are commonly designed using general rules (e.g., anode positioned "over" the target region), our results reinforce the complexity of current flow, including the critical importance of "return" electrode positioning (Bikson et al., 2010), and thus the value of applying predictive modeling as one tool in the rational design of safe and effective electrotherapies. Moreover, our results support the value of individualized models and therapy design because of the profound effect of cortical damage on overall current flow.

The tools developed for this case-report represent the state-of-the-art in high-resolution individualized modeling. Nonetheless, continued technical improvements are indicated. Namely, further automation of the modeling process (critical for economical

and broad dissemination) and additional sophistication in the imaging and modeling tissue properties around lesions is needed.

In closing, the accuracy of predictions using forward models is limited by the precise representation of anatomy. Our development of high-resolution individualized models is thus an important advancement towards the use of computer models to retrospectively analyze results and prospectively design optimal electrotherapies (Palm et al., 2008).

# Chapter 10: Experimental and finite element model analysis of scalp potentials induced during transcranial electrical stimulation; implications for clinical dose

## 10.1 Introduction

Transcranial electrical stimulation encompasses a range of clinical and experimental protocols which apply current through scalp electrodes for the purpose of modulating brain function (Calancie et al., 1998; Nitsche and Paulus, 2000; Schroeder and Barr, 2001; Zentner, 1989), including transcranial direct current stimulation (tDCS) and cranial electrotherapy stimulation (CES). In all cases, applied current first distributes throughout the scalp, and then passes across the skull and CSF, eventually entering the brain (Datta et al., 2009a). The goal of this study was to characterize scalp voltage "artifacts" generated during transcranial electrical stimulation and to determine how these voltages can be used to understand and refine transcranial electrical stimulation protocols.

For example, understanding the current distribution in the brain during transcranial electrical stimulation is paramount for rational and safe stimulation. Animal models, resected skulls, and synthetic phantoms are of limited use in this regard because of the critical importance of anatomy and material properties. "Forward" models of transcranial electrical stimulation predict brain current flow (Datta et al., 2008; Miranda et al., 2006; Rush and Driscoll, 1968; Saypol et al., 1991) and increasingly detailed

forward models using finite element methods (FEM) have been developed (Butson et al., 2007; Datta et al., 2009a; De Lucia et al., 2007). As FEM models may be used to characterize clinical electrotherapies as well as design new electrode montages (Butson et al., 2007; Datta et al., 2009a; Holsheimer, 1998) it is important to experimentally validate the accuracy of these FEM models. Toward this end, though it is evidently not safe to record clinically with invasive intra-cortical electrodes, it is practical to record surface "artifact" potentials on the scalp that are generated during transcranial electrical stimulation.

We propose that during transcranial electrical stimulation, electrode configuration determines current distribution through the scalp, which is reflected in scalp voltage maps, and which ultimately determines the distribution of brain current flow. Here we mapped scalp voltage artifacts and validated the accuracy of a subject-specific FEM model of transcranial electrical stimulation. To precisely control the applied electrical stimulation, we used specialized high-definition stimulation electrodes (Minhas et al., 2010), rather than large "sponge" electrodes. We tested three illustrative high-definition stimulation montages: 1) proximal-dipole (one electrode at Cz and one electrode at C2 ); 2) distant-dipole (one electrode at Cz and one electrode at AF4); 3) and the 4x1 concentric-ring configuration (one electrode at Cz surrounded by four return electrodes; Datta et al., 2009). We show that these montages result in distinct scalp surface artifacts that are precisely predicted by our high-resolution FEM model. Moreover, we illustrate how these surface artifacts provide insight into the distribution of brain current flow, and can thus be used to in the design of effective and specific transcranial electrical

stimulation electrode montages. Finally, we discuss how online artifact measurement can be used to increase the safety of transcranial electrical stimulation.

## 10.2 Methods

*Imaging and Computational Methods:*

*MRI Acquisition and Segmentation*

MRI of brain was performed on a 34 year old male with no neurological pathologies using a 3T Philips Achieva MRI scanner (Philips Medical Systems, Cleveland, Best, Netherlands). Three-dimensional spoiled gradient image (SPGR) was acquired with TE/TR = 3 ms/6.6 ms, flip angle = 8, acquisition matrix=256x256x190, voxel size=1x1x1 mm.

Automatic segmentation was performed by FSL's Brain Extraction Tool (BET) (Smith, 2002)and FSL's Automated Segmentation Toolbox (FAST) (Zhang et al., 2001). The head was initially segmented into four compartments: scalp, skull, cerebrospinal fluid (CSF), and brain. Manual editing (Soterix, New York, NY) was performed to correct segmentation errors and to further segment the head into additional tissue types: eye, muscle, air (Simpleware Ltd, Exeter, United Kingdom).

*Stimulating electrode configurations*

Following the 10-10 international system (conventionally used in EEG) 64 electrodes were automatically positioned on the segmented scalp surface using a

customized MATLAB script. All simulated electrodes were ~2 mm thick with a diameter of ~12 mm separated from the scalp by a 1-2 mm thick layer of gel. 2 or 5 electrodes were energized as stimulating electrodes according to one of following three electrode configurations; the remaining electrodes were not activated.

Three stimulation configurations were modeled and then tested experimentally:

1) Proximal-Dipole: Stimulation with active electrode positioned at C2 and return electrode at C2.

2) Distant-Dipole: Stimulation with active electrode positioned at AF4 and return electrode at Cz.

3) 4 X 1 Concentric-ring: Stimulation with one return electrode at Cz surrounded by four active electrodes at Fz, Pz, C3, C4.

*FEM Analysis*

The Laplace equation was solved and the boundary conditions used were: 1) inward current flow = Jn (normal current density) applied to the distal surface of the anode(s) electrode current, (2) ground condition applied to the distal surface of the return electrode and (3) all other external surfaces treated as insulated (thereby also including all recording electrodes). The electrical properties of the different compartments in the model were assigned the following conductivity values: (in units of S/m) scalp: 0.465; skull: 0.01; CSF: 1.65; Brain: 0.2; eye region: 0.4; muscle: 0.334; air: 1e-15; electrodes: 5.8e7 and gel: 0.3.

*Experimental Methods:*

All experiments were approved by The City College of New York IRB. Experiments were performed on one 34 year old male, also used for individualized brain modeling. The subject was fitted with a conventional EEG cap (EASYCAP, BrainVision LLC) with 64 electrode positions following the 10-10 international system; 2 or 5 positions were fitted with stimulation electrodes according to the three electrode configurations evaluated (as above), and the remaining positions were used for recording.

*Transcranial Electrical Stimulation*

Transcranial electrical stimulation was applied using either an AM system analog isolated current source (A-M Systems, USA) driven by a function generator (AFG 320, Tektronix, USA) or stand-alone Soterix 1x1 and 4x1 stimulators (Soterix, New York, NY). Current was delivered using high-density stimulation electrodes (diameter: 12 mm) and CCNY4 gel, where the stimulating electrodes replaced recording electrodes in the head-gear according to the stimulation configuration.

To minimize skin sensation and avoid irritation but maximize artifact signal to noise ratio (S/N), ~0.4 mA peak current with a monophasic square wave or monophasic (offset) sine wave waveform was typically used for mapping measurements. But, as we validated the linearity of induced scalp potential with current amplitude (Figure 20), all

results are normalized to per-mA-of-current. Stimulation was applied in repeated exposures each less than 1 minute.

*Surface Voltage Measurements*

The surface voltage artifacts induced by transcranial electrical stimulation were measured using methodology similar to EEG. We used two approaches to measure induced scalp potentials; the two technologies yielded identical results. In once case, scalp potentials were measured sequentially between pairs of electrodes using a custom-made instrumentation amplifier. In the second case, scalp potentials were simultaneously measured from all scalp electrodes using the Biosemi EEG system. In both cases, scalp potentials were measured using 8mm diameter electrodes at multiple locations on the scalp following the 10-10 system - omitting the locations occupied by the stimulating electrodes (though the potential applied to the stimulating electrodes could be measured as the output of the current source, we suspected that because of the electrode interface voltage, this potential did not reflect the voltage at the scalp *under* the stimulation electrodes).

**10.3 Results**

The main objective of this study was to characterize scalp potentials induced during transcranial electrical stimulation. In the process we validated the accuracy of a high-resolution individualized FEM forward model of transcranial electrical stimulation

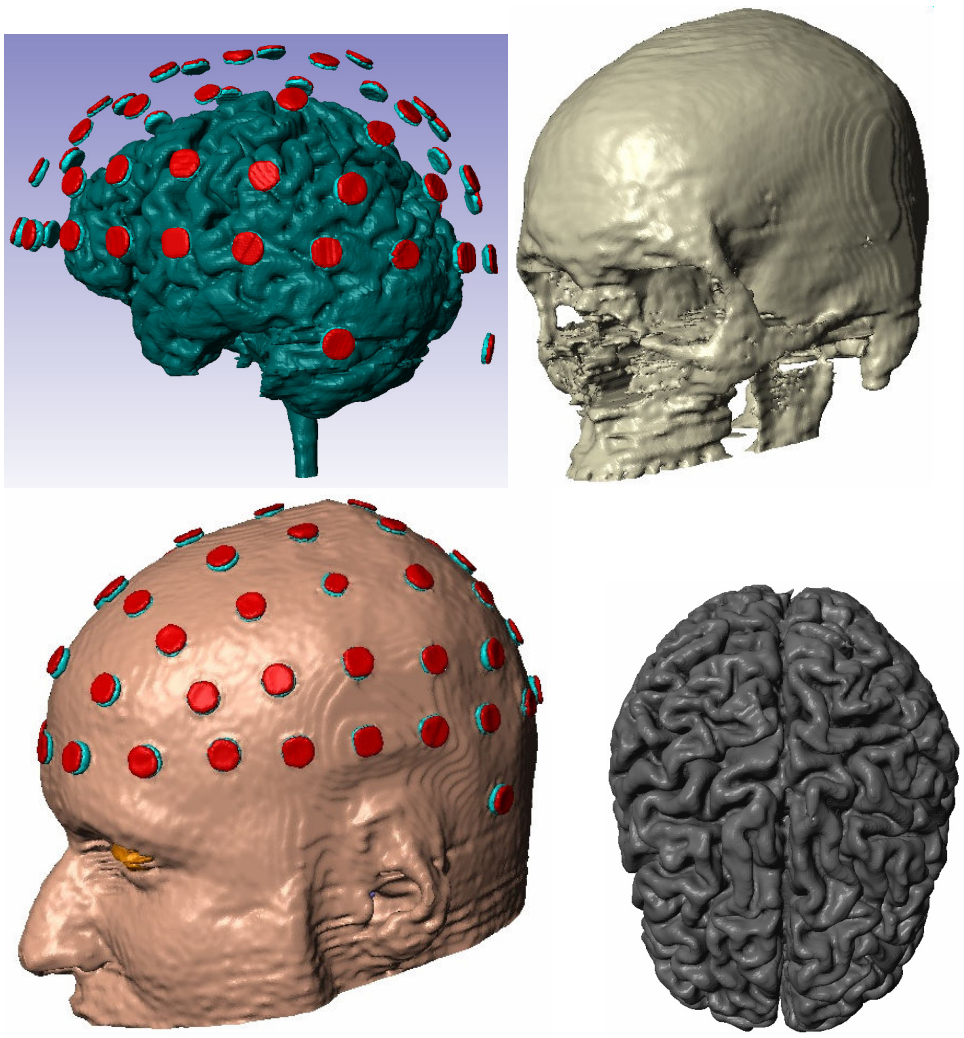

**Figure 19. Segmentation of the subject-specific FEM model.** For both experiment and model, transcranial electrical stimulation was applied using three electrode montages: proximal bipolar, distant bipolar, and 4x1 concentric ring. The remaining electrodes were used to measure the resulting artifact voltage induced on the scalp.

by comparing predicted and measured induced scalp voltages. We evaluated three electrode montages to further consider implications for clinical electrode configuration design. As part of this analysis, we verified the temporal and spatial linearity of scalp voltages for low current intensity and frequency.

*Linearity of scalp voltage artifacts with stimulation current amplitude and waveform*

For relatively low frequency and amplitude, we show that scalp voltage artifact amplitude, and by implication tissue current flow, is linear function of stimulation amplitude. Specifically, the peak scalp voltage artifact measured between two electrodes on the scalp increases linearly with the peak applied current (0.1 to 1 mA) between two separate scalp stimulating electrodes; moreover in a frequency independent manner across low-frequencies (DC to 10 Hz; Figure 20) as used, for example, in tACS (Terney et al., 2008). Similarly, the spatial profile of scalp voltage artifacts is unchanged across low frequencies. This linearity allows us to normalize spatial maps to per-mA of applied current as well as supports generalizing our results to any stimulation intensity and waveform (e.g. AC, DC) within the linear range.

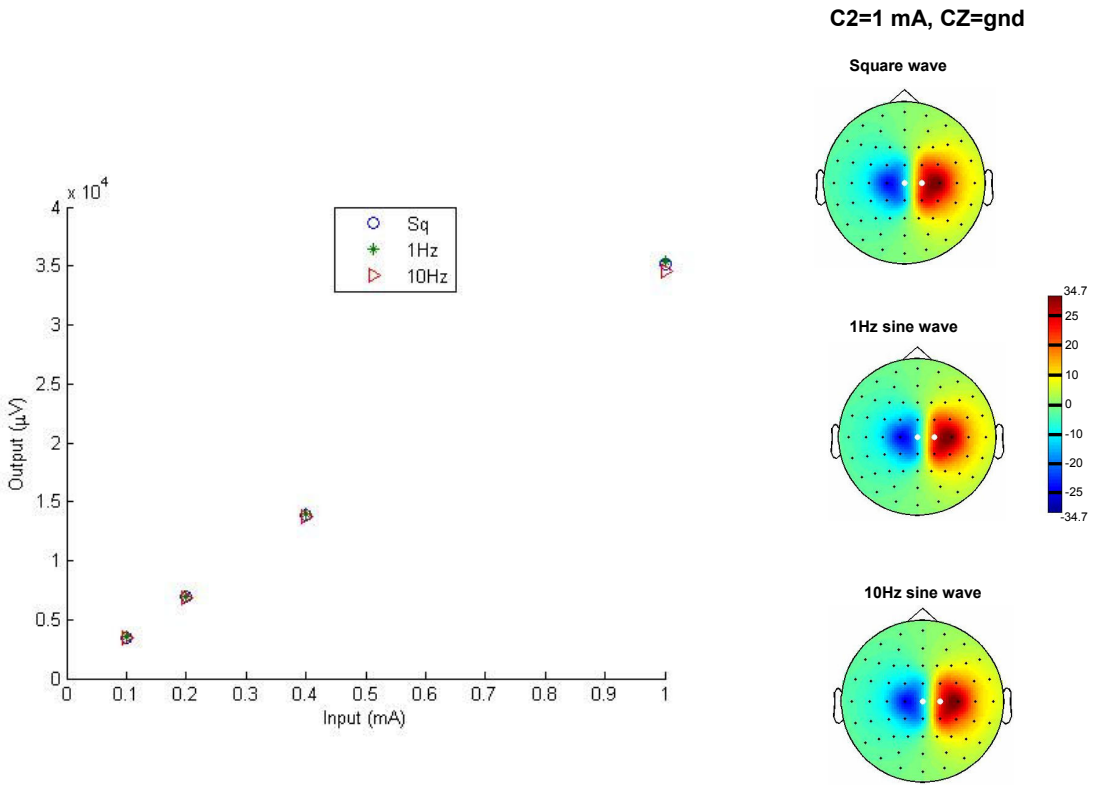


**Figure 20. Linearity of scalp voltages induced as artifacts of transcranial electrical stimulation** The induced scalp potential (artifact) between an arbitrarily selected pair is plotted as a function of stimulation amplitude and frequency using the proximal bipolar montage.

*Spatial maps of scalp voltage artifacts during transcranial electrical stimulation and predicted underlying current distribution*

We measured the scalp voltage artifact induced during transcranial electrical stimulation using three electrode montages. Results from experimental measurement were compared to prediction of a high-resolution FEM model – which was individualized

to the same subject. Each electrode montage resulted in a distinct surface potential that was precisely predicted by the subject-specific FEM model (Figure 20).

For each electrode montage, the FEM model also predicts the resulting current flow in deeper tissue including the skull current density and the cortical electric fields (Figure 20). Several interesting observations and predictions follow. For all montages, including distant bipolar, there is substantial current "shunting" across the scalp such that peak current density decreases but approximately an order of magnitude from scalp to skull. Interestingly, despite current distribution across the entire scalp region between and around electrodes (reflected in a broad scalp voltage distribution) the current density at the skull is highly localized directly under the stimulation electrodes. Taken together, these two observation imply that though significant current is shunted *tangentially* across the scalp, the currents that crosses *radially* through the skull are restricted to under the stimulation electrodes (i.e. essentially current that is shunted across the scalp has little driving force to cross the skull). Despite focal current entry across the skull, however, the resulting electric fields across the brain are still distributed across the cortical entire

**Figure 21. Experimental and FEM model spatial maps of voltage artifact induced on the scalp during transcranial electrical stimulation using three electrode montages**. 1) Proximal bipolar; 2) Distant bipolar; 3) 4x1 concentric ring. The boxed images in the top left for each of the montages show the experimental results. In each case, the electric field distribution on the brain surface and the current density at the skull surface predicted by the model is also shown.

**1) C2=1 mA, CZ=gnd**

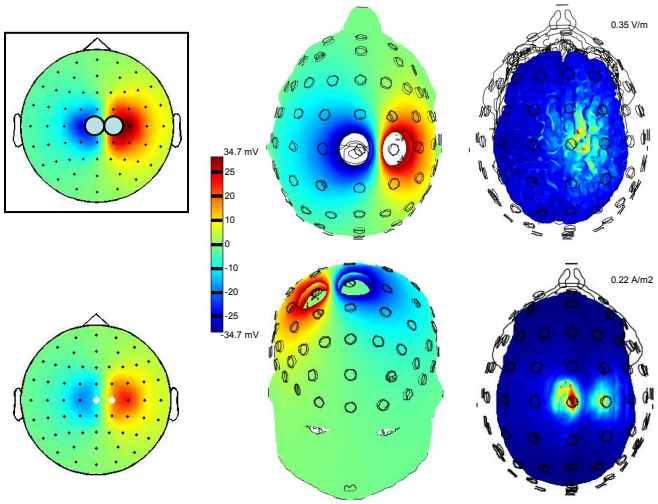


**2) AF4=1 mA, CZ=gnd**

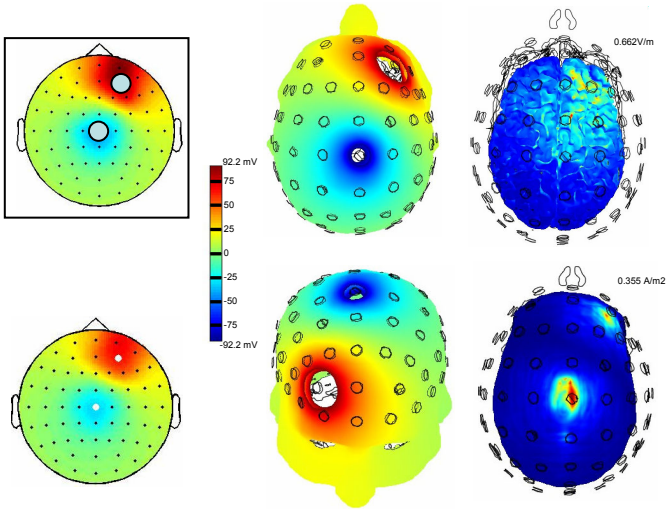


**3) C3 = C4 = Fz = Pz = 0.25 mA; CZ=gnd**

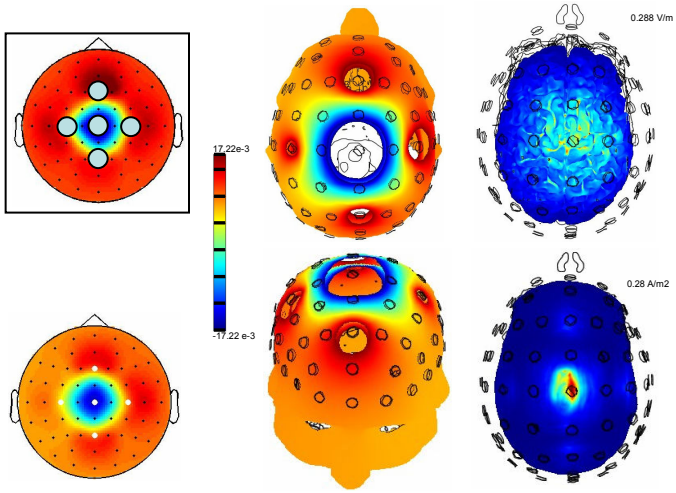

region between electrodes. This is indeed expected (Datta et al., 2009a) as current entering the brain must evidently pass through the *entire* intermediate brain on the way to the return electrode(s) – the more distant the electrodes, the larger the stimulated brain region. This prediction by the FEM model is somewhat in contrast to norms in clinical electrotherapy design where only the regions directly under electrodes are considered "effected" (see Discussion). As addressed below, the presence of a highly conductive layer of CSF further promotes this broad distribution, through is not required for it.

Changing FEM model tissue parameters, such that CSF has the same conductivity as the brain ($\sigma_{CSF}$ = 0.2 S/m), changes predicted scalp voltage artifacts confirming that: 1) Scalp surface artifacts are sensitive to the underlying tissue properties; and 2) The individualized high-resolution FEM model parameterized using standard tissue properties determinately predicts scalp artifacts. Matching CSF conductivity with brain conductivity also changed the predicted cortical electric fields; illustrating how the normally highly conductive CSF acts to further distribute current along the brain surface and promotes "clustering"(Datta et al., 2009a).

## 10.4 Discussion

*Linearity in low intensity and frequency Transcranial Electrical Stimulation*

For relatively low-intensity and frequency, linearity in transcranial electrical stimulation indicates that: 1) As the applied current intensity is increased, the electric

field in all regions scales directly with current amplitude; 2) The induced electric field tracks the waveform of the applied current, independent of frequency. This linearity is indeed an implicit assumption in the clinical design of transcranial electrical stimulation protocols – for example when the effects of distinct dosages are compared. Computational forward-models of weak electrical stimulation generally assume linearity and generalize their results (e.g. across waveforms) based on this linearity.

Non-linearity can arise from the electrode-tissue interface, which is mitigated by the use of current-controlled sources, from changes in skin properties resulting from current flow (Bikson et al., 2009b; Merrill et al., 2005), and complex tissue resistivities. Our results are consistent with linearity for weak-intensity low-frequency transcranial electrical stimulation.

*Scalp and deeper tissue current flow during Transcranial Electrical Stimulation*

Before applied current can effect brain function during transcranial electrical stimulation, current must pass through the scalp and other intermediate tissues. We recently proposed that dogma suggesting the skull is a "low-pass spatial filter" during transcranial current flow, diffusing current and severely limiting stimulation focality, was misguided (Datta et al., 2009a). Rather, the high resistivity of the skull results leads to predominantly radial (specifically *undiffused*) current flow – current diffusion results in other tissues namely the scalp and the CSF. The results of this study provide some experimental support (model validation) and additional insight into this proposed

paradigm. Indeed, the highly focalized current flow through the skull is striking given the broad diffusivity in both the superficial skin and underlying brain (Figure 21).

Current "loss" to due scalp-shunting is well recognized, and estimated previously at approximately 50% of total applied current - highly dependant on the electrode montage (Datta et al., 2008; Miranda et al., 2006; Rush and Driscoll, 1968). Here we show that the resulting peak current density in the brain may be two orders of magnitude below the average current density at the electrode surface (total current/electrode area) – with the scale of reduction highly sensitive to current montage. Peak current density at the electrode/skin is relevant for skin irritation and comfort, while peak current density in the brain determines cognitive outcomes and any undesired neurological effects (Bikson et al., 2009a). Our results thus under-score the importance of accurate computational models in the design of safe and efficacious transcranial electrical stimulation electrode montages.

The degree and extent of current spread has direct implications for the design of electrode montages for effective transcranial current stimulation. Using bipolar montages, our model predicts the passage of current through intermediary cortical regions limits the focality of stimulation; use of smaller electrodes does not prevent this (Figure 21). As expected, the use of more proximal electrodes increases focality at the cost of increase scalp shunting, which needs to be compensated by increased applied current. The 4x1 ring configuration restricts peak current flow to within the "ring" (Figure 21) – thus the controllable size of the ring determines the extent of diffusion.

*Monitoring of scalp voltage "artifacts" during clinical stimulation and relation to electrode-impedance tomography*

Because scalp voltage artifacts reflect the stimulation configuration (electrode montage, current intensity) they provide corroboration that a given clinical dose is being applied correctly. A fault in the device, a sudden problem with an electrode, or misplaced electrodes, will result in a deviation from an expected scalp voltage map (which is not necessarily evident in electrode resistance or stimulator output voltage); we suggest online monitoring of surface (scalp) voltage artifacts (MOSVA) may be incorporated as a safety feature in a stimulation device. MOSVA can be enhanced by, but does not necessarily require, individualized models.

Brain electrode-impedance tomography (EIT) involves application of weak transcranial current and measurement resulting scalp voltage changes for the purpose of imaging brain structures or brain activity (Tidswell et al., 2001). For EIT typically, no *a priori* individualized information is used (e.g. MRI scans) and indeed the rationale for ECT is predicated on accurately determining (resolving) individual anatomical or functional differences. In contrast, MOSVA returns only a binary decision of "correct" or "incorrect" electrode configuration (placements and faults). MOSVA can still leverage the sophistication of analysis tools developed for ECT, especially in the absence of MRI based individualized models.

*Accuracy of FEM models of transcranial electrical stimulation*

FEM forward models of transcranial stimulation are the primary basis for considering how the choice of electrode montage effects resulting current flow through the brain, and hence the targeting of neuromodulation. In this paper we validated the accuracy of a high-resolution individualized FEM model by measuring scalp voltage artifacts. As discussed below, a predictive forward model may indicate changes to how electrode montage is currently considered in clinical practice, as well as methodologies to optimize targeting.

Our measurements of induced scalp voltage artifacts support the accuracy of a high-resolution individualized FEM model of transcranial electrical stimulation, but does not directly validate the model prediction of brain current flow. Especially given that the dose (electrode montage) guidelines suggested by our models challenge certain prevailing clinical assumptions, additional validation is prudent (e.g. imaging). Moreover, clinical outcomes follow from neuromodulatoin which is not a simple function of the brain electric field maps generated by forward models. None-the-less, FEM forward models of transcranial electrical stimulation are based on straightforward parameterization (e.g. tissue anatomy and resistivity) and biophysical assumptions (e.g. ohms law). The results of the present study further support the usefulness of high-resolution forward models in understanding current flow through the brain (which underpins all resulting clinical effects).

Finally, in the absence of verification of brain current flow and association of brain current flow with specific physiological changes, the predictions of forward models must be qualified and questioned. None the less, the diffusivity and clustering of brain modulation observed with our high-resolution models (Datta et al., 2009a), which may be supported by imaging studies (Lang et al., 2005), suggest several interesting questions and revisions into how to rationally design electrode montages for transcranial electrical stimulation.

# Chapter 11: Future Work

The accuracy of any model prediction is limited by accuracy and precision of model anatomy and properties incorporated. Our measurements of induced scalp voltage artifacts support the accuracy of high-resolution individualized FEM modeling for transcranial electrical stimulation. Additionally, the observation of "stimulation clustering" reinforces the importance of models incorporating gyri/sulci resolution. Our results also support the value of individualized models and therapy design/analysis especially in cases related to pathology (skull defects/lesions).

Nonetheless continued technical improvements as well as future work are indicated as follows:

1) *Validating the focality predictions of 4 X1-ring:*

Experimental/functional assessments (such as testing for cortical excitability changes and imaging studies) are needed to confirm the FEM predictions presented in this thesis.

2) *Automation of the modeling process.*

This is critical for economical and broad dissemination with the goal to ultimately individualize tDCS therapy.

*3) Analyze induced current density/EF distributions for various tDCS electrode montages*

tDCS induced cortical electric fields should be calculated and analyzed (correlating with therapy outcome) for all possible clinical montages using high resolution human head models.

*3) Inter-subject Variability:*

tDCS induced cortical electric fields should be calculated and analyzed for different high resolution (1 $mm^3$) subject-specific human head models.

*4) Parameter Sensitivity analysis: Determine the variation of induced current distributions / temperature due to changes in electrical/thermal properties.*

Each of the tissues electrical/thermal values should be varied through a range of values one at a time to determine the variation of current flow and temperature distributions.

5) *Incorporate Diffusion Tensor Imaging (DTI) data:*

The focality predictions of our FEM models should be compared with models incorporating anisotropic properties of white matter and skull.

*6) Characterize tissue temperature increases during tDCS by incorporating micro architecture of the skin*

The bioheat model developed in thesis does not consider *micro architecture* of the skin. There have been studies where the skin has been considered to be composed of an outer unperfused layer ($\omega_b = 0$), sweat glands, hair follicles, and a fat layer. The skin should therefore be modeled by including the highly resistive stratum corneum, epidermis, dermis consisting of *current pores*, and subcutaneous tissue.

# Bibliography

Simpleware Reference Guide-Version 3.2.

Akhtari, M., Bryant, H.C., Mamelak, A.N., Flynn, E.R., Heller, L., Shih, J.J., et al., 2002. Conductivities of three-layer live human skull. Brain Topogr 14, 151-167.

Amassian, V.E., Eberle, L., Maccabee, P.J., Cracco, R.Q., 1992. Modelling magnetic coil excitation of human cerebral cortex with a peripheral nerve immersed in a brain-shaped volume conductor: the significance of fiber bending in excitation. Electroencephalogr Clin Neurophysiol 85, 291-301.

Amassian, V.E., Maccabee, P.J., Cracco, R.Q., Cracco, J.B., Somasundaram, M., Rothwell, J.C., et al., 1994. The polarity of the induced electric field influences magnetic coil inhibition of human visual cortex: implications for the site of excitation. Electroencephalogr Clin Neurophysiol 93, 21-26.

Antal, A., Kincses, T.Z., Nitsche, M.A., Bartfai, O., Paulus, W., 2004a. Excitability changes induced in the human primary visual cortex by transcranial direct current stimulation: direct electrophysiological evidence. Invest Ophthalmol Vis Sci 45, 702-707.

Antal, A., Nitsche, M.A., Kincses, T.Z., Kruse, W., Hoffman, K.P., Paulus, W., 2004b. Facilitation of visuo-motor learning by transcranial direct current stimulation of the motor and the extrastriate visual areas in humans. European Journal of Neuroscience 19, 2888-2892.

Arana, A.B., Borckardt, J.J., Ricci, R., Anderson, B., Li, X., Linder, K.J., et al., 2008. Focal electrical stimulation as a sham control for repetitive transcranial magnetic stimulation: Does it truly mimic the cutaneous sensation and pain of active prefrontal repetitive transcranial magnetic stimulation? Brain Stimul 1, 44-51.

Ardolino, G., Bossi, B., Barbieri, S., Priori, A., 2005. Non-synaptic mechanisms underlie the after-effects of cathodal transcutaneous direct current stimultion of the human brain. Journal of Physiology 568, 653-663.

Barbas, H., 2000. Connections underlying the synthesis of cognition, memory, and emotion in primate prefrontal cortices. Brain Res Bull 52, 319-330.

Baumann, S.B., Wozny, D.R., Kelly, S.K., Meno, F.M., 1997. The electrical conductivity of human cerebrospinal fluid at body temperature. IEEE Trans Biomed Eng 44, 220-223.

Besio, W., Aakula, R., Koka, K., Dai, W., 2006a. Development of a tri-polar concentric ring electrode for acquiring accurate Laplacian body surface potentials. Ann Biomed Eng 34, 426-435.

Besio, W.G., Koka, K., Aakula, R., Dai, W., 2006b. Tri-polar concentric ring electrode development for laplacian electroencephalography. IEEE Trans Biomed Eng 53, 926-933.

Besio, W.G., Koka, K., Cole, A.J., 2007. Effects of noninvasive transcutaneous electrical stimulation via concentric ring electrodes on pilocarpine-induced status epilepticus in rats. Epilepsia 48, 2273-2279.

Bikson, M., Bulow, P., Stiller, J.W., Datta, A., Battaglia, F., Karnup, S.V., et al., 2008. Transcranial direct current stimulation for major depression:a general system for quantifying transcranial electrotherapy dosage Current treatment options in neurology 10, 377-385.

Bikson, M., Datta, A., Elwassif, M., 2009a. Establishing safety limits of transcranial direct current stimulation Clinical Neurophysiology 120, 1033-1034.

Bikson, M., Datta, A., Elwassif, M., Bansal, V., Peterchev, A.V., 2009b. Introduction to electrotherapy technology. J Pain Management 2, 231-238.

Bikson, M., Datta, A., Rahman, A., Scaturro, J., 2010. Electrode montages for tDCS and weak transcranial electrical stimulation: Role of "return" electrode's position and size. Clin Neurophysiol, in press.

Bikson, M., Inoue, M., Akiyama, H., Deans, J.K., Fox, J.E., Miyakawa, H., et al., 2004. Effects of uniform extracellular DC electric fields on excitability in rat hippocampal slices in vitro Journal of Physiology 557, 175-190.

Bikson, M., Lian, J., Hahn, P.J., Stacey, W.C., Sciortino, C., Durand, D.M., 2001. Suppression of epileptiform activity by high frequency sinusoidal fields in rat hippocampal slices. J Physiol 531, 181-191.

Bikson, M., Radman, T., Datta, A., 2006. Rational modulation of neuronal processing with applied electric fields. Conf Proc IEEE Eng Med Biol Soc 1, 1616-1619.

Bindman, L.J., Lippold, O.C., Redfearn, J.W., 1964. The Action of Brief Polarizing Currents on the Cerebral Cortex of the Rat (1) During Current Flow and (2) in the Production of Long-Lasting after-Effects. J Physiol 172, 369-382.

Boggio, P.S., Bermpohl, F., Vergara, A.O., Muniz, A.L., Nahas, F.H., Leme, P.B., et al., 2007. Go-no-go task performance improvement after anodal transcranial DC stimulation of the left dorsolateral prefrontal cortex in major depression Journal of Affective Disorders 101, 91-98.

Boggio, P.S., Ferrucci, R., Rigonatti, S.P., Covre, P., Nitsche, M., Pascual-Leone, A., et al., 2006. Effects of transcranial direct current stimulation on working memory in patients with Parkinson's disease. J Neurol Sci 249, 31-38.

Boggio, P.S., Khoury, L.P., Martins, D.C., Martins, O.E., de Macedo, E.C., Fregni, F., 2009a. Temporal cortex direct current stimulation enhances performance on a visual recognition memory task in Alzheimer disease. J Neurol Neurosurg Psychiatry 80, 444-447.

Boggio, P.S., Liquori, P., Sultani, N., Rezende, L., Fecteau, S., Fregni, F., 2009b. Cumulative priming effects of cortical stimulation on smoking cue-induced craving Neuroscience Letters 463, 82-86.

Boggio, P.S., Zaghi, S., Fregni, F., 2009c. Modulation of emotions associated with images of human pain using anodal transcranial direct current stimulation (tDCS) Neuropsychologia 47, 212-217.

Boggio, P.S., Zaghi, S., Lopes, M., Fregni, F., 2008. Modulatory effects of anodal transcranial direct current stimulation on perception and pain thresholds in healthy volunteers European Journal of Neurology 15, 1124-1130.

Borckardt, J.J., Linder, K.J., Ricci, R., Li, X., Anderson, B., Arana, A., et al., 2009a. Focal electrically administered therapy: device parameter effects on stimulus perception in humans. J Ect 25, 91-98.

Borckardt, J.J., Smith, A.R., Reeves, S.T., Madan, A., Shelley, N., Branham, R., et al., 2009b. A pilot study investigating the effects of fast left prefrontal rTMS on chronic neuropathic pain. Pain Med 10, 840-849.

Borckardt, J.J., Smith, A.R., Reeves, S.T., Weinstein, M., Kozel, F.A., Nahas, Z., et al., 2007. Fifteen minutes of left prefrontal repetitive transcranial magnetic stimulation acutely increases thermal pain thresholds in healthy adults. Pain Res Manag 12, 287-290.

Butson, C.R., Cooper, S.E., Henderson, J.M., McIntyre, C.C., 2007. Patient-specific analysis of the volume of tissue activated during deep brain stimulation. Neuroimage 34, 661-670.

Calancie, B., Harris, W., Broton, J.G., Alexeeva, N., Green, B.A., 1998. Threshold-level multipulse transcranial electrical stimulation of motor cortex for intraoperative monitoring of spinal motor tracts: description of method and comparison to somatosensory evoked potential monitoring Journal of Neurosurgery 88, 457-470.

Cardinal, R.N., Parkinson, J.A., Hall, J., Everitt, B.J., 2002. Emotion and motivation: the role of the amygdala, ventral striatum, and prefrontal cortex. Neurosci Biobehav Rev 26, 321-352.

Carney, M.W., 1969. Negative polarisation of the brain in the treatment of manic states. Ir J Med Sci 8, 133-135.

Chan, C.Y., Hounsgaard, J., Nicholson, C., 1988. Effects of electric fields on transmembrane potential and excitability of turtle cerebellar Purkinje cells in vitro. J Physiol 402, 751-771.

Chan, C.Y., Nicholson, C., 1986. Modulation by applied electric fields of Purkinje and stellate cell activity in the isolated turtle cerebellum. J Physiol 371, 89-114.

Cohen, L.G., Hallett, M., 1988. Methodology for non-invasive mapping of human motor cortex with electrical stimulation. Electroencephalogr Clin Neurophysiol 69, 403-411.

Cohen, L.G., Roth, B.J., Nilsson, J., Dang, N., Panizza, M., Bandinelli, S., et al., 1990. Effects of coil design on delivery of focal magnetic stimulation. Technical considerations. Electroencephalogr Clin Neurophysiol 75, 350-357.

Costain, R., Redfearn, J.W., Lippold, O.C., 1964. A Controlled Trial of the Therapeutic Effect of Polarization of the Brain in Depressive Illness. Br J Psychiatry 110, 786-799.

Datta, A., Bansal, V., Diaz, J., Patel, J., Reato, D., Bikson, M., 2009a. Gyri-precise head model of transcranial direct current stimulation: Improved spatial focality using a ring electrode versus conventional rectangular pad Brain Stimulation 2, 201-207.

Datta, A., Elwassif, M., Battaglia, F., Bikson, M., 2008. Transcranial current stimulation focality using disc and ring electrode configurations:FEM analysis. Journal of neural engineering 5, 163-174.

Datta, A., Elwassif, M., Bikson, M., 2009b. Bio-heat transfer model of transcranial DC stimulation: comparison of conventional pad versus ring electrode. Conf Proc IEEE Eng Med Biol Soc 2009, 670-673.

Davidson, R.J., 2002. Anxiety and affective style: role of prefrontal cortex and amygdala. Biol Psychiatry 51, 68-80.

de Leeuw, R., Albuquerque, R., Okeson, J., Carlson, C., 2005. The contribution of neuroimaging techniques to the understanding of supraspinal pain circuits: implications for orofacial pain. Oral Surg Oral Med Oral Pathol Oral Radiol Endod 100, 308-314.

De Lucia, M., Parker, G.J., Embleton, K., Newton, J.M., Walsh, V., 2007. Diffusion tensor MRI-based estimation of the influence of brain tissue anisotropy on the effects of transcranial magnetic stimulation. Neuroimage 36, 1159-1170.

De Mercato, G., Garcia Sanchez, F.J., 1992. Correlation between low-frequency electric conductivity and permittivity in the diaphysis of bovine femoral bone. IEEE Trans Biomed Eng 39, 523-526.

Deans, J.K., Powell, A.D., Jefferys, J.G., 2007. Sensitivity of coherent oscillations in rat hippocampus to AC electric fields. J Physiol 583, 555-565.

Deng, Z.D., Peterchev, A.V., Lisanby, S.H., 2008. Coil design considerations for deep-brain transcranial magnetic stimulation (dTMS). Conf Proc IEEE Eng Med Biol Soc 2008, 5675-5679.

Dundas, J.E., Thickbroom, G.W., Mastaglia, F.L., 2007. Perception of comfort during transcranial DC stimulation: effect of NaCl solution concentration applied to sponge electrodes. Clin Neurophysiol 118, 1166-1170.

Durand, D.M., 2007. Neural engineering--a new discipline for analyzing and interacting with the nervous system. Methods Inf Med 46, 142-146.

Durand, D.M., Bikson, M., 2001. Suppression and control of epileptiform activity by electrical stimulation: a review. Proc IEEE 89, 1065-1082.

Elwassif, M.M., Kong, Q., Vasquez, M., Bikson, M., 2006. Bio-heat transfer model of deep brain stimulation-induced temperature changes. Journal of neural engineering 3, 306-315.

Farina, D., Cescon, C., 2001. Concentric-ring electrode systems for noninvasive detection of single motor unit activity. IEEE Trans Biomed Eng 48, 1326-1334.

Ferdjallah, M., Bostick, F.X., Jr., Barr, R.E., 1996. Potential and current density distributions of cranial electrotherapy stimulation (CES) in a four-concentric-spheres model. IEEE Trans Biomed Eng 43, 939-943.

Francis, J.T., Gluckman, B.J., Schiff, S.J., 2003. Sensitivity of neurons to weak electric fields. Journal of Neuroscience 23, 7255-7261.

Fregni, F., Boggio, P.S., Lima, M.C., Ferreira, M.J., Wagner, T., Rigonatti, S.P., et al., 2006a. A sham-controlled, phase II trial of transcranial direct current stimulation for the treatment of central pain in traumatic spinal cord injury. Pain 122, 197-209.

Fregni, F., Boggio, P.S., Lima, M.C., Ferreira, M.J., Wagner, T., Rigonatti, S.P., et al., 2006b. A sham-controlled,phase II trial of transcranial direct current stimulation for the treatment of central pain in traumatic spinal cord injury. Pain 122, 197-209.

Fregni, F., Boggio, P.S., Nitsche, M.A., Bermpohl, F., Antal, A., Feredoes, E., et al., 2005a. Anodal transcranial direct current stimulation of prefrontal cortex enhances working memory. Experimental Brain Research 166, 23-30.

Fregni, F., Freedman, S.D., Pascual-Leone, A., 2007. Recent advances in the treatment of chronic pain with non-invasive brain stimulation techniques Lancet Neurology 6, 188-191.

Fregni, F., Gimenes, R., Valle, A.C., Ferreira, M.J., Rocha, R.R., Natalle, L., et al., 2006c. A randomized, sham-controlled, proof of principle study of transcranial direct

current stimulation for the treatment of pain in fibromyalgia. Arthritis Rheum 54, 3988-3998.

Fregni, F., Simon, D.K., Wu, A., Pascual-Leone, A., 2005b. Non-invasive brain stimulation for Parkinson's disease: a systematic review and meta-analysis of the literature Journal of Neurology,Neurosurgery,and Psychiatry 76, 1614-1623.

Fregni, F., Thome-Souza, S., Nitsche, M.A., Freedman, S.D., Valente, K.D., Pascual-Leone, A., 2006d. A controlled clinical trial of cathodal DC polarization in patients with refractory epilepsy. Epliepsia 47, 335-342.

Fujii, S., Sasaki, H., Ito, K., Kaneko, K., Kato, H., 2002. Temperature dependence of synaptic responses in guinea pig hippocampal CA1 neurons in vitro. Cell Mol Neurobiol 22, 379-391.

Gabriel, C., Gabriel, S., Corthout, E., 1996. The dielectric properties of biological tissues: I. Literature survey. Phys Med Biol 41, 2231-2249.

Gartside, I.B., 1968. Mechanisms of sustained increases of firing rate of neurones in the rat cerebral cortex after polarization: role of protein synthesis. Nature 220, 383-384.

Geddes, L.A., Baker, L.E., 1967. The specific resistance of biological material--a compendium of data for the biomedical engineer and physiologist. Med Biol Eng 5, 271-293.

George, M.S., Lisanby, S.H., Sackeim, H.A., 1999. Transcranial magnetic stimulation: applications in neuropsychiatry. Arch Gen Psychiatry 56, 300-311.

Ghai, R.S., Bikson, M., Durand, D.M., 2000. Effects of applied electric fields on low-calcium epileptiform activity in the CA1 region of rat hippocampal slices. J Neurophysiol 84, 274-280.

Gluckman, B.J., Neel, E.J., Netoff, T.I., Ditto, W.L., Spano, M.L., Schiff, S.J., 1996. Electric field suppression of epileptiform activity in hippocampal slices. J Neurophysiol 76, 4202-4205.

Hattori, Y., Moriwaki, A., Hori, Y., 1990. Biphasic effects of polarizing current on adenosine-sensitive generation of cyclic AMP in rat cerebral cortex. Neurosci Lett 116, 320-324.

Hauesien, J., Ramon, C., Eiselt, M., Brauer, H., Nowak, H., 1997. Influence of tissue resistivities on neuromagnetic fields and electric potentials studied with a finite element model of the head IEEE Trans Biomed Eng 44, 727-735.

Hause, L., 1975. A mathematical model for transmembrane potentials secondary to extracellular fields. New York:Academic.

Hoffmann, H.M., Dionne, V.E., 1983. Temperature dependence of ion permeation at the endplate channel. J Gen Physiol 81, 687-703.

Holdefer, R.N., Sadleir, R., Russell, M.J., 2006. Predicted current densities in the brain during transcranial electrical stimulation. Clinical Neurophysiology 117, 1388-1397.

Holsheimer, J., 1998. Computer modelling of spinal cord stimulation and its contribution to therapeutic efficacy. Spinal Cord 36, 531-540.

Homan, R.W., Herman, J., Purdy, P., 1987. Cerebral location of international 10-20 system electrode placement. Electroencephalogr Clin Neurophysiol 66, 376-382.

Hummel, F., Celnik, P., Giraux, P., Floel, A., Wu, W.H., Gerloff, C., et al., 2005. Effects of non-invasive cortical stimulation on skilled motor function in chronic stroke Brain 128, 490-499.

Im, C.H., Jung, H.H., Choi, J.D., Lee, S.Y., Jung, K.Y., 2008. Determination of optimal electrode positions for transcranial direct current stimulation (tDCS). Phys Med Biol 53, N219-225.

Islam, N., Aftabuddin, M., Moriwaki, A., Hattori, Y., Hori, Y., 1995. Increase in the calcium level following anodal polarization in the rat brain. Brain Res 684, 206-208.

Iyer, M.B., Mattu, U., Grafman, J., Lomarev, M., Sato, S., Wassermann, E.M., 2005. Safety and cognitive effect of frontal DC brain polarization in healthy individuals Neurology 64, 872-875.

Janssen, F.E.M., Van Leeuwen, G.M.J., Van Steenhoven, A.A., 2005. Modeling of temperature and perfusion during scalp cooling. Physics in Medicine and Biology 50, 4065-4073.

Jefferys, J.G., 1981. Influence of electric fields on the excitability of granule cells in guinea-pig hippocampal slices. J Physiol 319, 143-152.

Jefferys, J.G., Deans, J., Bikson, M., Fox, J., 2003. Effects of weak electric fields on the activity of neurons and neuronal networks. Radiat Prot Dosimetry 106, 321-323.

Johnson, M.D., McIntyre, C.C., 2008. Quantifying the neural elements activated and inhibited by globus pallidus deep brain stimulation. J Neurophysiol 100, 2549-2563.

Kanai, R., Chaieb, L., Antal, A., Walsh, V., Paulus, W., 2008. Frequency-dependent electrical stimulation of the visual cortex. Curr Biol 18, 1839-1843.

Kincses, T.Z., Antal, A., Nitsche, M.A., Bartfai, O., Paulus, W., 2004. Facilitation of probabilistic classification learning by transcranial direct current stimulation of the prefrontal cortex in the human. Neuropsychologia 42, 113-117.

Komssi, S., Savolainen, P., Heiskala, J., Kahkonen, S., 2007. Excitation threshold of the motor cortex estimated with transcranial magnetic stimulation electroencephalography. Neuroreport 18, 13-16.

Kowalski, T., Silny, J., Buchner, H., 2002. Current density threshold for the stimulation of neurons in the motor cortex area. Bioelectromagnetics 23, 421-428.

Krings, T., Buchbinder, B.R., Butler, W.E., Chiappa, K.H., Jiang, H.J., Cosgrove, G.R., et al., 1997. Functional magnetic resonance imaging and transcranial magnetic stimulation: complementary approaches in the evaluation of cortical motor function. Neurology 48, 1406-1416.

Kwon, Y.H., Ko, M.H., Ahn, S.H., Kim, Y.H., Song, J.C., Lee, C.H., et al., 2008. Primary motor cortex activation by transcranial direct current stimulation in the human brain. Neurosci Lett 435, 56-59.

Lagopoulos, J., Degabriele, R., 2008. Feeling the heat: the electrode-skin interface during DCS. Acta Neuropsychiatra 20, 98-100.

Lang, N., Nitsche, M.A., Paulus, W., Rothwell, J.C., Lemon, R.N., 2004. Effects of transcranial direct current stimulation over the human motor cortex on corticospinal and transcallosal excitability. Exp Brain Res 156, 439-443.

Lang, N., Siebner, H.R., Wards, N.S., Lee, L., Nitsche, M.A., Paulus, W., et al., 2005. How does transcranial DC stimulation of the primary motor cortex alter regional neuronal activity in the human brain? European Journal of Neuroscience 22, 495-504.

Lefaucheur, J.P., 2006. New insights into the therapeutic potential of non-invasive transcranial cortical stimulation in chronic neuropathic pain. Pain 122, 11-13.

Liebetanz, D., Klinker, F., Hering, D., Koch, R., Nitsche, M.A., Potschka, H., et al., 2006. Anticonvulsant effects of transcranial direct-current stimulation (tDCS) in the rat cortical ramp model of focal epilepsy. Epliepsia 47, 1216-1224.

Liebetanz, D., Koch, R., Mayenfels, S., Konig, F., Paulus, W., Nitsche, M.A., 2009. Safety limits of cathodal transcranial direct current stimulation in rats. Clinical Neurophysiology 120, 1161-1167.

Liebetanz, D., Nitsche, M.A., Tergau, F., Paulus, W., 2002. Pharmacological approach to the mechanisms of transcranial DC-stimulation-induced after-effects of human motor cortex excitability. Brain 125, 2238-2247.

Lima, M.C., Fregni, F., 2008. Motor cortex stimulation for chronic pain: systematic review and meta-analysis of the literature. Neurology 70, 2329-2337.

Lisanby, S.H., 2007. Electroconvulsive therapy for depression. N Engl J Med 357, 1939-1945.

Maccabee, P.J., Amassian, V.E., Eberle, L.P., Cracco, R.Q., 1993. Magnetic coil stimulation of straight and bent amphibian and mammalian peripheral nerve in vitro: locus of excitation. J Physiol 460, 201-219.

MacDonald, D.B., 2002. Safety of intraoperative transcranial electrical stimulation motor evoked potential monitoring. Journal Clinical Neurophysiology 19, 416-429.

Marshall, L., Helgadottir, H., Molle, M., Born, J., 2006. Boosting slow oscillations during sleep potentiates memory. Nature 444, 610-613.

Marshall, L., Molle, M., Hallschmid, M., Born, J., 2004. Transcranial direct current stimulation during sleep improves declarative memory. J Neurosci 24, 9985-9992.

Marshall, L., Molle, M., Siebner, H.R., Born, J., 2005. Bifrontal transcranial direct current stimulation slows reaction time in a working memory task BMC Neuroscience 6, 23.

McIntyre, C.C., Grill, W.M., 1999. Excitation of central nervous system neurons by nonuniform electric fields. Biophys J 76, 878-888.

McIntyre, C.C., Mori, S., Sherman, D.L., Thakor, N.V., Vitek, J.L., 2004. Electric field and stimulating influence generated by deep brain stimulation of the subthalamic nucleus. Clin Neurophysiol 115, 589-595.

Merrill, D.R., Bikson, M., Jefferys, J.G., 2005. Electrical stimulation of excitable tissue:design of efficacious and safe protocols. J Neurosci Methods 141, 171-198.

Millan, M.J., 2002. Descending control of pain. Prog Neurobiol 66, 355-474.

Minhas, P., Bansal, V., Patel, J., Ho, J.S., Diaz, J., Datta, A., et al., 2010. Electrodes for high-definition transcutaneous DC stimulation for applications in drug delivery and electrotherapy, including tDCS. J Neurosci Methods 190, 188-197.

Miranda, P.C., Faria, P., Hallett, M., 2009. What does the ratio of injected current to electrode area tell us about current density in the brain during tDCS? . Clinical Neurophysiology 120, 1183-1187.

Miranda, P.C., Hallett, M., Basser, P.J., 2003. The electric field induced in the brain by magnetic stimulation: a 3-D finite-element analysis of the effect of tissue heterogeneity and anisotropy. IEEE Trans Biomed Eng 50, 1074-1085.

Miranda, P.C., Lomarev, M., Hallett, M., 2006. Modeling the current distribution during transcranial direct current stimulation. Clin Neurophysiol 117, 1623-1629.

Moliadze, V., Antal, A., Paulus, W., 2010. Electrode-distance dependent after-effects of transcranial direct and random noise stimulation with extracephalic reference electrodes. Clin Neurophysiol Epub.

Morgan, M.A., Romanski, L.M., LeDoux, J.E., 1993. Extinction of emotional learning: contribution of medial prefrontal cortex. Neurosci Lett 163, 109-113.

Murphy, D.G., DeCarli, C., Schapiro, M.B., Rapoport, S.I., Horwitz, B., 1992. Age-related differences in volumes of subcortical nuclei, brain matter, and cerebrospinal fluid in healthy men as measured with magnetic resonance imaging. Arch Neurol 49, 839-845.

Nadeem, M., Thorlin, T., Gandhi, O.P., Persson, M., 2003. Computation of electric and magnetic stimulation in human head using the 3-D impedance method. IEEE Transactions on Biomedical Engineering 50, 900-907.

Nagarajan, S.S., Durand, D.M., Warman, E.N., 1993. Effects of induced electric fields on finite neuronal structures: a simulation study. IEEE Trans Biomed Eng 40, 1175-1188.

Nahmias, F., Debes, C., de Andrade, D.C., Mhalla, A., Bouhassira, D., 2009. Diffuse analgesic effects of unilateral repetitive transcranial magnetic stimulation (rTMS) in healthy volunteers. Pain 147, 224-232.

Nathan, S.S., Sinha, S.R., Gordon, B., Lesser, R.P., Thakor, N.V., 1993. Determination of current density distributions generated by electrical stimulation of the human cerebral cortex. Electroencephalogr Clin Neurophysiol 86, 183-192.

Nelson, D.A., Nelson, M.T., Walters, T.J., Mason, P.A., 2000. Skin heating effects of millimeter wave irradiation-Thermal modeling results. IEEE Transactions Microwave Theory Tech 48, 2111-2120.

Nelson, D.A., Nunneley, S.A., 1998. Brain temperature and limits on transcranial cooling in humans:quantitative modeling results European Journal of Applied Physiology 78, 353-359.

Nitsche, M.A., Cohen, L.G., Wassermann, E.M., Priori, A., Lang, N., Antal, A., et al., 2008. Transcranial direct current stimulation: State of the art 2008. Brain Stimul 1, 206-223.

Nitsche, M.A., Doemkes, S., Karakose, T., Antal, A., Liebetanz, D., Lang, N., et al., 2007. Shaping the effects of transcranial direct current stimulation of the human motor cortex Journal of Neurophsyiology 97, 3109-3117.

Nitsche, M.A., Fricke, K., Henschke, U., Schlitterlau, A., Liebetanz, D., Lang, N., et al., 2003a. Pharmacological modulation of cortical excitability shifts induced by transcranial direct current stimulation in humans. J Physiol 553, 293-301.

Nitsche, M.A., Liebetanz, D., Lang, N., Antal, A., Tergau, F., Paulus, W., 2003b. Safety criteria for transcranial direct current stimulation (tDCS) in humans. Clin Neurophysiol 114, 2220-2222; author reply 2222-2223.

Nitsche, M.A., Nitsche, M.S., Klein, C.C., Tergau, F., Rothwell, J.C., Paulus, W., 2003c. Level of action of cathodal DC polarisation induced inhibition of the human motor cortex. Clinical Neurophysiology 114, 600-604.

Nitsche, M.A., Paulus, W., 2000. Excitability changes induced in the human motor cortex by weak transcranial direct current stimulation. Journal of Physiology 527, 633-639.

Nitsche, M.A., Paulus, W., 2001. Sustained excitability elevations induced by transcranial DC motor cortex stimulation in humans Neurology 57, 1899-1901.

Nitsche, M.A., Schauenburg, A., Lang, N., Liebetanz, D., Exner, C., Paulus, W., et al., 2003d. Facilitation of implicit motor learning by weak transcranial direct current stimulation of the primary motor cortex in the human Journal of Cognitive Neuroscience 15, 619-626.

Nitsche, M.A., Seeber, A., Frommann, K., Klein, C.C., Rochford, C., Nitsche, M.S., et al., 2005. Modulating parameters of excitability during and after transcranial direct current stimulation of the human motor cortex. J Physiol 568, 291-303.

Oda, H., Fujitani, Y., 1990. Concentric electrodes for producing acupuncture-like anesthetic effects. Tohoku J Exp Med 160, 169-175.

Oostendorp, T.F., Hengeveld, Y.A., Wolters, C.H., Stinstra, J., van Elswijk, G., Stegeman, D.F., 2008. Modeling transcranial DC stimulation. Conf Proc IEEE Eng Med Biol Soc 2008, 4226-4229.

Palm, U., Keeser, D., Schiller, C., Fintescu, Z., Reisinger, E., Padberg, F., 2008. Skin lesions after treatment with transcranial direct current stimulation (tDCS) Brain Stimulation 1, 386-387.

Passard, A., Attal, N., Benadhira, R., Brasseur, L., Saba, G., Sichere, P., et al., 2007. Effects of unilateral repetitive transcranial magnetic stimulation of the motor cortex on chronic widespread pain in fibromyalgia. Brain 130, 2661-2670.

Plonsey, R., Altman, K.W., 1988. Electrical stimulation of excitable cells-a model approach. Proc IEEE 76, 1122-1129.

Plonsey, R., Barr, R.C., 1995. Electric field stimulation of excitable tissue. IEEE Trans Biomed Eng 42, 329-336.

Poreisz, C., Boros, K., Antal, A., Paulus, W., 2007. Safety aspects of transcranial direct current stimulation concerning healthy subjects and patients. Brain Res Bull 72, 208-214.

Prausnitz, M.R., 1996. The effects of electric current applied to skin: a review for transdermal drug delivery Adv Drug Deliv Rev 18, 395-425.

Priori, A., 2003a. Brain polarization in humans: a reappraisal of an old tool for prolonged non-invasive modulation of brain excitability. Clin Neurophysiol 114, 589-595.

Priori, A., 2003b. Reply to Dr. Paulus. Clin Neurophysiol 114, 2223.

Purpura, D.P., McMurtry, J.G., 1965. Intracellular Activities and Evoked Potential Changes During Polarization of Motor Cortex. J Neurophysiol 28, 166-185.

Radman, T., Su, Y., An, J.H., Parra, L.C., Bikson, M., 2007. Spike timing amplifies the effect of electric fields on neurons: implications for endogenous field effects. J Neurosci 27, 3030-3036.

Ranck, J.B., Jr., 1963. Specific impedance of rabbit cerebral cortex. Exp Neurol 7, 144-152.

Ranck, J.B., Jr., 1975. Which elements are excited in electrical stimulation of mammalian central nervous system: a review Brain Res 98, 417-440.

Rattay, F., 1986. Analysis of models for external stimulation of axons. IEEE Trans Biomed Eng 33, 974-977.

Rattay, F., 1989. Analysis of models for extracellular fiber stimulation. IEEE Trans Biomed Eng 36, 676-682.

Rattay, F., 1998. Analysis of the electrical excitation of CNS neurons. IEEE Trans Biomed Eng 45, 766-772.

Rempel-Clower, N.L., Barbas, H., 1998. Topographic organization of connections between the hypothalamus and prefrontal cortex in the rhesus monkey. Journal of comparative neurology 31, 393-419.

Ren, C., Tarjan, P.P., Popovic, D.B., 1995. A novel electric design for electromagnetic stimulation--the Slinky coil. IEEE Trans Biomed Eng 42, 918-925.

Rish, L., Dillon, J.D., Meirowsky, A.M., Caveness, W.F., Mohr, J.P., Kistler, J.P., et al., 1979. Cranioplasty: a review of 1030 cases of penetrating head injury. Neurosurgery 4, 381-385.

Roizenblatt, S., Fregni, F., Gimenez, R., Wetzel, T., Rigonatti, S.P., Tufik, S., et al., 2007. Site-specific effects of transcranial direct current stimulation on sleep and pain in fibromyalgia: a randomized, sham-controlled study. Pain Pract 7, 297-306.

Rossini, P.M., Marciani, M.G., Caramia, M., Roma, V., Zarola, F., 1985. Nervous propagation along 'central' motor pathways in intact man: characteristics of motor responses to 'bifocal' and 'unifocal' spine and scalp non-invasive stimulation. Electroencephalogr Clin Neurophysiol 61, 272-286.

Rotenberg, A., Harrington, M.G., Birnbaum, D.S., Madsen, J.R., Glass, I.E., Jensen, F.E., et al., 2007. Minimal heating of titanium skull plates during 1Hz reptitive transcranial magnetic stimulation Clinical Neurophysiology 118, 2536-2538.

Rotenberg, A., Pascual-Leone, A., 2009. Safety of 1 Hz repititive transcranial magnetic stimulation (rTMS) in patients with titanium skull plates Clinical Neurophysiology 120, 1417.

Roth, B.J., 1994. Mechanisms for electrical stimulation of excitable tissue. Crit Rev Biomed Eng 22, 253-305.

Roth, Y., Zangen, A., Hallett, M., 2002. A coil design for transcranial magnetic stimulation of deep brain regions. J Clin Neurophysiol 19, 361-370.

Ruohonen, J., Ilmoniemi, R.J., 1998. Focusing and targeting of magnetic brain stimulation using multiple coils. Med Biol Eng Comput 36, 297-301.

Rush, S., Driscoll, D.A., 1968. Current distribution in the brain from surface electrodes. Anesth Analg 47, 717-723.

Rushton, W.A., 1927. The effect upon the threshold for nervous excitation of the length of nerve exposed, and the angle between current and nerve. J Physiol 63, 357-377.

Sadleir, R.J., Vannorsdall, T.D., Schretlen, D.J., Gordon, B., 2010. Transcranial direct current stimulation (tDCS) in a realistic head model. Neuroimage 51, 1310-1318.

Sampson, S.M., Rome, J.D., Rummans, T.A., 2006. Slow-frequency rTMS reduces fibromyalgia pain. Pain Med 7, 115-118.

Saypol, J.M., Roth, B.J., Cohen, L.G., Hallett, M., 1991. A theoretical comparison of electric and magnetic stimulation of the brain. Ann Biomed Eng 19, 317-328.

Schroeder, M.J., Barr, R.E., 2001. Quantative analysis of the electroencephalogram during cranial electrotherapy stimulation. Clinical Neurophysiology 112, 2075-2083.

Sekhar, L., Fessler, R., 2006. Atlas of Neurosurgical Techniques:Brain Thieme, New York.

Simpson, J.R., Jr., Drevets, W.C., Snyder, A.Z., Gusnard, D.A., Raichle, M.E., 2001. Emotion-induced changes in human medial prefrontal cortex: II. During anticipatory anxiety. Proc Natl Acad Sci U S A 98, 688-693.

Smith, S.M., 2002. Fast robust automated brain extraction. Hum Brain Mapp 17, 143-155.

Stecker, M.M., 2005. Transcranial electric stimulation of motor pathways: a theoretical analysis. Comput Biol Med 35, 133-155.

Suihko, V., 1998. Modeling direct activation of corticospinal axons using transcranial electrical stimulation. Electroencephalogr Clin Neurophysiol 109, 238-244.

Suihko, V., 2002. Modelling the response of scalp sensory receptors to transcranial electrical stimulation. Med Biol Eng Comput 40, 395-401.

Szmurlo, R., Sawicki, B., Starzynski, J., Wincenciak, S., 2006. A comparison of two models of electrodes for ECT simulations IEEE Trans Magnet 42, 1395-1398.

Terney, D., Chaieb, L., Moliadze, V., Antal, A., Paulus, W., 2008. Increasing human brain excitability by transcranial high-frequency random noise stimulation. J Neurosci 28, 14147-14155.

Tidswell, T., Gibson, A., Bayford, R.H., Holder, D.S., 2001. Three-dimensional electrical impedance tomography of human brain activity. Neuroimage 13, 283-294.

Tranchina, D., Nicholson, C., 1986. A model for the polarization of neurons by extrinsically applied electric fields. Biophys J 50, 1139-1156.

Uy, J., Ridding, M.C., 2003. Increased cortical excitability induced by transcranial DC and peripheral nerve stimulation. Journal of Neuroscience Methods 127, 193-197.

van Oosterom, A., Strackee, J., 1983. Computing the lead field of electrodes with axial symmetry. Med Biol Eng Comput 21, 473-481.

Wagner, T., Fregni, F., Fecteau, S., Grodzinsky, A., Zahn, M., Pascual-Leone, A., 2007. Transcranial direct current stimulation:a computer-based human model study Neuroimage 35, 1113-1124.

Wagner, T.A., Zahn, M., Grodzinsky, A.J., Pascual-Leone, A., 2004. Three-dimensional head model simulation of transcranial magnetic stimulation. IEEE Trans Biomed Eng 51, 1586-1598.

Wassermann, E.M., Wang, B., Zeffiro, T.A., Sadato, N., Pascual-Leone, A., Toro, C., et al., 1996. Locating the motor cortex on the MRI with transcranial magnetic stimulation and PET. Neuroimage 3, 1-9.

Webster, B.R., Celnik, P.A., Cohen, L.G., 2006. Noninvasive brain stimulation in stroke rehabilitation. NeuroRx 3, 474-481.

Wolfe, F., Smythe, H.A., Yunus, M.B., Bennett, R.M., Bombardier, C., Goldenberg, D.L., et al., 1990. The American College of Rheumatology 1990 Criteria for the Classification of Fibromyalgia. Report of the Multicenter Criteria Committee. Arthritis Rheum 33, 160-172.

Wongsarnpigoon, A., Grill, W.M., 2008. Computational modeling of epidural cortical stimulation. J Neural Eng 5, 443-454.

Zentner, J., 1989. Noninvasive motor evoked potential monitoring during neurosurgical operations on the spinal cord Neurosurgery 24, 709-712.

Zhang, Y., Brady, M., Smith, S., 2001. Segmentation of brain MR images through a hidden Markov random field model and the expectation-maximization algorithm. IEEE Trans Medical Imaging 20, 45-57.